

Aspects of *in situ* angular scattering measurements in contrasting waters

Håkon Johan Sandven

Thesis for the degree of Philosophiae Doctor (PhD)
University of Bergen, Norway
2022

UNIVERSITY OF BERGEN



Aspects of *in situ* angular scattering measurements in contrasting waters

Håkon Johan Sandven



Thesis for the degree of Philosophiae Doctor (PhD)
at the University of Bergen

Date of defense: 28.01.2022

© Copyright Håkon Johan Sandven

The material in this publication is covered by the provisions of the Copyright Act.

Year: 2022

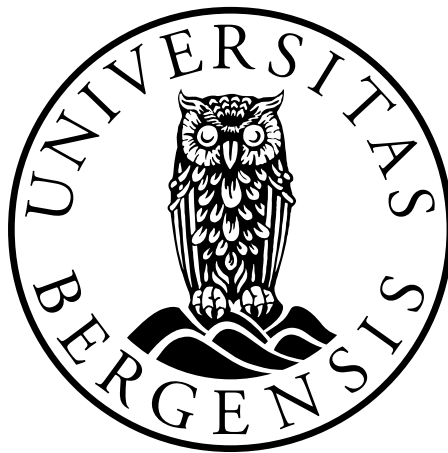
Title: Aspects of *in situ* angular scattering measurements in contrasting waters

Name: Håkon Johan Sandven

Print: Skipnes Kommunikasjon / University of Bergen

Aspects of *in situ* angular scattering measurements in contrasting waters

Håkon Sandven

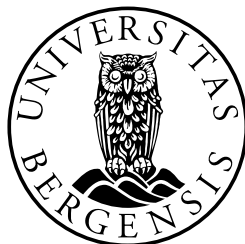


Dissertation for the degree of Philosophiae Doctor (PhD)
at the University of Bergen

2021

Scientific environment

This study has been carried out at the Department of Physics and Technology, University of Bergen.



Acknowledgements

Science is fortunately a more collaborative and social pursuit today than in the age of Newton or Faraday, even during years plagued by pandemics and digital meetings. While I have written most of the sentences in this dissertation, more people have contributed to the content of these sentences than possible to mention on a single page. Many thanks to my supervisors Børge and Arne for a close collaboration and great support. Together with my co-authors Yi-Chun, Håvard, Camilla, Svein Rune, Tristan and other members of the "optics corridor", they have formed a very positive and cooperative work environment, which has made it a pleasure to go to work.

Fieldwork has been a central part of my doctoral work, both for the results and the experiences. Many thanks to the Norwegian Coast Guard, especially the crew of KV Svalbard, and other research colleagues on the cruises for support and assistance, and some fun moments even on the longest days. A special mention goes to Henrik, Bjørnar, Espen and Hanne.

I am also thankful for the support from my family and friends throughout the doctoral work, above all during the strange periods of home office and social distancing, and care and patience from Emilia on the final stretch.

Håkon Sandven
Bergen, October 14th 2021

Abstract

Rapid changes are observed in oceanic and coastal environments around the world due to global temperatures increases, ocean acidification and changing weather patterns - anthropogenic climate change. These changes have large effects on the ecosystems of the ocean. In order to understand the effects and possibly mitigate their consequences, it is necessary to increase and improve the environmental monitoring of the ocean. Optical properties of natural waters within the visible spectrum is closely linked to properties of phytoplankton, the foundation of oceanic ecosystems, as well as other particles on the micrometer and sub-micrometer scale in the water mass. Optical measurements can thus give us valuable information about the particle content of the water and the state of the ecosystem.

The volume scattering function (VSF) is a fundamental optical property describing how much light is scattered by a medium and in what direction the light is scattered. In natural waters, by far most of the light is scattered in the very forward direction, which makes it technically challenging to measure the VSF. The LISST-VSF is the first commercially available instrument for field measurements of the VSF over a large angular domain. To trust the measurements, it is important to validate the performance of instrument and identify any error sources, in particular the valid range of the instrument, given that scattering coefficients of natural waters can span three orders of magnitude.

In this thesis, I have characterised LISST-VSF measurements using both *in situ* measurements of highly contrasting water types, controlled laboratory measurements, and Monte Carlo simulations of instrument geometry. Similar aspects have been investigated for the LISST-200X, which measures the VSF at angles $0.04\text{-}13^\circ$ at 670 nm.

In Paper I, these two instruments are calibrated and validated using polymer beads and *in situ* measurements spanning from clear waters on the North Pole to highly turbid glacial meltwater. The measurements demonstrated that due to instrument design, the LISST-200X only gives valid scattering measurements in moderate-to-turbid waters. The LISST-VSF gives valid measurements also in clear waters (however with a loss in precision), but is limited by multiple scattering errors in more turbid waters.

Multiple scattering effects on LISST-VSF measurements are investigated in detail in in Paper II and III. For this purpose, a Monte Carlo simulation was developed and validated with experimental data, and subsequently used to simulate LISST-VSF measurements with Fournier-Forand and Henyey-Greenstein phase functions. We demonstrated that the multiple scattering can yield uncertainties of 10% when the scattering coefficient is 1 m^{-1} , which significantly restricts the accurate measurement range of LISST-VSF. LISST-200X is less affected by this error due to its shorter path length.

Scattering can be an error source for other optical measurements as well. In Paper

IV, we attempt to correct *in situ* depth profiles of absorption coefficients measured with the ac-s instrument using VSF measurements collected with the LISST-VSF in coastal waters. We show that this method does not show a clear and consistent improvement over existing methods, which are simpler to use but make strong assumptions about absorption and scattering properties. The discrepancies in the VSF correction can be attributed to several different confounding factors, such as spatial variability and multiple scattering, which are exceedingly propagated to the corrected absorption values. Nevertheless, VSF measurements are found useful to analyze the scattering error. We show that the VSF between 5-90° can contribute significantly to the scattering error, depending on the phase function and the reflectance efficiency of the reflective tube. Moreover, by simulating the VSF wavelength-dependency using Mie theory, we show that particle sub-populations with diameters close to the wavelength can explain why scaling the scattering error with the scattering coefficient sometimes fails.

List of papers

This thesis consists of an introductory part and four scientific papers.

1. Sandven, H., Kristoffersen, A. S., Chen, Y. C., and Hamre, B., (2020) *In situ measurements of the volume scattering function with LISST-VSF and LISST-200X in extreme environments: Evaluation of instrument calibration and validity*, Optics Express **28(25)**, 37373-37396.
2. Ugulen, H. S., Sandven, H., Hamre, B., Kristoffersen, A. S., and Sætre, C., (2021) *Analysis of multiple scattering errors in LISST-VSF volume scattering function measurements using Monte Carlo simulations and experimental data*, Optics Express **29(8)**, 12413-12428.
3. Ugulen, H. S., Sandven, H., Hamre, B., Kristoffersen, A. S., and Sætre, C., (2021) *Efficient Monte Carlo simulations reveal significant multiple scattering errors in underwater angular scattering measurements*, Optics Express (Submitted, October 2021)
4. Sandven, H., Petit, T., Chen, Y. C., Kristoffersen, A. S., Erga, S. R., and Hamre, B., (2021) *Into treacherous waters: Corrections of ac-s absorption measurements in coastal waters using volume scattering function measurements*, Optics Express (Submitted, September 2021)

I was also part of the following paper, which is not included in the thesis:

- Petit, T., Hamre, B., Sandven, H., Röttgers, R., Kowalczyk, P., Zablocka, M., and Granskog, M. (2021) *Inherent optical properties and optical characteristics of dissolved organic and particulate matter in an Arctic fjord (Storfjorden, Svalbard) in early summer*, Ocean Science (Preprint).

Contents

Scientific environment	i
Acknowledgements	iii
Abstract	v
List of papers	vii
1 Introduction	1
2 Scientific background	5
2.1 A short view back to the past	5
2.2 The changing marine environment	7
2.3 Inherent optical properties	8
2.3.1 Scattering	9
2.3.2 Absorption	15
2.3.3 Radiative transport	16
2.4 Instrumentation platforms	18
3 Instrument characteristics and methods	21
3.1 Characteristics of LISST instruments	23
3.1.1 Ring detector	23
3.1.2 Eyeball detector	26
3.2 Monte Carlo simulations of optical instrumentation	30
3.3 LISST error sources	32
3.4 How scattering affects absorption measurements	36
4 Introduction to the papers	41
5 Concluding remarks and outlook	45
6 Scientific results	63

Chapter 1

Introduction

In 2015, scientists discovered that the estimated number of trees on Earth, 400 billion, was a severe underestimation (Crowther *et al.*, 2015). By comparing satellite data with on-the-ground tree counting in various regions, they uncovered that the global number of trees was nearly an order of magnitude larger, approximately 3 trillion trees. In the same study, the authors also found that this number has fallen with about 46% since the beginning of human civilization. Another study determined that there is now nearly an order of magnitude more humans (in biomass) than all wild mammals combined (Bar-On *et al.*, 2018). Humans are greatly affecting the natural environments on Earth, and monitoring the biosphere accurately is a considerable challenge to this day. Increased and improved observations of the Earth are vital to understand and possibly mitigate ecological changes due to climate change or other environmental disruptions (Guo *et al.*, 2015; Ryabinin *et al.*, 2019).

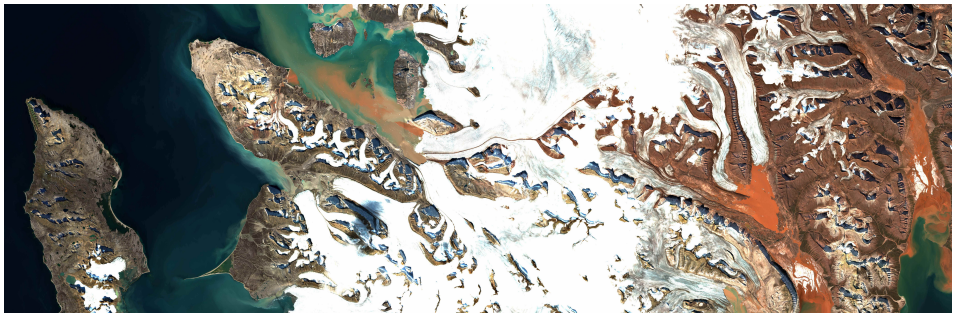


Figure 1.1: A Sentinel-2 ocean color image (color-enhanced) shows the considerable impact terrestrial run-off have on the surrounding coastal waters in the Arctic archipelago of Svalbard, Norway. The Arctic region is already strongly affected by climate change, and fundamental ecological changes are expected in the upcoming decades due to decreasing sea-ice and glaciers.

The ocean covers 71% of the surface of the Earth and is of great economic and social value in addition to its immeasurable ecological importance (Costanza, 1999). While the ocean may seem unchangeable and limitless in size, it can be and is affected by human activity. Ocean resources can be depleted, pollution disrupts the ocean environment, and anthropogenic climate change has a wide range of physical and chemical manifestations in the ocean, leading to cascading consequences throughout the ocean

ecosystem. However, ocean environments have been severely under-sampled, especially the biogeochemical properties (Claustre *et al.*, 2020). Thus, there is a knowledge gap concerning the sustainable human activity in the ocean. How can we utilize the ocean without damaging it? United Nations has proclaimed a Decade of Ocean Science for Sustainable Development from 2021 to 2030, aiming to narrow this knowledge gap (Ryabinin *et al.*, 2019). Knowledge of the ocean is stated as a "pre-requisite to the development of sustainable ocean economic policies and ecosystem-based management. [...] One cannot manage what one cannot measure."

Our monitoring of biogeochemical properties and ecosystem dynamics of the ocean is less developed than of physical quantities such as temperature, salinity, waves and currents (Claustre *et al.*, 2020). The physical properties are measured with instrumentation validated to very high accuracy, which can be deployed on a large variety of sensor platforms. The measurements are used to understand processes and trends, and assimilated into advanced numerical models for ocean circulation that are built on decades of theoretical and observational research (Johnson *et al.*, 2021). Ocean circulation is thus well-constrained within the field of physical oceanography, meanwhile the biogeochemical dynamics of the ocean require inherently an interdisciplinary approach. There are many more variables involved, which have complex relationships and are often difficult to measure even in a laboratory. Optical measurements have contributed greatly to the current knowledge on primary productivity and the biological carbon pump of the ocean, especially through the use of satellite observations starting in the 1970s (Blondeau-Patissier *et al.*, 2014). We have also learned a lot about the relationships between optical and biogeochemical properties through shipborne surveys, which has formed the foundation for satellite observations using visible light, *ocean color remote sensing*. In the past decade, optical measurements have been increasingly deployed on autonomous platforms, which opens up new regions of the ocean for environmental monitoring using optics. Monitoring of coastal regions may benefit greatly from ocean color satellite observations, but coastal waters are considerably more optically complex and thereby more difficult to measure accurately than the open ocean.

Absorption and scattering govern underwater light propagation (Mobley, 1994). These inherent optical properties (IOPs) are difficult to measure *in situ* with high detail and accuracy. The fundamental scattering property is the volume scattering function (VSF), which describes how much light is scattered in each direction. This is a multidimensional property depending both on scattering angle and wavelength, and is particularly challenging to measure due to the extreme dynamical range present in a single measurement. The particulate VSF dominates scattering in the ocean and is governed by particle size, composition and inner structure. VSF measurements may thus provide detailed observations of suspended particles in the ocean. Due to the technical challenges, instrumentation for measuring the full VSF *in situ* has been scarce, but a recently released commercial instrument, the LISST-VSF (Sequoia Sci.), can measure the VSF across a wide angular domain *in situ* down to a depth of 50 metres (Slade *et al.*, 2013). These measurements will also improve ocean color satellite observations and other *in situ* optical measurements, which are more routinely measured. However, these new instruments need to be validated and characterised to know that the measurements are robust and accurate. *In situ* optical measurements often demand assumptions about the optical properties of the water and involve confounding factors and uncertainties, which must be tested and identified.

In this thesis, I have evaluated LISST-VSF and LISST-200X measurements across the entire validity range of the instrument. This includes identifying a variety of possible error sources *in situ*, establishing measurement limits and replicating validation studies within the measurement range. Fieldwork has been conducted in the central Arctic Ocean, from the marginal ice zone to the ice-covered North Pole, and in coastal waters in Western Norway and Svalbard, covering almost the entire range of scattering properties possible to find in natural waters. Laboratory bench-top measurements with a wide range of polymer bead sizes and concentrations have also been used to calibrate and validate instrument performance. A Monte Carlo simulation of the LISST-VSF instrument has been developed and used to investigate effects of multiple scattering on the VSF measurements. In addition, LISST-VSF measurements have been used to correct depth-resolved absorption measurements made with the widely used ac-s instrument. This correction method should in principle correct the absorption without any assumptions about the IOPs. It is compared with simpler empirical models in optically and spatially complex coastal waters.

Objectives and structure

The main objective of this doctoral study is to assess whether VSF measurements with the recently released LISST-VSF and LISST-200X instruments are trustworthy and accurate in a wide range of natural waters.

To address and expand upon the main objective, the doctoral study is organized into the following secondary goals:

- **Goal I:** Find valid measurement ranges of the LISST-VSF and LISST-200X in natural waters.
- **Goal II:** Identify key error sources in the scattering measurements of the LISST-VSF and LISST-200X instruments.
- **Goal III:** Quantify the effect of multiple scattering on the measured volume scattering functions.
- **Goal IV:** Assess whether measured volume scattering functions be used to correct ac-s absorption measurements, in particular depth profiles. Does this correction method yield more accurate absorption coefficients than existing empirical methods?

The thesis is outlined as follows. First, there is section detailing the scientific background of the study, including a brief history of marine optics, why it is more important than ever to monitor the ocean, and the state-of-the-art of *in situ* scattering and absorption measurements in the ocean. A short review on how absorption and scattering properties are connected to the observed light propagation in the ocean is given, in addition to an overview of different measurement platforms. Then follows a description of the LISST instruments and how the scattering data is processed into volume scattering measurements, and their error sources. Furthermore, I include a treatment of how scattering causes inaccuracies in ac-9/s measurements and how they are corrected. Afterwards, an introduction to each of the four publications is given, before I give my concluding remarks of the doctoral study and my outlook for further research. The final part of the thesis is the scientific results, consisting of the four publications.

Chapter 2

Scientific background

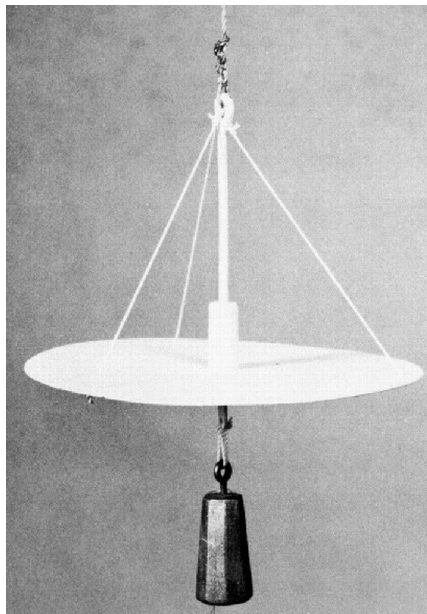


Figure 2.1: The first instrument for measuring underwater optics was the simple Secchi disk from the 19th century. Photograph from Pitarch (2020), used with permission.

2.1 A short view back to the past

Marine optics is a relatively young branch of science, being on the intersect between physics and oceanography, but observations of the transparency of water have been found in ship logbooks from many ocean explorations throughout the centuries (Pitarch, 2020). During a Russian expedition to find the Northeast passage in 1815-1818, the German naturalist Adelbert von Chamisso found a method of measuring water transparency quantitatively by lowering a whitened disk down to the depth to where it vanishes in the surrounding water (Wernand, 2010). The method was adapted by several other ocean expeditions in the 1800s, using everything from painted iron pots to

dinner plates as optical instrumentation (Wernand, 2010). Angelo Secchi, most famous as a founding figure of modern astronomy, standardised and made rigorous studies of the method in 1865 and 1866 (Chinnici and Consolmagno, 2021; Pitarch, 2020). The measurement is henceforth known as the *Secchi depth* and is measured using a *Secchi disk*.

The Challenger expedition of 1872-1876 is considered the birth of modern oceanography with systematic surveys of the large ocean, measuring important ocean currents such as the Gulf Stream (Apel, 1987). Another remarkable transition point in the history of ocean exploration was the Fram expedition of 1893-1896. The expedition would explore one of the last white spots on the world map by crossing the Arctic Ocean, and hopefully reach the North Pole on the way. Earlier it was actually theorized that the Greenland landmass reached all the way to the North Pole. However, they found the Arctic Ocean to be deeper than their 3400 metres of measurement wire, and they did novel measurements of salinity using electrical conductivity (Baker, 1981; Huntford, 1997). Nansen's observations of wind and ocean currents in the high Arctic led Swedish oceanographer Vagn Walfrid Ekman to apply classical fluid mechanics to the atmosphere-ocean boundary, and found that wind and the Coriolis force can drive circulation in upper ocean (Apel, 1987).

The two world wars accelerated the development of ocean science. Submarines and amphibious operations made it important to have more knowledge of the ocean than the enemy, and successful developments such as the sonar and wave propagation paved the way for ambitious and technologically advanced ocean science after World War II (Apel, 1987; Munk, 2013). Marine optics, or optical oceanography, also advanced into the modern era during the post-war decades. Some measurements on the vertical and spectral distribution of the underwater light field (apparent optical properties, see 2.3.3) were done in the inter-war years, in particular after the discovery of the photoelectric effect (Antoine *et al.*, 2014; Jerlov, 1968). There were even a few studies on light scattering and transmittance in water, but the research was experimental in nature and had often military applications.

In the 1960s, there was a change in direction towards more fundamental research on the optical properties of natural waters, including detailed measurements on absorption and scattering properties (Antoine *et al.*, 2014; Zaneveld, 2013). Theoretical or empirical relationships were found between the first fragmented IOP measurements and ocean constituents like suspended particles and water itself, for instance by applying electromagnetic theory to particle properties like size and refractive index (Antoine *et al.*, 2014). Considerable progress was also made on computing the underwater light field using radiative transfer modelling. This became even more relevant after the launch of the Coastal Zone Color Scanner in 1978, the first radiometer designed for satellite remote sensing of ocean color (Hovis *et al.*, 1980).

In 1970, Clarke *et al.* demonstrated that it was possible to estimate chlorophyll concentration from surface reflectance measurements made from an aircraft. After the emergence of remote sensing using satellites, global observations of chlorophyll could be made from satellite imagery. Ocean color remote sensing (visual spectrum satellite observation) is now widely used for environmental monitoring (Blondeau-Patissier *et al.*, 2014). In the past decades, a considerable part of the research conducted within marine optics has been directed towards validating and improving the accuracy of these observations (Werdell *et al.*, 2018). A wide assortment of advanced *in situ* optical in-

strumentation has also been developed to fill the knowledge gaps of the optical ocean, see section 2.3 (Moore *et al.*, 2009). Nevertheless, the simple Secchi-disk measurements are still useful 200 years after their invention, especially when looking at long-term trends connected to climate change (Opdal *et al.*, 2019).



Figure 2.2: Phytoplankton and other oceanic particles are now routinely observed from space with satellites measuring visible light, here an illustration showing the Sentinel-3 satellite passing over Barents Sea. Copyright: ESA/ATG medialab.

2.2 The changing marine environment

Despite its somewhat opaque and homogeneous appearance to a person on a ship or on the shore, the ocean is a highly diverse and dynamic environment driven by a large number of complex physical processes such as the Coriolis force, differences in radiative forcing, interactions with the atmosphere and the ocean bottom, tidal forces, and internal processes such as viscous forcing and diffusion (Apel, 1987). The processes span spatial scales from global to microscopic (Basterretxea *et al.*, 2020).

Life exists at all depths of the ocean, from the surface to the bottom of the Mariana Trench more than ten thousand metres below (Takami *et al.*, 1997). The majority of marine life is concentrated near the surface where light is available for photosynthesis. Microscopic marine plants, phytoplankton, forms the backbone of the marine ecosystem and contributes about half of the global primary production. On the other hand, only $\sim 1\%$ of the plant biomass in the biosphere is phytoplankton, and the entire phytoplankton biomass is renewed (produced and consumed) every 2-6 days (Behrenfeld, 2014; Behrenfeld and Falkowski, 1997). The rapid turnover makes phytoplankton highly sensitive to environmental changes compared to other types of biomass, and because the biomass consists of microscopic particles diffused in the water mass, it is difficult to monitor (Behrenfeld *et al.*, 2016). Phytoplankton biomass can be consumed by other organisms, or it can sink down to the bottom of the deep ocean, acting as a carbon sink. The biological carbon pump of the ocean is a complicated process and there are still considerable knowledge gaps (Siegel *et al.*, 2016).

The ocean is changing. In the past decades, an increase in ocean temperatures have been observed globally (Wijffels *et al.*, 2016), as well as a rise in average sea-level

(*Nerem et al.*, 2018), a dramatic loss of sea-ice (*Onarheim et al.*, 2018; *Polyakov et al.*, 2017), ocean acidification (*Doney et al.*, 2009), and increased stratification (*Li et al.*, 2020). Stratification inhibits transportation processes in the ocean, consequently will a stronger stratification yield less nutrients in the upper ocean (*Moore et al.*, 2018), less dissolved oxygen (*Keeling et al.*, 2010), and thus dramatically changed conditions for marine ecosystems (*Behrenfeld et al.*, 2016; *Doney et al.*, 2012). All of these observed changes are manifestations of anthropogenic climate change (*IPCC*, 2021). Human activity is also disrupting marine ecosystems in other ways, for instance through pollution and over-fishing (*Crain et al.*, 2008).

Coastal environments are of particular importance both ecologically, economically and socially, with their large biodiversity and often high population densities (*Martínez et al.*, 2007). Coastal waters interact with land and the bathymetry, for instance through terrestrial run-off or coastal upwelling, which adds additional layers of complexity to our understanding of the physical and biological processes (*Cloern et al.*, 2014; *Johnson et al.*, 1999). Terrestrial run-off and upwelling processes provide important nutrients for ecosystems, but also suspended particles that inhibit light from penetrating deep into the water masses. The euphotic zone depth, the maximum depth considered to have enough light to support photosynthesis, ranges from less than 5 meters to 200 meters depending on the water constituents (*Lee et al.*, 2007; *Morel et al.*, 2007). The underwater light environment has also been impacted by climate changes. An increase in precipitation has led to more terrestrial discharge from rivers or glaciers, yielding higher concentrations of particulate and dissolved matter in coastal waters, which in turn increases the light attenuation (*Frigstad et al.*, 2020). This phenomenon is called *darkening* and is expected to have wide-ranging consequences in coastal marine ecosystems (*Opdal et al.*, 2019).

The ocean is a diverse and dynamic environment, both on shorter and longer time scales. It is also chronically under-sampled (*Claustre et al.*, 2020). The transport of light into the ocean is crucial for marine ecosystems, but marine life also modifies the light transport, together with other types of particles and dissolved matter. It is consequently important to understand optical properties of natural waters and their optically active constituents, both to know more about the interaction between light and the ocean environment and to measure properties of the ocean more effectively.

2.3 Inherent optical properties

Consider a beam of light passing through a small volume of water, which contains various particles or dissolved substances. What can happen to the light in this beam? Most of the light will pass through undisturbed. Some of the light will change direction, most likely due to particles in the water. This is called scattering. Another fraction of the light will be absorbed by the water volume, such that radiant energy is transformed into thermal or chemical energy. Absorption and scattering are the primary processes for radiative transport in the ocean (*Mobley*, 1994). Other minor processes include fluorescence, bioluminescence and Raman scattering. The principle of radiative transfer modelling is to divide the ocean into many small water volumes with fixed absorption and scattering properties, and from that simulate the propagation of light through the water column. Accurate measurements of absorption and scattering prop-

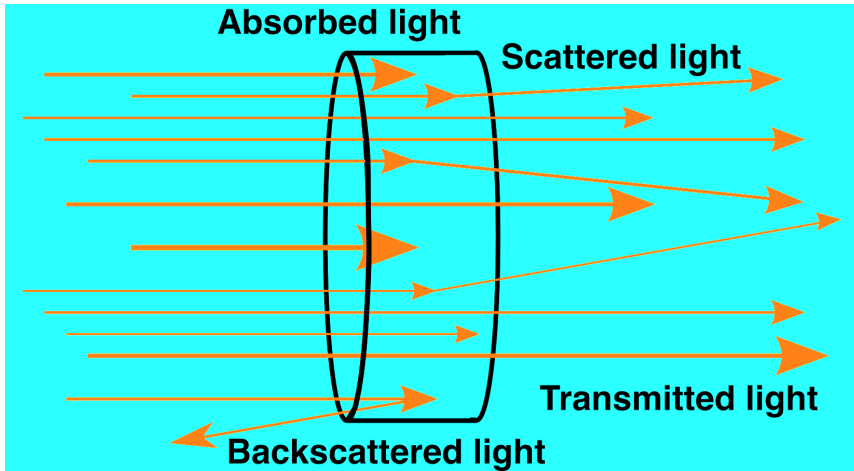


Figure 2.3: The major physical processes for light transport in natural waters. Light passing through a (very small) volume of water can either be scattered, absorbed, or transmitted.

erties are consequently of high importance for modelling the behaviour of light in the ocean. Moreover, absorption and scattering properties are governed by the properties of particles and dissolved matter in the water, as well as water itself. This means that IOP measurements can serve as useful proxies for observing the state of the ocean.

2.3.1 Scattering

Scattering is a phenomenon deeply engrained into electromagnetic theory (Mishchenko, 2009), but also of uttermost importance in environmental optics. All natural light visible around us except direct sunlight is due to scattering. When describing nature we need more simplified models compared to those found in electromagnetic theory, and typically electric and magnetic components are neglected. The most fundamental definition of scattering commonly given within optical oceanography literature is the volume scattering function $\beta(\theta, \lambda)$ (or VSF). The VSF describes the magnitude and angular distribution of scattered light from an arbitrary light beam. It is mathematically defined as

$$\beta(\theta, \lambda) = \frac{\partial I}{E \partial V}. \quad (2.1)$$

Here, E is the irradiance of an incident beam entering an infinitesimal volume dV , dI is the radiant intensity of the scattered light in the direction θ . In natural waters, scattering is assumed to occur due to randomly oriented particles. Consequently, the VSF depends only on θ , the angle between the direction of the incident light and the direction of the scattered light, and the wavelength λ .

In natural waters, the VSF is typically extremely forward-peaked (up to $\sim 10^7$ times larger at small angles than at large angles), meaning that most of the scattered light will barely change direction. Nevertheless, large-angle scattering is disproportionately important for ocean color remote sensing, which depends on scattering causing water-leaving radiances that are detectable from satellite (Werdell *et al.*, 2018). The shape and

properties of the backward VSF ($>90^\circ$) have thus been of considerable research interest (Mobley *et al.*, 2002; Stramski *et al.*, 2004; Sullivan and Twardowski, 2009; Zhang *et al.*, 2021). The shape of the full VSF is often assumed to have a low spectral dependence, while the magnitude often vary with wavelength. The scattering coefficient b describes the VSF magnitude, and is calculated from integrating the VSF over all angles,

$$b(\lambda) = 2\pi \int_{0^\circ}^{180^\circ} \beta(\theta, \lambda) \sin \theta d\theta. \quad (2.2)$$

The scattering coefficient is a somewhat more intuitive physical parameter. Over a certain path length L , the fraction of a light beam which has *not* been scattered is given by e^{-bL} . This is the Beer-Lambert law for scattering. Due to the forward-peaked VSF in natural waters, most of the scattering coefficient will be decided by the small-angle VSF (less than $\sim 10^\circ$). The shape of the VSF is commonly described using the phase function,

$$p(\theta, \lambda) = \frac{\beta(\theta, \lambda)}{b(\lambda)}. \quad (2.3)$$

Furthermore, the backscattering coefficient is computed by integrating VSF over all angles above 90° ,

$$b_b = 2\pi \int_{90^\circ}^{180^\circ} \beta(\theta) \sin \theta d\theta, \quad (2.4)$$

and the shape of the backward VSF is often described by the shape factor $\chi_p(\theta) = b_b/2\pi\beta(\theta)$.

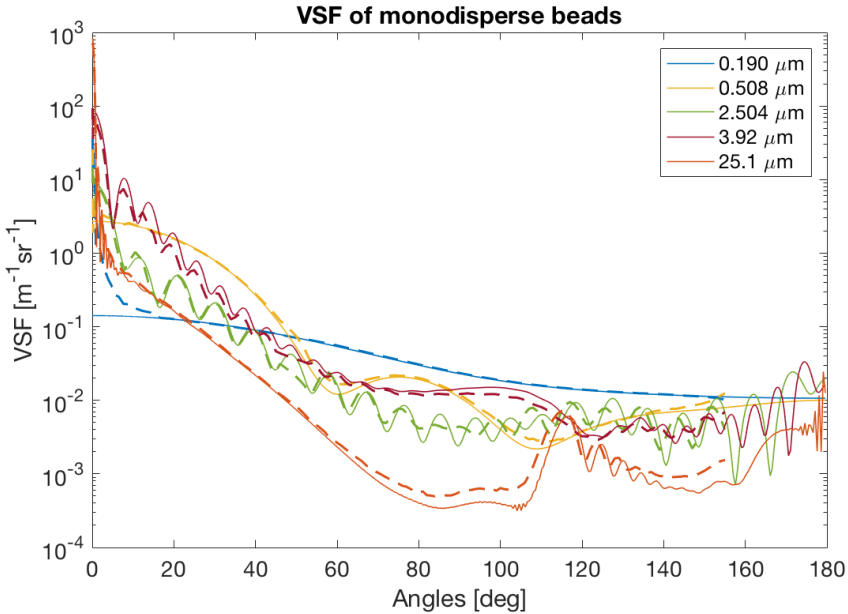


Figure 2.4: The VSF of monodisperse polymer beads at 515 nm plotted together with corresponding LISST-VSF measurements. The VSF varies considerably with particle size.

Given that the structure, size and composition (real and imaginary refractive index) is known, the VSF and absorption of a single particle can be computed using electromagnetic theory (Mishchenko *et al.*, 1996). This is however far too demanding and impractical for most purposes. A very practical theoretical model is Mie scattering, which is the analytical solution of scattering from homogeneous spheres (Mie, 1908). It depends only on particle diameter and concentration, the refractive index of the spheres and the surrounding medium, and the vacuum wavelength of the incoming light. It has been shown to be accurate for monodisperse polymer spheres, note the variation with particle diameter in Figure 2.4. The relatively cost-effective computation means that it can be used to model spectral scattering from distributions of particles (Boss and Pegau, 2001; Twardowski *et al.*, 2001; Ulloa *et al.*, 1994), as well as computing particle size distributions from inversion of scattering measurements (Agrawal and Pottsmith, 2000). The validity of the Mie scattering for modelling ocean particles has been challenged, as spheres are generally not representative of oceanic particles, but it has shown a surprising ability to retrieve physical characteristics of non-spherical particles (Clavano *et al.*, 2007; Karp-Boss *et al.*, 2007). In the backward direction, structural complexity of phytoplankton cells has been found to explain observed discrepancies between measured backscattering in the open ocean and predictions by Mie scattering (Organelli *et al.*, 2018).

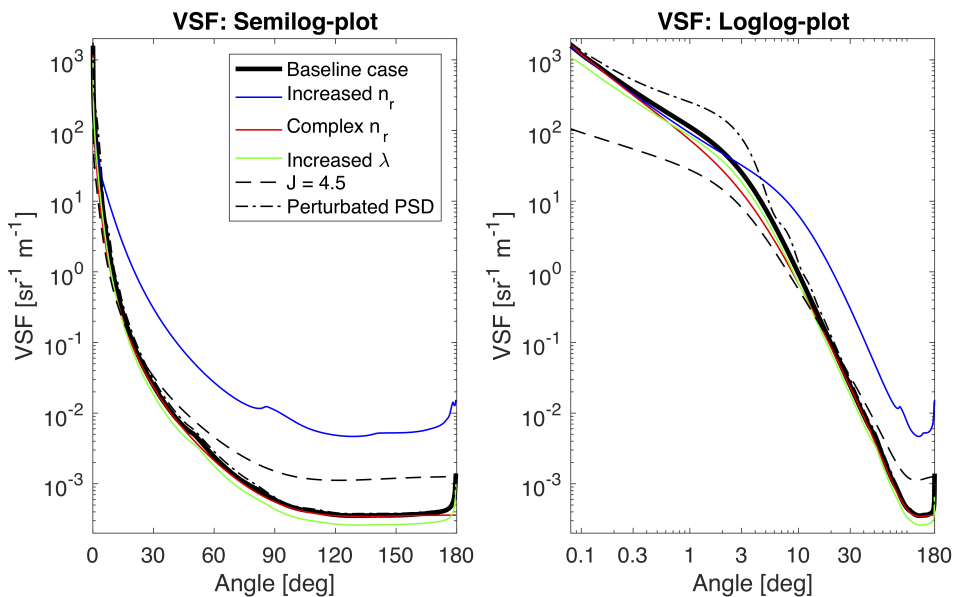


Figure 2.5: Illustration plot of the key governing factors for the VSF which can be modelled with Mie theory. The black line shows the baseline case, with Junge slope $J = 3.8$, and relative refractive index $n = 1.03$. The relative refractive index is increased to 1.1 for the blue line, the red line shows the VSF if an imaginary refractive index is introduced ($n = 0.001$) and the green shows the VSF if the laser wavelength is increased to 700 nm. The two dashed black lines shows the VSF if (1) the Junge slope is increased to $J = 4.5$ yielding more small particles, or (2) a subpopulation of $5 \mu\text{m}$ particles (median diameter) has been added.

Mie scattering modelling can aid in understanding the effects of four different pa-

rameters on the VSF; the particle size (distribution), the real (bulk) refractive index, the imaginary (bulk) refractive index, and the wavelength. These effects are illustrated in Figure 2.5. The baseline case (black line) is based on a power law-distribution (Junge slope $J = 3.8$), with a relative refractive index $n = 1.03$, and the wavelength 515 nm. A power law-distribution means that the number concentration of particles with diameter D follow the distribution $n(D) \propto D^{-J}$. The resulting VSF is reasonably realistic for natural waters. When the refractive index is increased to 1.1 (blue), there is more scattering at all angles larger than 3° . Consequently, backscattering coefficients can vary considerably with the refractive index. The imaginary refractive index (red line) have more subtle effect on the VSF, shown in the figure to slightly decrease scattering between 0.3° and 10° , however absorption effects on the VSF can vary considerably with particle size (Slade and Boss, 2006).

The particle size distribution affects the VSF at all angles. A smaller average particle size ($J = 4.5$, dashed line) yields both an increase in backward scattering and decreased forward scattering in Figure 2.5. On the other hand, by adding a narrowly log-normal distributed sub-population of $5 \mu\text{m}$ median size particles to the baseline case, we see an increased VSF within a relatively narrow angular domain. Forward scattering of visible light is particularly sensitive to the particle size of particles within the size range $\sim 1\text{-}300\mu\text{m}$, which forms the underlying principle for measuring particle size distributions using LISST-instruments. According to Mie theory, the VSF do not actually depend on particle size, but the size parameter $x = 2\pi D n_w / \lambda$, where D is the particle diameter, n_w is the refractive index of water, and λ is the vacuum wavelength of the incident light. Thus, a narrow size distribution may actually depend strongly on the wavelength. However, for power-law size distributions the wavelength-dependence is relatively weak, as seen in Figure 2.5. This is consistent with the Fournier-Forand phase function, which is a widely used approximate model of the VSF in natural waters (Fournier and Forand, 1994). It is based on the assumption that particles follow a power-law distribution, and yields a spectrally independent phase function which is governed by the Junge slope and bulk refractive index.

Our current knowledge about the full VSF in the ocean comes from a relatively limited set of measurements. Few instruments have been available, and *in situ* measurements have been difficult to conduct with the existing instrumentation. The largest technical challenge when designing a VSF instrument is the dynamical range of the VSF, making the instruments impractically large or yielding a slow sampling rate (Slade *et al.*, 2013). Thus, the early VSF measurements made by Petzold in the 1970s has had a prominent position within the ocean optics community, which otherwise has relied mostly on approximate models of the VSF (Petzold, 1972). The Multispectral Volume Scattering Meter (MVSM) is a prototype scattering meter measuring the VSF at eight different wavelengths, but only above 10° , which excludes a large portion of the scattering (Lee and Lewis, 2003). The Multi-Angle Scattering Optical Tool (MASCOT) is another *in situ* VSF instrument, measuring at 658 nm between $10\text{-}170^\circ$ (Sullivan and Twardowski, 2009). The only commercially available instrument for measuring the VSF over a large angular domain is the LISST-VSF. It measures the angular domain $0.09\text{-}150^\circ$ at a single wavelength, 515 nm, down to a depth of 50 m. Other LISST-instruments can give VSF measurements of forward scattering ($<15^\circ$), but requires specialized calibration for correct absolute values (Slade and Boss, 2006).

On the other hand, optical instruments for measuring other scattering properties

have been widely used for many years. Attenuation, the sum of the scattering and absorption coefficient, is in principle easy to measure as it only requires accurate measurements of an incident and transmitted light beam, and thus many attenuation meters (transmissiometers) exist. As scattering is the dominating physical process compared to absorption in parts of the visible spectrum, the scattering coefficient may be approximated by the measured attenuation coefficient at certain wavelengths. Instruments like the Sea-Bird ac-9 or ac-s measure both the absorption and attenuation coefficient over many wavelengths, enabling more accurate scattering coefficient measurements by computing $b = c - a$ (Twardowski *et al.*, 1999).

The backscattering coefficient is another commonly measured optical property, in particular after the inclusion in the biogeochemical-Argo program (Roemmich *et al.*, 2019). However, for backscattering sensors the measured property is actually not the backscattering coefficient, but a VSF value across a narrow angular domain, typically in the region 115° to 140° . Studies have shown that the shape of the VSF varies relatively little in this angular region, and there is thus a strong relationship between the measured VSF and the backscattering coefficient (Boss and Pegau, 2001; Chami *et al.*, 2006a; Oishi, 1990; Sullivan and Twardowski, 2009; Zhang *et al.*, 2021). Based on this, several commercial backscattering meters have been developed, such as the ECO-BB (WET Labs) and Hydrosat (HOBILabs), which measures the backscattering multi-spectrally.

Turbidimeters are similar to backscattering sensors, but measure the scattering close to 90° (correspondingly called side-scattering), normally at relatively long wavelengths such as 860 nm. Turbidity measurements are typically not calibrated to any physical properties, but to empirically determined units such as NTU or FTU. A recent study by Wong *et al.* (2020) demonstrated that a turbidimeter can be used to measure the backscattering coefficient by finding a relationship between NTU and b_b from *in situ* and laboratory measurements. However, both VSF measurements and theory suggest that the relationship between side-scattering (VSF at 90°) and the backscattering coefficient is weaker than the relationship at 120° . Differences in particle composition and size distribution can lead to large uncertainties in the b_b -value derived from side-scattering. Nevertheless, turbidimeters persist as one of the most widely used environmental optics instrumentation due to their application for cost-effective water quality measurements.

Scattering measurements have been found to be useful and accurate proxies for different particulate properties in natural waters. Several studies have shown that suspended particulate matter (SPM) concentration has strong relationships with the attenuation, scattering and backscattering coefficient as well as turbidity (Boss *et al.*, 2009a; Neukermans *et al.*, 2012; Reynolds *et al.*, 2016). Moreover, the attenuation coefficient often follows a power law dependence on wavelength,

$$c_p(\lambda) \propto \lambda^{-\gamma}. \quad (2.5)$$

The spectral slope γ has been found to correlate with particle size both through observations and in theory (Boss *et al.*, 2001; Slade and Boss, 2015). A similar relationship has also been observed for the backscattering coefficient (Slade and Boss, 2015). However, a recent study by Organelli *et al.* (2020) shows that these relationships are not necessarily valid in all ocean environments. Whether the backscattering ratio b_b/b is wavelength-independent or not has been the subject of some debate in the ocean optics community, with several studies supporting wavelength-independence (Huot *et al.*,

2008; Slade and Boss, 2015; Ulloa et al., 1994; Whitmire et al., 2007, 2010), while other studies show that there can be non-negligible spectral dependence (Antoine et al., 2011; Chami et al., 2005; McKee et al., 2009; Soja-Woźniak et al., 2019; Sun et al., 2019). For the full VSF, a spectrally independent b_b/b strongly implies limited spectral variation of the phase function. By using the backscattering ratio together with the Junge slope (derived from the attenuation slope), the bulk refractive index can be estimated, enabling assessments whether the suspended particles consist of organic and inorganic matter (Twardowski et al., 2001). Other recent studies support the notion that the backscattering ratio is closely related to the particle composition (Soja-Woźniak et al., 2019; Sun et al., 2019).

Forward scattering has a strong relationship with particle size due to diffraction phenomena; Fraunhofer diffraction theory or anomalous diffraction can largely explain the forward scattering observed in natural waters (Agrawal et al., 2008; Agrawal and Pottsmith, 2000; Clavano et al., 2007; van de Hulst, 1981). Consequently, there has been considerable interest in developing inversion methods for estimating the particle size distribution from *in situ* scattering measurements, such as Laser In-Situ Scattering and Transmissometry (LISST) series of instruments (Sequoia Sci.). These instruments have been widely used over the past decades and validated for use in varied hydrographic environments (Agrawal et al., 2008; Agrawal and Pottsmith, 2000; Boss et al., 2018a; Felix et al., 2018). While providing considerably more detailed information than other optical measurements about particles on the micrometer scale, the LISST particle size distribution measurements approximates all particles in the ocean as sphere-like (only one parameter describes the size). Moreover, the estimates may contain artifacts due to particles smaller or larger than the measurement limit, and considers the relative refractive index to be invariant even though it may have a significant effect for smaller particles (Andrews et al., 2010; Davies et al., 2012).

As we have seen, a significant amount of information may be possible to obtain from parts of the VSF, or other scattering measurements. This implies that measurements of the full VSF can be used as a powerful optical tool for measuring suspended particle properties. While the LISST-instruments estimates particle size distributions from scattering at angles $\sim 0.1^\circ$ - 15° , relatively few studies have applied inversion methods to VSF measurements covering larger angular domains. In a series of articles, Zhang et al. (2011; 2012; 2013; 2014) and Twardowski et al. (2012) have developed inversion techniques for estimating subpopulations of oceanic particulate and dissolved matter, as well as bubbles. With more widely available VSF instrumentation, this method can be further developed and become a powerful tool for estimations of ocean constituents.

Looking beyond the normal VSF properties observed in natural seawaters, the ability of ocean constituents to polarize scattered light is growing subject of interest, in particular with upcoming remote sensing missions with capability of monitoring the polarized components of ocean color (Werdell et al., 2019). The LISST-VSF instrument can in fact measure linear and circular polarization properties of natural waters, however there are still few studies utilizing these measurements (Koestner et al., 2020; Slade et al., 2013). Further work is required for validating and characterizing LISST-VSF polarization measurements, as well as exploring the physical properties governing polarization.

2.3.2 Absorption

Absorption properties of ocean constituents have been measured extensively for many years due to its explicit relationship with photosynthesis. Similar to plants on land, phytoplankton converts light to chemical energy using chlorophyll pigments which absorbs light. Phytoplankton are microscopic organisms that cannot be seen with the naked eye, but their collective influence on the surface ocean can often be visible, even from space. By using remote sensing satellite products, the primary productivity of phytoplankton has been estimated to approximately equal to the primary productivity of terrestrial plants (*Field et al.*, 1998).

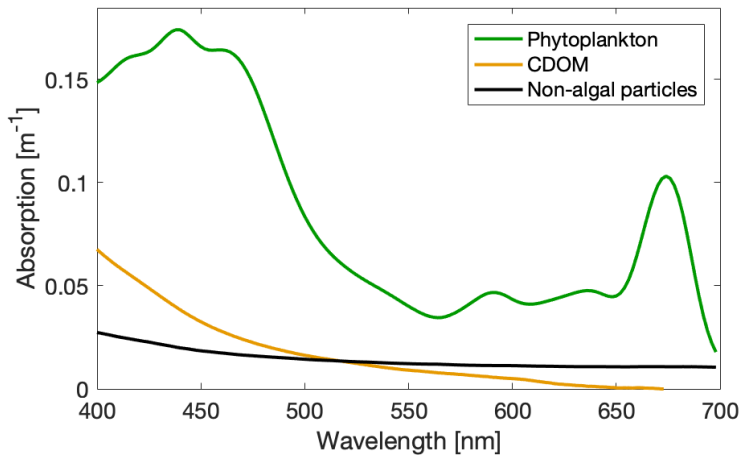


Figure 2.6: Wavelength-dependent absorption properties of phytoplankton, non-algal particles and colored dissolved organic matter (CDOM). These are measurements from a water sample collected during the UAK 2020 cruise (*Petit et al.*, 2021).

Chlorophyll pigments have very specific absorption spectra, the chlorophyll influence on measured absorption is often obvious even to untrained eyes. Other oceanic constituents have more subtle wavelength dependencies, see Figure 2.6. Non-water absorption in natural waters is considered to come from three types of optically active constituents, which are to some extent defined operationally from the measurement techniques. Colored dissolved organic matter (CDOM) is the constituent yielding non-water absorption of water that has been filtered through a 0.2 (or 0.7) μm filter (*Werdell et al.*, 2018). The absorption of CDOM typically follows an exponential curve,

$$a_{\text{CDOM}} = a_{\text{Ref}} e^{-S(\lambda - \lambda_{\text{Ref}})}, \quad (2.6)$$

where the spectral slope S can be linked to the origin of the particles (*Nima et al.*, 2019). The water constituents that does not pass the 0.7 μm filter is defined as particulate matter. The absorption properties of these particles are computed from measurements made on these samples, both before and after a bleaching process. This separates the absorption properties of pigmented and non-pigmented particulate matter. The former corresponds to phytoplankton absorption (which is removed by the bleaching), while the latter is defined as non-algal particle absorption. Non-algal particles absorb light similarly to CDOM, but with a different spectral slope and with often

non-negligible absorption at near-infrared wavelengths (Werdell *et al.*, 2018). Phytoplankton absorption is connected to the various pigments present, and can be used to characterize phytoplankton populations (Chase *et al.*, 2013). In the open ocean, concentrations and thereby absorption properties of the ocean constituents tend to co-vary, which enables retrieval of primary productivity from ocean color products (Bricaud *et al.*, 1998). By contrast, in optically complex waters characteristic of coastal environments, terrestrial input yields less interlinked concentrations of the water constituents (Blondeau-Patissier *et al.*, 2014; Mobley *et al.*, 2004). Consequently, more refined retrieval algorithms are needed for coastal waters. This requires extensive absorption measurements of high accuracy and resolution.

Laboratory absorption measurements of water samples has been conducted using benchtop spectrophotometers (as described above) since the 1980s, with refined instrumentation and well-characterized uncertainties (Werdell *et al.*, 2018). These measurements are however time- and resource-demanding, and are based on collecting water samples from discrete depths. Consequently, the spatial resolution is limited. *In situ* absorption measurements have by large been conducted using the ac-9 or ac-s instruments (Sea-Bird Sci.) in the past decades. Absorption and attenuation coefficients are measured with multi- (ac-9) or hyperspectral (ac-s) resolution with a sampling rate of ~ 4 Hz, enabling fine-scale resolution in profiling deployments (Twardowski *et al.*, 1999). The instruments have also been used in underway flow-through systems and mooring deployments, and by installing $0.2 \mu\text{m}$ filter cartridges on the inlet allows the dissolved matter absorption to be measured (Slade *et al.*, 2010). The ac-9/s absorption measurements have been used to estimate chlorophyll concentration in various oceans environments (Boss *et al.*, 2007; Dall'Olmo *et al.*, 2009; Liu *et al.*, 2018). Approaches to retrieve even more information using inversion methods have been tested (Ramírez-Pérez *et al.*, 2018). Most of the measurement uncertainties are well-characterized, including instrument drift and temperature and salinity corrections (Sullivan *et al.*, 2006; Twardowski *et al.*, 1999). However, the most significant error source, scattered light leading to errors in the absorption measurements, is still an ongoing area of research, in particular for use in coastal waters (Kostakis *et al.*, 2021; Röttgers *et al.*, 2013; Stockley *et al.*, 2017). Current correction methods require either strong assumptions about scattering and near-infrared absorption, or detailed knowledge about the (hyperspectral) VSF. This topic is covered in detail in Section 3.4.

2.3.3 Radiative transport

Given that we know the optical properties of the water column, in addition to the properties of the incident light (wavelength-dependent intensity and direction), we will be able to model the light field of entire water column. The light field is described by the radiance $L(\mathbf{x}, \theta, \varphi, \lambda)$, which can briefly be described as the intensity of light (units $[\text{W}/\text{m}^2\text{sr}]$) at the wavelength λ , in the direction given by the polar and azimuthal angles θ and φ , at the position \mathbf{x} in the water column. The radiance is an *apparent optical property* (AOP), a property which depends both on IOPs and the incident light field. Other AOPs such as irradiance can be computed from the radiance. These properties are measured using *passive measurements* of the natural light field due to the sun. When we compute the light field, we need to take into account both the internal ocean

properties and boundary conditions such as the ocean bottom, air-sea surface, and the atmosphere.

There are three main approaches for computation of radiative transport. The first is simplified analytical solutions from formulating the optical processes as a differential equation, namely the *radiative transfer equation* (RTE). These solutions were popular before the computer era, and require substantial approximations and very simple boundary conditions. They can nevertheless provide useful insights into the transport processes. For instance, Gershun's law (1939) can provide accurate estimates of the water absorption properties using passive optical measurements (Kostakis *et al.*, 2021).

The second approach is numerical solutions to the radiative transfer equation. Due to the vast limitations of the analytical solutions, numerically modelling has become by far the most used tool within ocean optics, especially when considering the atmosphere and the ocean as a coupled system, which is important for remote sensing (Jin and Stamnes, 1994). It is however computationally intensive, in particular for three-dimensional geometries or time-dependent processes (Stamnes and Stamnes, 2016).

The third approach is Monte Carlo methods. Here, a statistical interpretation of absorption and scattering is used to conduct (in practice) ray-tracing of the light, which are consistent with Monte Carlo methodology where a large number of simulations are run to find probability distributions, see section 3.2. It is easily extended to three-dimensional geometries (Stamnes and Stamnes, 2016), making the method valuable for simulating instruments, see for instance Doxaran *et al.* (2016); Kirk (1992); Piskozub *et al.* (2004). On the other hand, Monte Carlo has only been used in a limited number of studies for solving the radiative transfer equation in the ocean, see Gordon and Boynton (1998); Zhai *et al.* (2008), but it has been used extensively for LIDAR studies (Liu *et al.*, 2019; Poole *et al.*, 1981).

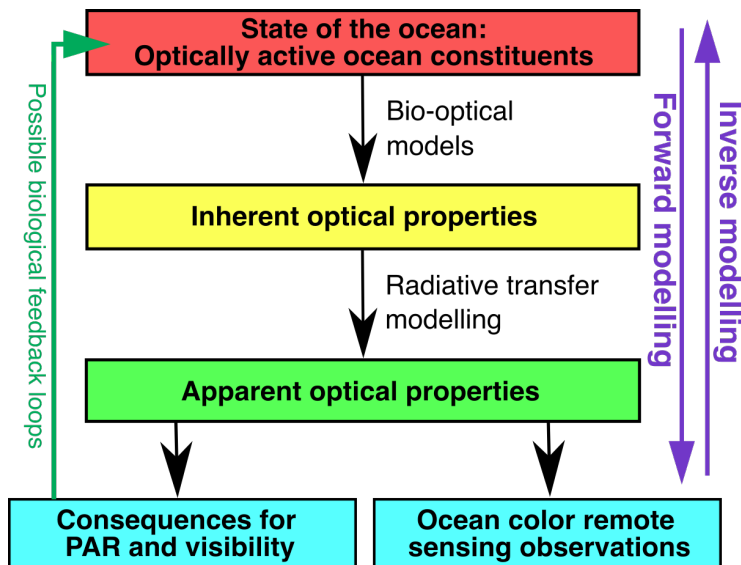


Figure 2.7: Inherent and apparent optical properties are connected to the state of the ocean (properties of optically active constituents) and ocean color satellite observations through the illustrated framework.

Inherent and apparent optical properties form a well-defined framework for describing the field of marine optics, which is illustrated in Figure 2.7. If we know the IOPs of the water column and boundary conditions, we can use radiative transfer modelling to calculate the oceanic AOPs, which furthermore can be used to model the reflected signal observed by satellites. By extension, concentrations and properties of the optically active constituents in the ocean (the "state of the ocean") can in principle be used to model the IOPs. All of these modelling efforts go under the term *forward modelling*, as the computations are generally well-defined in this direction. Modelling in the other direction, e.g. calculating IOPs from AOPs, is called *inverse modelling* and is considerably more challenging as the problem is often not well-posed, for instance can different sets of IOPs give the same AOPs (Werdell *et al.*, 2018).

2.4 Instrumentation platforms

Ocean color satellites systems have been a central instrumentation platform for optical oceanography observations since the late 1970s, providing passive multispectral ocean color images of the Earth (Chai *et al.*, 2020). By applying atmospheric corrections, the images are processed into estimates of the oceanic spectral water-leaving radiance (Blondeau-Patissier *et al.*, 2014). Further estimates can then be made on marine biogeochemical and optical properties of the ocean, either by utilizing empirical relationships or radiative transfer modelling. The latter is of particular interest because it builds directly on our physical understanding of processes driving light propagation in the ocean (absorption and scattering) and their connection to biogeochemical properties of interest, and may be easier generalized to larger geographical areas (Werdell *et al.*, 2018). Ocean color satellite observations have been highly successful in providing global and basin-scale estimates of for instance chl-a, showing seasonal and multidecadal trends. There are considerable research efforts directed towards improving ocean color products, in particular in coastal waters that are much more optically complex than the open ocean. In addition to the lack of vertical information, interference from cloud cover and low zenith-angles are inherent problems for ocean color observations, especially at high latitudes that are of increasing importance for global primary productivity (Chai *et al.*, 2020; Kulk *et al.*, 2020). Much of the Arctic Ocean and Antarctic coastal waters are also concealed from ocean color observations by sea-ice cover.

Shipborne *in situ* observations precedes ocean color observations with several decades (centuries including Secchi depth observations), and research vessels remain highly important observation platforms. While resource- and time-consuming, measurements done from vessels can give an unmatched level of detail and accuracy using an assortment of instrumentation and measurements techniques. Shipborne field campaigns are essentially required for assessing proxy relationships between biogeochemical and optical properties, and until recently this was the only platform for validating ocean color. From a vessel, water samples can be collected for laboratory analysis, and *in situ* measurements can be made using depth profiles or at discrete depths. On ships with the required capabilities, optical instrumentation can be mounted in flow-through mode for measuring surface waters during transit, or instruments can be installed on undulating vehicles towed behind the vessel (Boss *et al.*, 2018a; Slade *et al.*, 2010; Twar-

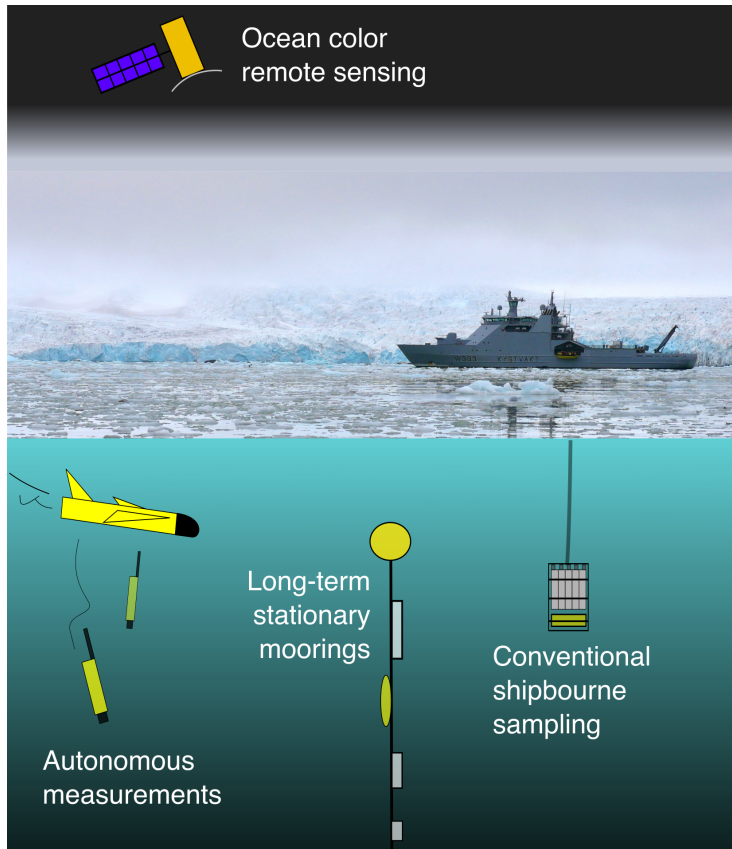


Figure 2.8: The platforms we use to observe the marine environment are under continuous development. For a long time, shipborne measurements (discrete sampling and later also profiling) were together with diving our only way of researching the ocean. Now, remote sensing and long-term mooring are also widely used, and in the past decades there has been a rapid development in autonomous platforms such as gliders and buoys.

dowski et al., 2007). In addition to being resource- and time-consuming, shipborne observations are constrained in spatial and temporal coverage, and can be limited by adverse weather conditions and sea-ice.

Fixed-location observation systems such as moorings are widely used in physical and biogeochemical oceanography, as these systems offer high temporal resolution with deployment times up to several years. However, optical measurements can be severely impacted by bio-fouling, which greatly impacts the results from long-term deployments in surface waters (*Twardowski et al., 2007*). Long-term deployments deeper than the euphotic depth are less affected by bio-fouling. While such fixed-depth measurements are obviously less useful for observing e.g. primary productivity, they can provide valuable observations for studying sediment processes or the biological carbon pump (*Boss et al., 2018b*).

Autonomous observation platforms such as Argo floats, gliders, and unmanned surface vehicles have been growing in use over the past decade (*Chai et al., 2020; Claustre et al., 2020*). Argo floats and gliders can change their buoyancy using inflatable bladders, and thereby ascend or descend through the water column while profiling, and transmit data via satellite communication on the surface. Argo floats drift passively with the ocean currents, while gliders may be equipped with wings that allow some horizontal steering. The biogeochemical Argo array is a collection of currently over 350 Argo floats with biogeochemical sensors distributed in the global ocean. Optical sensors for measuring downward irradiance, attenuation and backscattering are present on many of the biogeochemical Argo floats, which have a typical lifetime of ~ 4 years. Gliders have typically shorter deployment times and are remotely controlled, but can be equipped with a wider range of instrumentation. In the ice-covered Arctic Ocean, ice-tethered profilers with similar instrumentation as biogeochemical Argo floats have yielded invaluable data sets from an otherwise opaque and sparsely sampled region (*Boles et al., 2020*). While showing a tremendous potential in large scale monitoring, autonomous system observations are constrained by limited payload and battery capacity, and long deployment times are challenging for the stability of the measurements (*Chai et al., 2020; Twardowski et al., 2007*). To maximize the potential of the optical measurements it is important to compliment them with more detailed optical measurements from shipborne surveys.

Chapter 3

Instrument characteristics and methods



Figure 3.1: The LISST-VSF being deployed during the UAK 2020 cruise in Storfjorden, Svalbard.

When assessing the validity of environmental measurements like scattering or absorption properties of natural waters, there are many factors that need to be taken into account (Webster and Eren, 2018). Precision and accuracy are the two factors most commonly assessed, as they are intuitively understood from measuring a single value. *Precision* describes how well repeated measurements converge against a value, or the uncertainty inherent in a single measurement. Normally, precision is easily assessed by repeating measurements, but can vary with the signal strength or auxiliary factors (such as ambient light). Whether repeated measurements converge towards the correct value or not, is described by the *accuracy*. Systematic over- or under-estimations (bias) can have significant consequences for results or error propagation into models. For environmental measurements, accuracy can be considerably more challenging to determine than the precision, since the true" value is often not well-established. Even the most accurate measurements can have uncertainties, and there may be inherent differences between the measurements making comparisons difficult.

Linearity or *sensitivity* describes how accurate and precise a measurement is over a wider range of measurements. The dynamic range of the instrument describes the measurement domain where the linearity hold, outside the measurements may be saturated or the amount of noise is too high. Assessing the dynamic range is of particular importance for optical measurements, due to the considerable variability seen in op-

tical properties of natural waters. For instance, salinity varies linearly in the global ocean between approximately 30 and 40 PSU, while the scattering coefficient has been observed to vary logarithmically between 0.05 and 30 m^{-1} (Babin *et al.*, 2003).

Many studies have shown using high-resolution measurements that optical properties can vary considerably across a vertical profile, with gradients on a sub-meter scale (Claustre *et al.*, 2020; Frette *et al.*, 2004; Twardowski *et al.*, 1999; Whitmire *et al.*, 2009). In coastal surface waters, horizontal variations on the scale of 200 meters or less can be observed (Moses *et al.*, 2016). Consequently, under-sampling is likely a prominent feature in optical oceanography, especially of the vertical structure given the difficulty of extracting such information from passive remote sensing (Claustre *et al.*, 2020; Dierssen, 2010; Kulk *et al.*, 2020). Thus, a high sampling rate yielding a high spatial resolution is a key feature of an *in situ* instrument to get accurate observations of the entire water column.

Within the framework of environmental monitoring, optical measurements are typically reported in terms of proxy relationships. How do the measurements relate to environmental properties such as particle concentration or primary production? These relationships can be robustly quantified or more vaguely defined, depending on the ability to validate the relationships. For instance, robust empirical relationships have been found between chl-a concentration and particulate absorption in the open ocean ($r^2 = 0.91$) (Bricaud *et al.*, 1998), and particulate matter concentration and backscattering coefficient ($r^2 = 0.96$) (Boss *et al.*, 2009a). By contrast, fluorescence is of particular interest for *in situ* measurements of chlorophyll-a (chl-a) and dissolved organic matter (DOM), but the relationship between measured fluorescence and chl-a or DOM concentration can be affected by confounding factors and varies significantly by region (Roessler *et al.*, 2017). Nevertheless, the numerous advantages to fluorometric sensors (low-cost, small size, large range) still makes this measurement highly valuable for environmental monitoring.

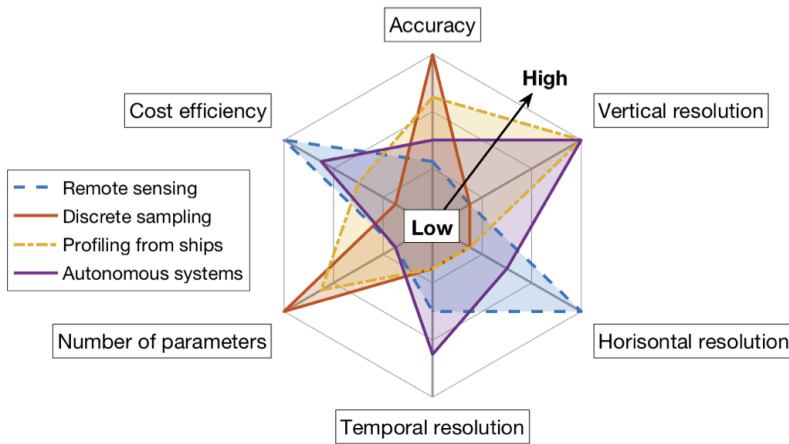


Figure 3.2: Illustration of the relative strengths and weaknesses of the different measurement strategies. Adapted from El Serafy et al. (2021)

Figure 3.2 illustrates the relative strengths and weaknesses of different measurement strategies using the instrument platforms described in section 2.4. Measurements with LISST-VSF, LISST-200X and ac-9/s lie within profiling from ships, which have a high vertical resolution and number of parameters, moderate cost-efficiency and accuracy, and low horizontal and temporal resolutions. No measurement strategy is perfect, but combining a set of different strategies can offer an accurate account of the underlying dynamics, "the state of the ocean". Combinations of two strategies, like ship-bourne profiles and discrete sampling, or remote sensing observations and autonomous gliders, can help assessing and hopefully improving weaknesses in both approaches.

3.1 Characteristics of LISST instruments

LISST instruments send a collimated laser beam through a water sample, and measure the scattered, transmitted and incident light. Modern diode lasers give precise and stable incident light at single wavelengths, and transmitted and incident light is measured similarly to common transmissometers using photodetectors and beam splitters. Measuring the scattered light requires a more complex optical setup, see Figure 3.3 and 3.4. Many LISST-instruments (e.g. LISST-100, LISST-200X, LISST-Deep) measures forward scattering using a ring detector, while the LISST-VSF uses a combination of the ring detector and a rotating eyeball detector.

3.1.1 Ring detector

The following treatment of how the VSF is measured by LISST ring detectors primarily follows Agrawal (2005) and Agrawal and Pottsmith (2000). The scattered light passes

through the optical window and a convex lens before striking the ring detector, which has been placed at the focal length f of the lens. The ring detector is an array of small photo-diode detectors shaped as partial rings (covering 60° instead of the full 360° ring), each with a very precise inner and outer radius. At the lens focal plane, the lens sends all light scattered at angle θ to the radial distance r from the lens axis, following the formula $r = f \tan \theta_a$. As the lens is in air, the scattering angles in water are transformed via Snells law, $\sin \theta = \sin \theta_a/n_w$. Consequently, each ring detector will collect light scattered between two angles corresponding to the inner and outer radius. At the centre of the ring detector, there exists a small hole for the transmitted light to pass through.

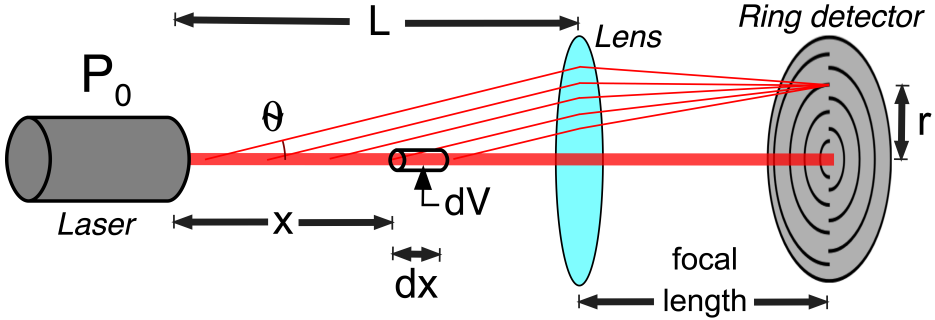


Figure 3.3: Schematic giving an overview of the LISST ring detector. The convex lens makes all light scattered at a certain angle hit the ring detector hit at the radius r , as the detector is placed at the focal length f of the lens. An optical window separating the sample volume and the lens is not drawn.

The silicon photodiodes convert light into electrical current. The detector output is digital counts which has a linear relationship with optical power P_i [W], and by dividing P_i by the detector area the irradiance is found. The ring radii increase logarithmically, meaning that the innermost rings cover a much smaller area than the outermost rings. This is advantageous if the scattering is very forward-peaked, as in natural waters, but can be problematic if the scattering is isotropic. From the measured optical power, we can compute the VSF. From the definition of the VSF, we have

$$dP_s(\theta) = \beta(\theta)E dV d\Omega. \quad (3.1)$$

Here, $dP_s(\theta)$ is the optical power scattered from the infinitesimal volume dV at the infinitesimal solid angle $d\Omega$, due to a beam of irradiance E and the VSF $\beta(\theta)$. To find the contribution from the entire beam, we want to evaluate this expression as an integral. We assume that the laser beam is radially uniform, but is attenuated as it passes through the sample volume. Hence, we have $dV = A dx$, where A is the beam cross-section and dx is a infinitesimal length of the beam (x is the distance between the start of the sample and dV), and $E(x) = \exp(-cx)P_0/A$, where P_0 is the power of the beam. The scattered light will also be attenuated as it travels between dV and the optical window, such that the power detected by the detector is

$$dP(\theta) = dP_s(\theta) \exp \left[-\frac{c(L-x)}{\cos \theta} \right]. \quad (3.2)$$

Here, L is the laser beam path length. The solid angle term can be written as $d\Omega = 2\pi\phi \sin\theta d\theta$ when we assume symmetry around the laser beam axis (azimuthal symmetry), with ϕ being the fraction of the azimuthal angles being covered by the ring detector ($60^\circ/360^\circ = 1/6$ for the ring detector). Inserting these expressions into Eq. 3.2 and 3.1 yields

$$dP(\theta) = \exp\left[-\frac{c(L-x)}{\cos\theta}\right]\beta(\theta)\exp(-cx)\frac{P_0}{A}A dx 2\pi\phi \sin\theta d\theta \quad (3.3)$$

$$= \exp\left[-c\left(\frac{L-x}{\cos\theta} - x\right)\right]\beta(\theta)P_0 dx 2\pi\phi \sin\theta d\theta. \quad (3.4)$$

We can now formulate analytical integrals for the power detected by each of the rings in the ring detector P_i , without having made any considerable assumptions. We want to integrate x across the path length from O to L , and the polar angle θ from the inner (θ_i) to outer (θ_{i+1}) scattering angle covered by the respective detector. We can compute θ_i and θ_{i+1} from the detector radii. The integral is then given as

$$P_i = 2\pi\phi P_0 \int_0^L \int_{\theta_i}^{\theta_{i+1}} \exp\left[-c\left(\frac{L-x}{\cos\theta} + x\right)\right]\beta(\theta) dx \sin\theta d\theta. \quad (3.5)$$

This integral is straight-forward to compute if $\beta(\theta)$ is known, however we want to compute $\beta(\theta)$ from P_i measurements. To do this, we assume that $\beta(\theta)$ varies slowly between θ_i and θ_{i+1} , and that the two angles are relatively close. Consequently, we can approximate $\beta(\theta)$ as an average value $\beta_i = \langle\beta(\theta)\rangle$ across the integral. Moreover, since the ring detector measures light scattered less than $\sim 15^\circ$, we can approximate $\cos\theta$ as unity, which greatly simplifies the integral,

$$P_i = 2\pi\phi P_0 \beta_i \exp(-cL) \int_0^L dx \int_{\theta_i}^{\theta_{i+1}} \sin\theta d\theta \quad (3.6)$$

$$= 2\pi\phi P_0 \beta_i e^{-cL} L (\cos\theta_i - \cos\theta_{i+1}). \quad (3.7)$$

Scattering and absorption of pure water itself also needs to be accounted for, as well as optical losses in the instrument. Similar to comparable optical instrumentation, these factors are corrected for by doing background measurements on ultra-pure water, e.g. milli-Q water. The measured attenuation and scattering due to pure water (and optical losses) are denoted c_w and $\beta_{i,w}$, while the particulate attenuation and scattering is denoted c_p and $\beta_{i,p}$. The c and β_i in Eq. 3.5 is the sum of the pure water and particulate attenuation and scattering. For the background measurements, we have the transmission measurements $P_{i,w} = P_0 e^{-c_w L}$ and the scattering measurements,

$$P_{i,w} = 2\pi\phi P_0 \beta_{i,w} e^{-c_w L} L (\cos\theta_i - \cos\theta_{i+1}). \quad (3.8)$$

Using our expressions for the background measurements, we can rewrite Eq. 3.5 as

$$P_i = 2\pi\phi P_0 (\beta_{i,p} + \beta_{i,w}) e^{-(c_p + c_w)L} L (\cos\theta_i - \cos\theta_{i+1}), \quad (3.9)$$

$$\frac{P_i}{e^{-c_p L}} = 2\pi\phi P_0 \beta_{i,p} e^{-c_w L} L (\cos\theta_i - \cos\theta_{i+1}) + P_{i,w}, \quad (3.10)$$

$$P_{i,p} = 2\pi\phi P_0 \beta_{i,p} e^{-c_w L} L (\cos\theta_i - \cos\theta_{i+1}) = \frac{P_i}{\tau} - P_{i,w}. \quad (3.11)$$

Here, τ is the optical transmission and is related to the transmission measurements by

$$\tau = e^{-c_p L} = \frac{e^{-(c_p+c_w)L}}{e^{-c_w L}} = \frac{P_t}{P_{t,w}} \quad (3.12)$$

The transmission measurements P_t and $P_{t,w}$ are scaled by the incident laser power to account for drifting in the laser. Finally, $P_{i,p}$ is the corrected scattering data, used in the LISST particle size distribution inversion algorithm (often referred to as *cscat*), and can readily be used to compute the VSF from Eq. 3.11,

$$\beta_{i,p} = \frac{P_{i,p}}{P_0} \frac{e^{c_w L}}{2\pi\phi L(\cos\theta_i - \cos\theta_{i+1})}. \quad (3.13)$$

As expected from the formal definition of the VSF, there exists a linear relationship between $\beta_{i,p}$ and the ratio $P_{i,p}/P_0$. The relationship for each ring can be determined both analytically from Eq. 3.11, if all the parameters including photodiode sensitivities are known, or empirically by measuring solutions with known scattering properties, typically monodisperse plastic beads with diameters on the microscale (*Slade and Boss, 2006*).

3.1.2 Eyeball detector

The LISST-VSF eyeball detector rotates around its own axis to view different parts of the laser beam, allowing measurements of scattered light covering the scattering angles 15-150°. While it does not involve a large photodiode array as the ring detector, there are two features that makes the eyeball scattering measurements complex to process.

Firstly, the incident light is polarized, and the scattered light passes through a polarizing beam splitter before detection. This enables measurements of linear polarization of the scattered light. Using a half-wave plate, the incident light polarization can be changed from perpendicular to parallel (or vertical to horizontal). This means that at every measured angle, four scattering measurements have been made; perpendicular polarized incident light and parallel polarized scattered light (rp), perpendicular polarized incident light and perpendicular polarized scattered light (rr), parallel polarized incident light and parallel polarized scattered light (pp), and parallel polarized incident light and perpendicular polarized scattered light (pr). This enables the LISST-VSF to also measure the polarizing properties of natural waters, which has been even less measured than the VSF.

Secondly, the eyeball detector uses photomultiplier tubes with different gain levels (that are automatically adjusted) to magnify the detected signal, and the laser is dimmed between 15° and ~45°. This is to account for the large dynamical range in $\beta(\theta)$ both across the angular domain and between different types of waters. Moreover, the geometry of the detector is more complex than the ring detector. Consequently, it is more difficult to make an absolute calibration of the eyeball detector, and several studies have been published using different approaches (*Hu et al., 2019; Koestner et al., 2018, 2020*). The following treatment primarily follows *Hu et al. (2019)*.

The scattered light detected by the eyeball detector $I_{ij}^*(\theta, V)$ (still in digital counts) is first corrected for ambient light,

$$I_{ij}^*(\theta, V) = I_{ij}^{\text{on}}(\theta, V) - I_{ij}^{\text{off}}(\theta, V), \quad (3.14)$$

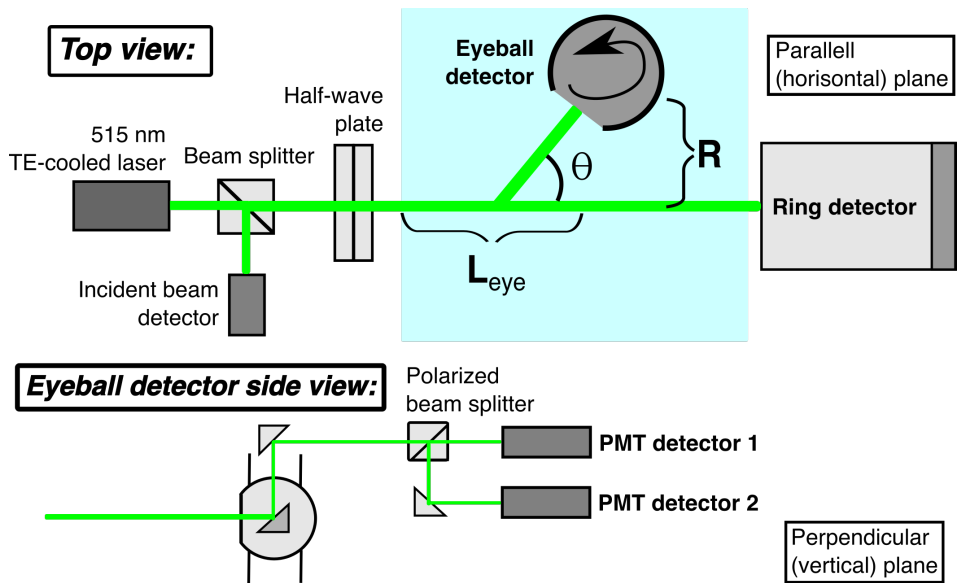


Figure 3.4: Schematic overview of the LISST-VSF design. The ring detector works as described in Fig. 3.3 and subsequent calculations. In addition, a rotating eyeball detector measures scattering at larger angles. The incident light is emitted with two different linear polarizations, changed by inserting a half-wave plate after one rotation. One polarization is oriented in the parallel (horizontal) plane, and the scattered light is detected using two detectors covering each of the linear polarizations (designated pp and pr). The other polarization is in the perpendicular (vertical) plane, yielding corresponding scattering measurements rp and rr .

where ij refers to different polarization combinations (rp, rr, etc.). As the eyeball is moving, the laser turns on and off rapidly. In Eq. 3.14, $I_{ij}^{\text{on}}(\theta, V)$ refers to measurements when the laser is turned on, and $I_{ij}^{\text{off}}(\theta, V)$ when the laser is turned off. The supply voltage of the PMT gain is V . Furthermore, the scattering signal is corrected for geometric effects and attenuation, and the background measurements are subtracted,

$$I_{ij}(\theta, V) = (I_{ij}^*(\theta, V) - I_{ij,w}^*(\theta, V))T_{ij}f(\theta) \sin \theta e^{c_p l(\theta)}. \quad (3.15)$$

Here, T_{ij} corrects for the transmission of the half-wave plate (set to unity for I_{pr} and I_{pp} , for I_{rp} and I_{rr} an instrument-specific value is applied), $f(\theta)$ corrects the laser-dimming at smaller angles and $\sin(\theta)$ accounts for the (relative) change in volume of water the eyeball detector measures. The particulate attenuation c_p is computed similarly as for the ring detector (Eq. 3.12), but the path length $l(\theta)$ is calculated using

$$l(\theta) = L_{\text{eye}} - R \cot \theta + \frac{R}{\sin \theta}.$$

See Fig. 3.4 for explanations of R and L_{eye} .

We now know the four measured polarization components, but they are still not converted from digital counts, and how do they relate to the VSF and polarization properties? Some Mueller calculus is required to relate the measurements to the scattering properties. The incident light can be described by the Stokes vector

$$\mathbf{s} = I_0 \begin{bmatrix} 1 \\ \pm 1 \\ 0 \\ 0 \end{bmatrix}, \quad (3.16)$$

where the I_0 is the incident light intensity, and ± 1 corresponds to full linear polarization, either perpendicular or parallel. The light scattering in the water sample is described by

$$\mathbf{P} = \begin{bmatrix} P_{11}(\theta) & P_{12}(\theta) & 0 & 0 \\ P_{21}(\theta) & P_{22}(\theta) & 0 & 0 \\ 0 & 0 & P_{33}(\theta) & P_{34}(\theta) \\ 0 & 0 & P_{43}(\theta) & P_{44}(\theta) \end{bmatrix}. \quad (3.17)$$

Here, P_{11} is the VSF, and components $P_{12} = P_{21}$ and P_{22} describe the linear polarization properties of the water constituents. The remaining Mueller components cannot be measured by the LISST-VSF. The optical components the scattered light passes through are described by the Mueller matrices,

$$\mathbf{R} = \begin{bmatrix} 1 & 0 & 0 & 0 \\ 0 & \cos(2\theta) & \sin(2\theta) & 0 \\ 0 & -\sin(2\theta) & \cos(2\theta) & 0 \\ 0 & 0 & 0 & 1 \end{bmatrix}, \quad (3.18)$$

and,

$$\mathbf{L} = \frac{1}{2} \begin{bmatrix} 1 & \pm 1 & 0 & 0 \\ \pm 1 & 1 & 0 & 0 \\ 0 & 0 & 0 & 0 \\ 0 & 0 & 0 & 0 \end{bmatrix}, \quad (3.19)$$

where ± 1 distinguishes between the perpendicular and parallel polarization of the scattered light, which is measured with two different detectors. There is also a relative gain difference α between the two detectors. The detected light \mathbf{d} is subsequently given by,

$$\kappa(\theta, V)\mathbf{d} = \mathbf{LRPs}. \quad (3.20)$$

The coefficient $\kappa(\theta, V)$ is defined to account for all optical losses, instrument geometry, and the quantum efficiency of the detectors (conversion of digital counts to optical power). In *Hu et al.* (2019) and Paper I, $\kappa(\theta, V)$ is set to be the same for all polarization components (as only the VSF is absolutely calibrated), while *Koestner et al.* (2020) calculated different scaling factors for I_{pr} , I_{pp} , I_{rp} , and I_{rr} , which enables calibrated P_{12} and P_{22} measurements. As the polarization properties are outside the scope of this thesis, we assume a single scaling function $\kappa(\theta, V)$.

By conducting the matrix algebra in Eq. 3.20, we get the following set of equations:

$$\kappa(\theta, V)I_{pp}(\theta, V) = I_0[P_{11}(\theta) + P_{12}(\theta) + (P_{12}(\theta) + P_{22}(\theta)) \cos 2\theta] \quad (3.21)$$

$$\kappa(\theta, V)I_{pr}(\theta, V) = \alpha I_0[P_{11}(\theta) + P_{12}(\theta) - (P_{12}(\theta) + P_{22}(\theta)) \cos 2\theta] \quad (3.22)$$

$$\kappa(\theta, V)I_{rp}(\theta, V) = I_0[P_{11}(\theta) - P_{12}(\theta) + (P_{12}(\theta) - P_{22}(\theta)) \cos 2\theta] \quad (3.23)$$

$$\kappa(\theta, V)I_{rr}(\theta, V) = \alpha I_0[P_{11}(\theta) - P_{12}(\theta) - (P_{12}(\theta) - P_{22}(\theta)) \cos 2\theta] \quad (3.24)$$

By solving Eq. 3.21-3.24, we get the equation for the VSF,

$$\beta(\theta) = P_{11}(\theta) = \kappa(\theta, V) \frac{I_{pp}(\theta, V) + I_{pr}(\theta, V)/\alpha + I_{rp}(\theta, V) + I_{rr}(\theta, V)/\alpha}{4I_0} \quad (3.25)$$

$$= \kappa(\theta, V)P_{11}^{\text{uncal}}(\theta). \quad (3.26)$$

For finding α , it is utilized that $\cos(2 \times 45^\circ) = \cos(2 \times 135^\circ) = 0$. From Eq. 3.21-3.24 we then find

$$\alpha = \frac{I_{rr}(45^\circ, V)}{I_{rp}(45^\circ, V)} = \frac{I_{rr}(135^\circ, V)}{I_{rp}(135^\circ, V)} = \frac{I_{pr}(45^\circ, V)}{I_{pp}(45^\circ, V)} = \frac{I_{pr}(135^\circ, V)}{I_{pp}(135^\circ, V)}. \quad (3.27)$$

Since the measurements can contain noise, α is computed from the median of the above fractions.

There are several ways to calibrate the uncalibrated eyeball VSF measurement $P_{11}^{\text{uncal}}(\theta)$. The factory-default calibration method is a relative calibration, where the two outermost ring detectors are linearly extrapolated to the first eyeball detector value at 15° . The ratio between the extrapolated value and the uncalibrated measurement $P_{11}^{\text{uncal}}(15^\circ)$ is then used as a scaling factor to correct the entire $P_{11}^{\text{uncal}}(\theta)$ measurements. The major drawback of using this calibration method is that any measurement errors can easily propagate to the entire eyeball VSF measurement. Nevertheless, the relative calibration still works reasonably well in moderate (coastal) waters. It also has the benefit of not requiring resource-demanding laboratory measurements, and is not sensitive to laser drifting. The absolute calibrations done in *Hu et al.* (2019) and Paper I utilizes microscopic bead measurements to find $\kappa(\theta, V)$, as $\beta(\theta)$ is accurately known for polymer beads. Since the phase functions of polymer beads do not resemble the phase functions of natural waters, different monodisperse solutions with varying bead sizes and concentrations have to be used to cover the dynamical range for all angles.

There are 10 different PMT gain values, depending on supply voltage V , which implies that the $\kappa(\theta, V)$ must be found for each of the voltage steps. However, the PMT gain G_1 at supply voltage V_1 is related to the corresponding PMT gain G_2 at V_2 by the equation

$$\frac{G_2}{G_1} = \left(\frac{V_2}{V_1}\right)^\gamma, \quad (3.28)$$

where the coefficient $\gamma = 8.6$ depends on the dynode material and geometry. This allows Eq. 3.26 to be rewritten as

$$\beta(\theta) = \left(\frac{V_0}{V}\right)^\gamma \kappa(\theta, V_0) P_{11}^{\text{uncal}}(\theta). \quad (3.29)$$

Hence, we only need to find $\kappa(\theta, V_0)$ at a reference voltage V_0 . In Paper I and the default relative calibration, the incident light I_0 is included in the $\kappa(\theta, V_0)$ -value, while in *Hu et al. (2019)* I_0 is included when computing $P_{11}^{\text{uncal}}(\theta)$. The first approach may then require a scaling factor ($I_0^{\text{meas}}/I_0^{\text{cal}}$) in future results if the laser power drifts.

The design of LISST-instruments demands complex data processing to acquire the measured VSF, which makes it more difficult to assess the precision and measurement uncertainties. In the case of the LISST-VSF, we see from bench-top and field measurements that the VSF precision depends on signal strength, PMT gain, and ambient light. However, rigorously quantifying the precision under different conditions remains to be done. *Koestner et al. (2020)* showed that polarization properties also need absolute calibration for accurate measurements, in particular the P_{22} component. *In situ* polarization measurements from the LISST-VSF remains to be published, along with a corresponding error analysis.

3.2 Monte Carlo simulations of optical instrumentation

In order to compute IOPs from optical instruments, it is necessary to make some assumptions about the light transport within the instrument sample volume, for instance about multiple scattering. It is advantageous to use Monte Carlo simulations to simulate radiative transfer within optical instruments because it is relatively straightforward to implement geometrical boundary conditions, especially compared to traditionally RTE approaches. However, Monte Carlo methods require a statistical interpretation of the scattering and absorption coefficients. Consider the Beer-Lambert law of a beam passing through a homogeneous sample volume

$$I(x) = I_0 e^{-cx} = I_0 e^{-\tau}, \quad (3.30)$$

where I_0 is the intensity of the incident beam, $c = b + a$ is the attenuation coefficient, and $I(x)$ is the remaining intensity of the beam that has not been scattered or attenuated. Optical depth is a useful dimension-less quantity. The beam intensity can be defined in several ways, but the number of photons (per second) is practical to use for Monte Carlo simulations. Following this model, Eq. 3.30 tells us that the *probability density* that a photon is scattered or absorbed at the optical depth τ is

$$P = \frac{d}{d\tau} \left(1 - \frac{I}{I_0}\right) = -\frac{d}{d\tau} e^{-\tau} = e^{-\tau}. \quad (3.31)$$

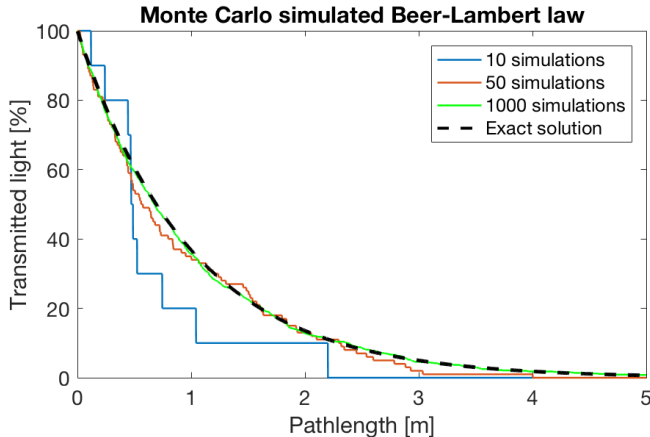


Figure 3.5: With Monte Carlo simulations, deterministic laws are formulated as probability distributions. Here, the Beer-Lambert law is simulated with different numbers of incident photons. Few simulated photons yield noisy and random results, while a large number of photons makes the simulation converge against the analytical solution.

This expression can be rearranged to $\tau = -\ln P$. In this context, P can be any arbitrary number ξ between 0 and 1. Algorithms for generating a random ξ between 0 and 1 are prevalent. Then follows the key part of the Monte Carlo methodology. By drawing a random ξ , we simulate when a single photon is attenuated after travelling the distance $x = \tau/c = -\ln \xi/c$. If we draw a large number of random ξ -values, and treat the simulated photon attenuation lengths as observations, we will end up with a statistical distribution of the "observations" which recreates the Beer-Lambert law in Eq. 3.31. This is demonstrated in Figure 3.5.

If we then continue to simulate a single photon, it is either absorbed or scattered. This can be calculated using a statistical approach, where the probability that an attenuated photon is scattered is given by the single-scattering albedo $\omega = b/c$.

If the photon is scattered, it is given a new direction by formulating the phase function (Eq. 2.3) as a probability function, and drawing another random number. After a new direction is found, the process is repeated (find new travelled distance, if it is scattered, new direction) for the same photon until it is eliminated. Elimination happens when the photon is absorbed, or if it passes a boundary condition such as an absorbing wall or a detector. The result is saved, and a new photon simulation is restarted after elimination. The uncertainty decreases with the number of (detected) photons, e.g. for transmission simulations the uncertainty decreases relatively quickly, while for backscattering it may take a large number of simulations. More than a million photons are typically simulated. This means Monte Carlo simulations can be very time-consuming, especially if the photons are scattered many times before elimination.

When treating the detected photons $n_i(\theta_i)$, for example at the detector corresponding to the scattering angle θ_d , we sum up all the photons hitting the detector within a certain angular interval $\theta_{d,\min}-\theta_{d,\max}$. However, in certain instances very few photons will actually hit the detector due to the IOPs. For instance, if the absorption is very high, few photons will survive each attenuation event, and fewer will reach the detec-

tor. A common way of solving this issue is to introduce a statistical weight w_i to each of photon. In the high-absorption example, instead of eliminating photons when they are absorbed, we alter the statistical weight according to the single-scattering albedo at each attenuation event j ,

$$w_{i,j+1} = w_{i,j} \frac{b}{c}, \quad (3.32)$$

which means all photons will be simulated until they leave the sample volume or are detected. When treating the detected photons in the end, we sum the w_i -values of all photons hitting the detector to find the number of detected photons N_d , instead of the actual sum of the photons. The method of weighting the photons can be expanded to account for photons which simply pass through the sample volume without being attenuated, or to mitigate the fact that most photons are not scattered in the direction of the detector (*Buras and Mayer, 2011*), and can make Monte Carlo simulations orders of magnitude more efficient. For the LISST-VSF, the detected scattering is calculated using instrument-specific angular bins, and the VSF is computed using a version of Eq. 3.13, with the ratio P_i/P_0 being replaced by the fraction of detected photons N_d to the number of total incident photons N_0 .

The photon is a physical concept borrowed from quantum electrodynamics, and is actually somewhat misleading to use for radiative transfer, as light propagates (and in particular when light scatters) fully as a wave phenomenon (*Mishchenko, 2009*). A photon in this context is a mathematical model which describes a (small) quantity of radiation energy, more similar to ray tracing than quantum electrodynamics. Curiously enough, the way Monte Carlo methodology is implemented in marine and atmospheric optics bears a strong resemblance to the problem Monte Carlo was originally designed for, namely neutron transport within nuclear weapons (*Eckhardt et al., 1987*). Dealing with photons instead of neutrons leads fortunately to less destructive outcomes.

3.3 LISST error sources

In this section, a systematic overview of known LISST error sources for scattering measurements is presented. For completeness, some results from Paper I and III are included. It should be noted that errors connected to computing the particle size distributions, e.g. out-of-bounds particles and particle composition, are not considered here.

Detector limits

The photodiodes used in the LISST detectors give digital counts as output. At low light levels, the detected signal is dominated by noise (e.g. dark current) and is thus comparable in magnitude to the background measurement. Consequently, when we subtract the background in Eq. 3.11, there is nothing left of the signal. This is apparent from bead measurements over a large range of concentrations as the scattering measurements become erratic below a certain value, see Figure 3 in Paper I. This has previously been studied by *Andrews et al. (2011a)*, who estimated minimum concentration and scattering limits for the LISST-100X. LISST-200X cannot be used for measuring the VSF and attenuation in clear waters as the laser power is too low and the path length is too

short. For the LISST-VSF, the detector noise limit has been investigated for the ring detector, the eyeball detector is more convoluted to assess due to the complex data processing and the concurrent effects of ambient light. Nevertheless, bead measurements show that the ring detector is more limited in dynamical range than the eyeball detector, which has also been seen in other studies (Zhang *et al.*, 2020).

In the extreme upper limit, both the ring detector and eyeball detector has been observed to become saturated, but at this point the measurements are typically also severely impacted by multiple scattering.

Schlieren effects

Microscale vertical gradients in salinity or temperature yield rapid changes in the refractive index of the water, which can bend light passing through the water, such as an incident laser beam. LISST-instruments passing through such gradients is often strongly affected by such Schlieren effects, which manifest as enhanced forward scattering similar to large particles and lower transmission. Several studies have investigated or documented this error source in controlled laboratory environments (Styles, 2006) or in field deployments (Karageorgis *et al.*, 2015; Mikkelsen *et al.*, 2008; Miles *et al.*, 2021). Schlieren can affect the entire VSF in addition to the forward scattering, since transmission values are used to correct scattering measurements in the data processing through Eq. 3.11 and 3.15. Due to the chaotic nature of Schlieren, and because it resembles the scattering of large particles that can accumulate in the pycnocline, it is difficult to assess and correct. It is however a spatially limited effect.

Multiple scattering

Multiple scattering is a key process in radiative transport in the ocean and for surface reflectance (Chami *et al.*, 2006b), but is considered nearly negligible for IOP instruments due to the short path lengths, but there are some discrepancies in the literature on when multiple scattering can be neglected or not. While Jonasz and Fournier (2011) gives $\tau(1 - g) \ll 1$ as a general condition for single-scattering, the work by van de Hulst (1981) states that $0.1 < \tau < 0.3$ is the transition zone between the single-scattering and multiple-scattering regime, which is more restrictive than $\tau(1 - g) \ll 1$. Piskozub *et al.* (2004) found that multiple scattering has a negligible effect on attenuation measurements in natural waters. In the LISST-VSF study by Koestner *et al.* (2018), $\tau = 0.3$ was used as the maximum value for bead measurements, while in Hu *et al.* (2019), $c = 5 \text{ m}^{-1}$ was used as the upper limit, which corresponds to $\tau = 0.75$.

LISST-VSF measurements in turbid glacial meltwaters showed strong discontinuities at the transition between the ring and eyeball detector when the absolute calibration was applied to the eyeball detector data. There is a 30% difference in path length between the two detectors at the transition point. This motivated a deeper enquiry into how multiple scattering affects LISST-VSF measurements. When processing ring and eyeball detector data from the LISST-200X and LISST-VSF, we assume that light scattered more than once is lost. We correct for attenuated light along the path of the detected light with τ in Eq. 3.11 and e^{-cpl} in Eq. 3.15. However, light scattered more than once can often pass into the LISST optical windows and be detected together with the single-scattered light. Consequently, multiple scattering may cause greatly exag-

gerated VSF measurements. Due to the large angular dependence of the LISST-VSF path length, the phase function can also become distorted due to multiple scattering. This error was observed in measurements in Paper I, and has been investigated in detail using Monte Carlo simulations in Paper II and Paper III. Because LISST-200X has a much shorter 2.5 cm path length, it is considerably less affected than the LISST-VSF.

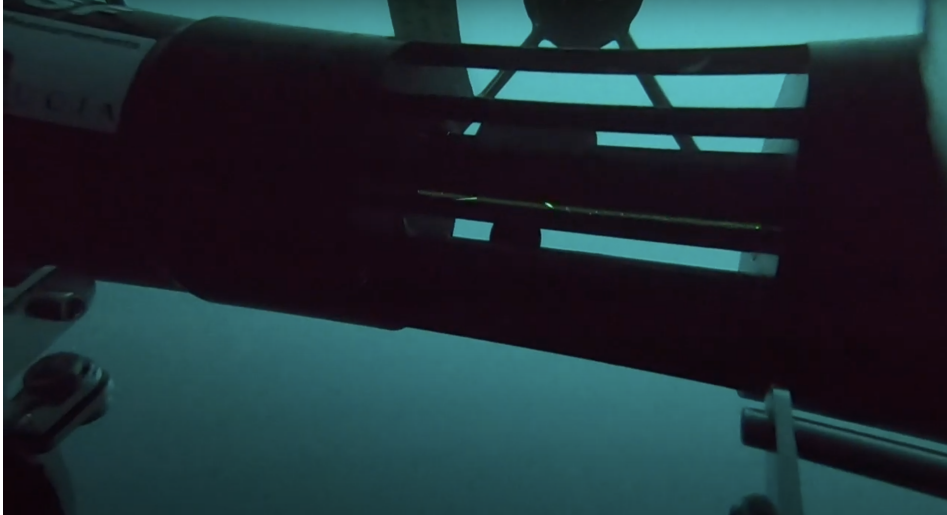


Figure 3.6: LISST instruments are open to the environment and thereby exposed to possible ambient light artifacts. Here, the LISST-VSF is photographed (from below) measuring underwater. Both scattered light from the laser and ambient light is visible.

Ambient light

Ambient light can easily contaminate optical measurements. One solution is to pump water into an opaque measurement set-up, but the pumping can disrupt particle flocs and other weak structures in the water mass. LISST instruments are designed to be deployed open to the environment, but this means they be susceptible to ambient light. *Andrews et al.* (2011b) investigated ambient light effect on the LISST-100X instrument, and found that outermost rings can yield artificially high scattering data. This gives erroneously high VSF measurements at the largest measured angles, and yields overestimates of the smallest particles in the particle size distribution. With the LISST-200X, an ambient light rejection method has been implemented (*Sequoia Scientific Inc.*, 2020).

The LISST-VSF measurements are open to the environment, meaning that the eye-ball detector also detects the ambient light field, particularly between $\sim 40^\circ$ and 120° . The ambient light is rejected by rapidly turning the laser on and off, and detecting the signal both when the laser is on and the laser is off, and then subtracting the signal due to ambient light, see Eq. 3.14. However, when the detected scattered light is weak compared to the ambient light and level of noise, ambient light can degrade the measurement quality. Considerable loss of precision has been observed in VSF measurements. The amount of noise makes it difficult to establish if this leads to sys-

tematic inaccuracies, and a more detailed study is required. Polarized components may be more impacted than the VSF due to their more intricate processing from the measured components, see Eq. 3.21-3.24. Furthermore, the detected ambient light field can be partially polarized. Assessing this error is further complicated by the different PMT gains of the measurements, which introduces varying levels of random noise. The effect of ambient light on the LISST-VSF ring detector measurements also remains to be investigated.

Statistical effects of the sample volume

We observe from the fundamental mathematical definitions of scattering and absorption, for instance Eq. 3.1, that the continuum assumption is expected to hold for IOPs, namely that the properties are continuous functions valid down to an indefinitely small volume. Optical properties of natural water are however decided by both dissolved matter and particles. Submerged particles can very much be discrete objects while still contributing to optical properties of the water mass. Notably, large particles can have a significant impact on light propagation in water even if there are not many of them in a small volume. In a recent study by *Davies et al. (2021)*, it was shown that a limited sample volume leads to instruments not detecting the contribution of large particle to absorption or scattering. The ac-s absorption tube has a sample volume of ~ 4 mL, given typical size distributions the authors demonstrated that for particles larger than $100 \mu\text{m}$, there is often less than one particle in the sample volume. By contrast, the LISST-VSF eyeball detects scattered light from a considerably smaller sample volume. It is uncertain what effect this has on LISST-VSF measurement accuracy and precision, and consequently on the measured VSF, P_{12} and P_{22} . LISST-200X measurements may also contain related uncertainties in the extreme forward direction.

Temperature and salinity corrections

Blank measurements are done using fresh ultra-pure water at room temperature. However, scattering and absorption properties of seawater (excluding particles and dissolved matter) depends on both temperature and salinity. Consequently, there can be an offset between the pure water scattering recorded during the background measurement and pure water component of the scattering measured *in situ*. The first study pointing out this issue for LISST-VSF measurements, *Hu et al. (2019)*, suggest computing the VSF of pure seawater and directly subtract it from the raw measurements without the use of a blank measurement. Another correction method for the VSF is described in Paper I, which utilizes both blank measurements and CTD measurements. For LISST-200X, the detectable scattering is magnitudes larger than the contribution from pure seawater and is thus negligible. The effect of temperature and salinity on the polarized components measured with LISST-VSF has not been investigated, and the corrections described above has not been validated experimentally.

Drifting and calibration quality

Like many other optical instruments, the LISST-instruments may be subject for laser or detector drift. Laser drift is typically corrected for in the data processing, and by doing a background measurement with ultra-pure water. However, when using the method

for absolute calibration in Paper I, the laser drift is actually not fully accounted for and needs to be included by using a scaling. This remains to be implemented, but it is not well-established how much the LISST-VSF laser actually drifts with time and use. Drifting of detector sensitivity has not been reported, but requires polymer bead measurements conducted across a long time period. The absolute calibration using polymer beads also involves uncertainties, in particular that we need to assume that we need to know the diameter and refractive index of the beads accurately. Another calibration challenge is the quality of ultra-pure water for blank measurements. Such water is not always readily available when doing fieldwork, and it can degrade over time, and thus the quality of a field calibration is not always easy to assess.

3.4 How scattering affects absorption measurements



Figure 3.7: When measuring absorption with ac-9/s instruments, a reflective tube is used to collect almost all of the scattered light. It is however impossible to collect all of the scattered light with this approach, causing measurement errors.

As of today, the only way of getting high-resolution depth profiles of spectral absorption and attenuation with high accuracy is by using the ac-9 or ac-s (ac-9/s) instruments. This type of instruments was developed in the early 1990s (Moore *et al.*, 1992), and soon after it became apparent that scattering errors are the most significant error source for these measurements (Kirk, 1992; Zaneveld *et al.*, 1994). For the attenuation detector, there is a finite acceptance angle for the light of 0.93° . This means that light scattered *less* than 0.93° will be detected as transmitted light, even though it has actually been attenuated. For absorption measurements, the scattering error is more complex and has more practical consequences. While the attenuation measurements use a tube which absorbs scattered light, the absorption measurements are based on using a reflective tube that is designed to reflect scattered light such that the majority of the non-absorbed light reaches the detector, especially since the VSF of natural waters is highly forward-peaked. Nevertheless, the reflective tube design is not a perfect collector of scattered light. The total internal reflectance, created by a quartz tube surrounded by an air gap, breaks down above a critical angle of 41.7° , meaning that

much of the light being scattered above this angle is lost. Furthermore, the reflectance efficiency of the tube is not 100% below 41.7°, leading to additional losses. Several approaches for correcting the scattering error of the measured absorption without auxiliary measurements were outlined in *Zaneveld et al.* (1994). All corrections schemes can be written on the form

$$a_{\text{corr}}(\lambda) = a_{\text{meas}}(\lambda) - \varepsilon_a(\lambda), \quad (3.33)$$

where a_{meas} and $a_{\text{corr}}(\lambda)$ are the measured and corrected absorption, and $\varepsilon_a(\lambda)$ is the estimated scattering error. Following methods were described for estimating the scattering error:

1. Assume that the non-water absorption in the near-infrared is negligible, and that the scattering error is independent of wavelength,

$$\varepsilon_a = a_{\text{meas}}(\lambda_{\text{ref}}). \quad (3.34)$$

This is called the *flat* or *baseline* method. Here, λ_{ref} is a measured wavelength in the infrared, typically 715 nm as this is a wavelength measured by the ac-9.

2. Assume that the scattering error is a certain fraction of the scattering coefficient,

$$\varepsilon_a = F b_{\text{meas}}(\lambda) = F [c_{\text{meas}}(\lambda) - a_{\text{meas}}(\lambda)], \quad (3.35)$$

where F is a fraction, typically around ~ 0.14 - 0.2 (*Watanabe et al.*, 2018), which have to be chosen based on whether organic or inorganic material dominates the water column. No assumptions are made about the near-infrared absorption, but we assume the phase function is constant after choosing a F -value.

3. The *proportional* method is a combination of the first two methods. We assume that the non-water absorption coefficient is zero in near-infrared, but that it varies spectrally with the scattering coefficient. Thus, we get a scattering error on the form,

$$\varepsilon_a = a_{\text{meas}}(\lambda_{\text{ref}}) \frac{b_{\text{meas}}(\lambda)}{b_{\text{meas}}(\lambda_{\text{ref}})} = a_{\text{meas}}(\lambda_{\text{ref}}) \frac{c_{\text{meas}}(\lambda) - a_{\text{meas}}(\lambda)}{c_{\text{meas}}(\lambda_{\text{ref}}) - a_{\text{meas}}(\lambda_{\text{ref}})}. \quad (3.36)$$

The flat and proportional methods became the most widespread scattering correction methods, given that they only use ac-9/s measurements for corrections. On the other hand, the assumptions these methods are built on have been continuously challenged in the decades after the instruments were first deployed (*Leymarie et al.*, 2010; *Stockley et al.*, 2017).

It is well-established that the near-infrared absorption is often not negligible, especially in coastal or estuarine waters (*Tassan and Ferrari*, 2003). Non-water absorption at long wavelengths can be measured using accurate laboratory instrumentation, for instance the PSICAM. *Röttgers et al.* (2013) conducted a study with comparisons of PSICAM and ac-9 measurements of the same water samples. An empirical relationship ($r^2 = 0.930$) was found between the measured PSICAM absorption a_{nw} (assumed to be "true") and the ac-9 absorption a_{meas} at 715 nm in coastal waters in the North Sea,

$$a_{\text{nw}}(715 \text{ nm}) = 0.212 \times [a_{\text{meas}}(715 \text{ nm})]^{1.135}. \quad (3.37)$$

This relationship made way for improvements of the flat and proportional correction methods in coastal waters. These improved versions are referred to in the literature as "semi-empirical" or "RR" methods. In the updated proportional method (Lefering *et al.*, 2018), a correction for the attenuation error is also included,

$$\varepsilon_a = [a_{\text{meas}}(715 \text{ nm}) - a_{\text{nw}}(715 \text{ nm})] \frac{c_{\text{meas}}(\lambda)/e_c - a_{\text{meas}}(\lambda)}{c_{\text{meas}}(715 \text{ nm})/e_c - a_{\text{nw}}(715 \text{ nm})}, \quad (3.38)$$

where $a_{\text{nw}}(715 \text{ nm})$ is estimated from Eq. 3.37, and e_c is the estimated fraction of the "true" attenuation which is not detected by the ac-9/s due to the acceptance angle. This value was found to be 0.56 in the North Sea in Röttgers *et al.* (2013). The attenuation error is covered in detail in Boss *et al.* (2009b), where ac-9/s was compared with LISST-instruments that had more than an order of magnitude smaller acceptance angle than the ac-9/s. The e_c -value was found to vary between 0.4 and 1.03.

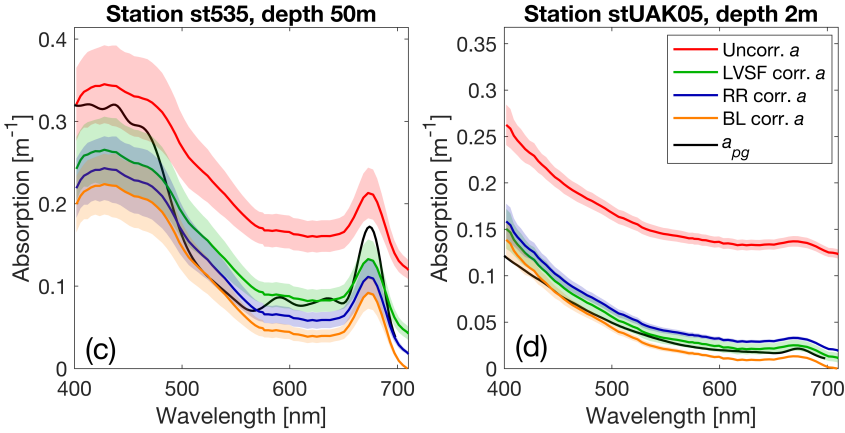


Figure 3.8: Scattering errors can have a serious impact on ac-9/s absorption measurements. Here are results from the UAK 2020 cruise in Storfjorden where accurate absorption spectra from two water samples are compared with uncorrected ac-s absorption measurements along with scattering-corrected spectra using three different methods, the baseline method (BL), semi-empirical (RR) and VSF correction using LISST-VSF measurements. The scattering error clearly has a strong but highly variable contribution to the uncorrected absorption measurements. See Paper IV for a more detailed description and analysis of the results.

Whether the phase function is independent of the wavelength or not was first assessed in relation to the ac-9 scattering error by McKee and Cunningham (2005) using *in situ* data, see Sect. 2.3.1. The approach made in this study was refined in later works using Monte Carlo simulations, and in the latest iteration, McKee *et al.* (2013), an imperfect reflectance efficiency of the reflective tube is also included. Consequently, the scattering error can be assessed without any initial assumptions about the IOPs. The absorption and attenuation coefficients measured by the ac-9/s are given by

$$a_{\text{meas}}(\lambda) = a_{\text{nw}}(\lambda) + f_a(\lambda)b_{\text{nw}}(\lambda), \quad c_{\text{meas}}(\lambda) = c_{\text{nw}}(\lambda) - f_c(\lambda)b_{\text{nw}}(\lambda). \quad (3.39)$$

The true non-water absorption, scattering, and attenuation coefficients are given by a_{nw} , b_{nw} , and c_{nw} , and are related by $a_{\text{nw}} + b_{\text{nw}} = c_{\text{nw}}$. Meanwhile, f_a and f_c are the fractions

of the scattering coefficient which contributes to respectively the scattering errors of the absorption and attenuation measurements. Given that we know the VSF at all angles, the f_c -value is determined from the integral,

$$f_c(\lambda) = 2\pi \int_{0^\circ}^{0.93^\circ} p(\theta, \lambda) \sin \theta d\theta, \quad (3.40)$$

where $p(\theta, \lambda)$ is the phase function calculated from Eq. 2.3. Determining the f_a -value requires knowledge about the reflectance efficiency r_w of the absorption tube. Monte Carlo simulations in *McKee et al. (2013)* yielded weighting functions $W_a(\theta)$, which tell us the relative contribution of VSF (or phase function) at the scattering angle θ for a given reflectance efficiency r_w between 0.95 and 1. The r_w -value can vary and needs to be known *a priori* or by fitting the parameter to minimize the error against known absorption values. *Stockley et al. (2017)* found that 0.98 is a typical value. The f_a -value can then be computed from

$$f_a(\lambda) = 2\pi \int_{0^\circ}^{180^\circ} W_a(\theta) p(\theta, \lambda) \sin \theta d\theta. \quad (3.41)$$

Following this equation, Eq. 3.33 and 3.39, we see that the scattering error for the absorption can in fact be calculated directly using the VSF,

$$\varepsilon_a(\lambda) = f_a(\lambda) b_{\text{nw}}(\lambda) = 2\pi \int_{0^\circ}^{180^\circ} W_a(\theta) \beta(\theta, \lambda) \sin \theta d\theta. \quad (3.42)$$

In practice, VSF may at most be measured at a few wavelengths, while the absorption and attenuation are measured multi- or hyperspectrally by the ac-9/s. The spectral variation of the phase function is also considered to be much smaller than a_{nw} and b_{nw} . Hence, it is of interest to decouple f_a and f_c from b_{nw} . We can solve Eq. 3.39 (including $a + b = c$) for a_{nw} and c_{nw} ,

$$a_{\text{corr}}(\lambda) = a_{\text{meas}}(\lambda) - \frac{f_a(\lambda) [c_{\text{meas}}(\lambda) - a_{\text{meas}}(\lambda)]}{1 - f_a(\lambda) - f_c(\lambda)}, \quad (3.43)$$

$$c_{\text{corr}}(\lambda) = c_{\text{meas}}(\lambda) + \frac{f_c(\lambda) [c_{\text{meas}}(\lambda) - a_{\text{meas}}(\lambda)]}{1 - f_a(\lambda) - f_c(\lambda)}. \quad (3.44)$$

The derived scattering error terms resemble the ε_a of the proportional method. If we let the phase function be spectrally independent, f_a and f_c become constants, the proportional method is recovered with $\varepsilon_a(715 \text{ nm})/b(715 \text{ nm}) = f_a/(1 - f_a - f_c)$. The final objective of *McKee et al. (2013)* was to use measured backscattering ratios to correct the scattering error of both the absorption and attenuation measurements, which was done by finding empirical relationships for f_a and f_c with $b_{b,\text{nw}}/b_{\text{nw}}$, and develop an iterative algorithm to estimate $b_{b,\text{nw}}/b_{\text{nw}}$ from measured values. Since the phase function is difficult to measure accurately, due to its great sensitivity to small-angle scattering, it is Eq. 3.41 that in practice have been used to correct ac-s measurements. Attenuation measurements have to smaller extent been corrected by integrating the forward VSF of LISST-instruments (Eq. 3.40), as there may be confounding factors due to differences between the instruments, such as deflocculation in the ac-9/s pump system or Schlieren effects affecting LISST-instruments (*Boss et al., 2009b*).

Absorption corrections using measured VSF from the MASCOT instrument have been applied in the studies *Stockley et al. (2017)*, *Tonizzo et al. (2017)*, and *Kostakis et al. (2021)*. Since the MASCOT measures the VSF from 10° , the measurements were forward extrapolated using the Fournier-Forand phase function. The corrected absorption measurements showed for the most good agreement with absorption coefficients measured using accurate bench-top instruments, or when compared with radiometric measurements (by forward modelling using measured IOPs). On the other hand, no clear and consistent improvement over the conventional semi-empirical methods could be seen. As *Kostakis et al. (2021)* writes: "No consistent trend could be observed when comparing the semiempirical vs. VSF corrections, that is, sometimes VSF correction outperformed the semiempirical correction and vice versa when compared with PSI-CAM data." *Stockley et al. (2017)* did an in-depth comparison of different scattering corrections from a data set around the British Isles. The proportional semi-empirical method was found to perform the best, together with the VSF-based correction method. Still, residual methods of up to 20% were common even for these methods. Moreover, the flat semi-empirical method agreed better than the proportional variant in clear waters, likely due to enhanced error propagation. The flat variant uses only ac-9/s absorption measurements, the proportional variant uses both absorption and attenuation measurements, while the VSF correction method uses both of these in addition to VSF measurements. Thus, it is the VSF correction method that is the most sensitive to any measurement errors propagating to the corrected absorption coefficients.

To summarise, there are two key questions regarding the scattering errors of the ac-9/s absorption measurements. Firstly, what is most accurate and robust method for estimating scattering errors, especially in the near-infrared? Secondly, how does the scattering error vary with wavelength?

Chapter 4

Introduction to the papers

Paper I: In situ measurements of the volume scattering function with LISST-VSF and LISST-200X in extreme environments: Evaluation of instrument calibration and validity

Sandven, H., Kristoffersen, A. S., Chen, Y. C., and Hamre, B. (2020), Optics Express 28(25).

In **Paper I**, VSF measurements from the LISST-VSF and LISST-200X were calibrated and characterised over the entire measurement range using both polymer bead and *in situ* measurements. Both instruments were found to provide reliable VSF measurements across several orders of magnitude. In the higher scattering detection limit, the instruments are mainly limited by multiple scattering, but also saturation of the photodetectors. In the lower scattering limit, the measurements reach the detection limit (dark current) of the photodetectors. This particularly inhibits the use of the LISST-200X in clear waters. LISST-VSF is more suitable for use in clear waters, but the precision of the eyeball measurements is degraded in extremely clear waters such as the Arctic Ocean. In Paper I, we also demonstrate how the scattering coefficient at 670 nm is estimated by LISST-200X measurements using extrapolation of the VSF, which can be very useful in turbid waters.

Paper I also identified several difficulties with using polystyrene beads for calibration. Due to the extreme dynamical range in the angular VSF in natural waters, which the LISST-instruments have been designed towards, different bead types have to be used for calibrating all angles. For instance, 25 μm beads offer adequate forward scattering to get a valid signal at angles smaller than 1° , but have considerable oscillations impacting other angles. At large angles, large beads are also more sensitive to uncertainties in the complex refractive index of the beads (*Slade and Boss, 2006*), and are also affected by multiple scattering. Small beads, like 0.190 and 0.508 μm , have a much smoother VSF without rapid oscillations, and are thus useful for calibrating a large part of the angular domain. On the other hand, forward scattering of small beads is weaker than the detection limit of the ring detector for all valid particle concentrations. These beads were also impacted by flocculation, leading to erroneously high forward scattering in some cases.

In this paper, I did all of the laboratory measurements and conducted the fieldwork together with co-authors. My contribution also included analyzing the data, making all

the figures and writing most of the manuscript with input and revisions from co-authors.

Paper II: Analysis of multiple scattering errors in LISST-VSF volume scattering function measurements using Monte Carlo simulations and experimental data

Ugulen, H. S., Sandven, H., Hamre, B., Kristoffersen, A. S., and Sætre, C. (2021), Optics Express 29(8).

In **Paper II**, we investigated discrepancies found in turbid LISST-VSF measurements by implementing a Monte Carlo code simulating the LISST-VSF. The three key instrument components to implement were the laser source, ring detector and eyeball detector. For the laser source, photons are sent into the sample volume along the z-axis. The ring detector is implemented as a circular surface at the position of the LISST-VSF optical window. If the photon crosses this boundary surface, it is "detected", and the angle it hit the surface with is stored as a data point. The eyeball detector is implemented as a toroidal surface encircling the laser beam. This enables more photons of different azimuth angles to be detected than if the real eyeball geometry was used. Any photons leaving the boundary surface defined for the sample volume are eliminated and do not contribute to the measured VSF.

Model validation was done by doing experimental measurements on Arizona test dust and 508 nm polystyrene beads with varying concentrations. The model reproduces measurements both for low concentrations and for concentrations far into the multiple scattering regime. Thus, in the study we both validate a model for simulating LISST-VSF instrument, and confirmed that the observed discrepancies in LISST-VSF measurements are due to multiple scattering. For the two scattering agents investigated, the relative error of the scattering coefficient is approximately 10% when the scattering coefficient is 2.7 m^{-1} or 2.9 m^{-1} , while the relative error in the phase function varies considerably between the two phase functions. None of these phase functions are particularly realistic for natural waters, meaning that additional studies must be conducted to assess field measurements.

This paper was built upon discrepancies observed in LISST-VSF *in situ* measurements in turbid waters, and the hypothesis in Paper I that this was caused by multiple scattering. My contribution was conducting and processing the experimental data, interpreting the results, writing parts of the manuscript, and discussion on the overall structure of the study and the manuscript.

Paper III: Efficient Monte Carlo simulations reveal significant multiple scattering errors in underwater angular scattering measurements

Ugulen, H. S., Sandven, H., Hamre, B., Kristoffersen, A. S., and Sætre, C. (2021), Optics Express (Submitted, October 2021)

Paper III further investigated the multiple scattering using more realistic phase functions for natural waters than the ones used to validate the Monte Carlo simulation in Paper II. As realistic phase functions are highly forward-peaked, the simulation in Paper

It requires a large number of simulated photons for the large-angle VSF to converge statistically. A number of strategies were implemented to reduce the computation time. Of particular importance is the *detector directional importance sampling* (DDIS) method. Here, the number of photons heading towards the eyeball detector, which are more likely to contribute to the detected signal than other photons, is artificially enhanced using statistical weighting.

The improved Monte Carlo simulation was used to simulate a wide range of Fournier-Forand and Henley-Greenstein phase functions with different scattering coefficients. The multiple scattering error of both the measured scattering coefficient, backscattering coefficient, and phase function is found to have a first-order variation with the scattering coefficient and a second-order variation with the asymmetry factor. A high asymmetry factor gives a larger multiple scattering. We also demonstrated that for scattering coefficients smaller than 1 m^{-1} , the relative errors for LISST-VSF measurements will be contained below 10%, which offers a useful rule-of-thumb. As several other *in situ* VSF meters have similar path lengths, this results may also have significant implications for historical VSF data sets.

This paper focuses more directly on improving and applying the Monte Carlo model, which has been done primarily by Håvard Ugulen. I contributed to the design and structure of the study, interpretation of the results and some writing.

Paper IV: Into treacherous waters: Corrections of ac-s absorption measurements in coastal waters using volume scattering function measurements

Sandven, H., Petit, T., Chen, Y. C., Kristoffersen, A. S., Erga, S. R., and Hamre, B., (2021), Optics Express (Submitted, September 2021)

In **Paper IV**, we did a detailed comparison of the different correction methods for ac-9/s absorption measurements applied to depth profiles in highly stratified coastal waters in Gaupnefjorden in Western Norway and Storfjorden on Svalbard. The wavelength-independent *semi-empirical* method performed the best, except in the clearest waters where the original *baseline* method showed better agreement with water sample measurements. Similar to other studies, the VSF correction method did not show a clear and consistent improvement over existing methods.

Using high-resolution depth profiles, this study illustrated well error propagation issues with the VSF correction method. For instance, multiple scattering or Schlieren effects can cause the LISST-VSF to measure considerably higher scattering than what is present in reality. Since scattering was the dominating process in the studied waters, artificially high scattering could yield larger scattering errors ϵ_a than the measured absorption. Consequently, the corrected absorption coefficients at these depths became negative. By comparison, errors in the semi-empirical method are proportional to the absorption coefficient instead of the scattering coefficient, and errors will consequently be much smaller in scattering-dominated waters. On a following note, proportional variants gave unreliable and often unphysical results, and were excluded from most of the analysis. Several other studies in coastal waters show a similar trend. We did a small set of Mie simulations showing that perturbations ($<10 \mu\text{m}$ in diameter) to power-law distributions decouples the spectral variation of ϵ_a and b measured by the ac-9/s. Thus,

a subpopulation of small particles may cause the proportional method to fail.

Spatial variations in IOPs can be strong and unpredictable in coastal waters such as in our study. Moreover, ocean currents can cause significant drift between instrument casts. Thus, we observed that concurrent LISST-VSF, ac-s and CTD deployments in some instances measured completely different water masses, with large implications for the correction method. As the LISST-VSF and ac-s are difficult to mount on the same frame, it is also a practical challenge to use the LISST-VSF for ac-s corrections in coastal waters.

This paper is also based on fieldwork with the participation of both myself and the co-authors. I did the majority of the data processing, made the figures and did the writing with revisions from co-authors.

Chapter 5

Concluding remarks and outlook

This thesis has been primarily focused on characterizing volume scattering measurements from the LISST-VSF and LISST-200X instrument, as well as an investigation of the scattering error in ac-9/s absorption measurements and how the error may be corrected with VSF measurements. In particular, the LISST-VSF is the first and only commercially available submersible instrument for measuring the VSF across a wide angular range. *In situ* VSF measurements have for a long time been acknowledged as a large research gap in the optical oceanography community. Backscattering sensors have now been included in the biogeochemical Argo program. There is thus a growing interest to understand the physical properties behind these measurements, as well as their uncertainties.

LISST-VSF and LISST-200X are reliable and trustworthy *in situ* instruments for measuring the VSF within their specific measurement range. The useful measurement ranges found in this doctoral work are illustrated in Figure 5.1. By doing a wide range of measurements in the field and in the laboratory, this thesis has identified prominent error sources which limits the useful range of the LISST-VSF and LISST-200X. This is covered in Paper I and expanded upon in Paper II and III. The LISST-VSF can be severely affected by multiple scattering due to its 0.15 m path length, which was investigated in detail in Paper II and III. We found that the error can be considered negligible (<10%) for typical phase functions only if the scattering coefficient is 1 m^{-1} or smaller, which means accurate measurement range of the LISST-VSF is limited to clear-to-moderate scattering conditions. Moreover, several other VSF meters have a similar path length as the LISST-VSF. Consequently, several of the published VSF measurements throughout the years may also contain non-negligible multiple scattering errors. Hopefully, these errors will be possible to correct with a reasonable accuracy, which seems promising given that the multiple scattering effects appear to behave consistently. LISST-200X is limited by the minimum detectable signal strength to use in moderate-to-turbid waters, but is much less affected by multiple scattering. In the low detection limit, there are also issues with lower precision for the LISST-VSF that needs to be investigated further, especially with high ambient light levels. Schlieren can have considerable effects on both LISST-VSF and LISST-200X measurements, but these effects are spatially limited to stratified layers. Statistical effects of the limited sample volumes should also be assessed in more detail.

Paper IV showed how an application of VSF measurements, namely correcting ac-s absorption measurements, can be affected by multiple scattering and other confounding

factors. Since scattering errors can be much larger than the absorption itself, even small overestimates of the VSF can translate into negative absorption values after correction. Estimating the absorption empirically in the near-infrared is more robust and has a reasonable accuracy. Currently, the larger challenge is to extrapolate the scattering error robustly to the measured wavelengths. The present approach, using the measured scattering coefficient to estimate the spectral slope, is not always reliable and may even give unphysical results. *In situ* VSF measurements combined with modelling can help solve this issue, but the optimal solution is a hyperspectral VSF meter.

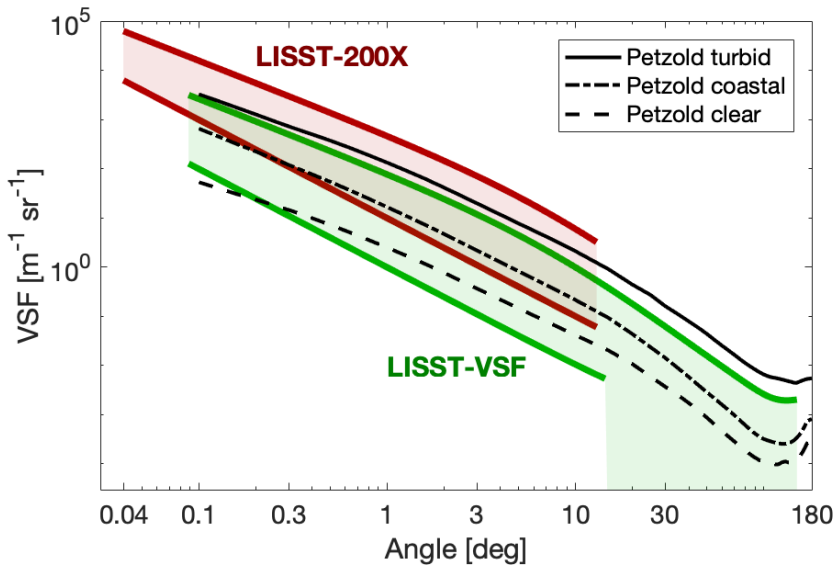


Figure 5.1: Valid measurement ranges for measuring the VSF using the LISST-200X (upper area, in red) or the LISST-VSF (lower area, in green) are plotted together with the Petzold measurements (black lines). The colors also indicate the different wavelengths the instruments use, LISST-200X has a red 670 nm laser; while LISST-VSF uses a green 515 nm laser. These are approximate measurement ranges. The lower limit of the LISST-VSF eyeball detector ($> 15^\circ$) has not been investigated in detail, but is lower than the ring detector.

With the introduction of the LISST-VSF, it is now possible with commercially available instrumentation to achieve high-resolution *in situ* measurements of hyperspectral absorption and attenuation coefficients, multispectral backscattering coefficients, the VSF between $0.1\text{-}150^\circ$ and polarization measurements at 515 nm, as well as a selection of different fluorimeters. This gives a nearly complete picture of the inherent optical properties of the water column. There is a large body of literature concerning the uncertainties of several of these optical instruments, i.e. the uncertainty of a single measurement compared to highly accurate laboratory measurements. By comparison, less work has been done on quantifying uncertainties of the integrated properties, namely under-sampling errors across the vertical column or on the basin-scale. More work should also be done on developing and validating general proxy relationships from *in situ* measurements. Investigating relationships between optical properties and other

measurable quantities in the ocean would increase the overall *usefulness* of optical measurements, both for *in situ* instrumentation and ocean color observations. For instance, the fast, robust and reasonably accurate retrievals of suspended particulate matter concentrations using backscattering measurements on biogeochemical Argo floats have made such optical instrumentation more useful for researchers and other users outside the ocean optics community, and consequently makes more data available for ocean color validation. Even though uncertainties for $a_{c-9/s}$ absorption coefficients may be on the order of 25%, these measurements can still provide valuable information on bio-optical properties that may vary several orders of magnitude across a single depth profile. Comprehensive scattering and absorption measurements with the LISST-VSF, LISST-200X, a_{c-s} or similar instrumentation is needed to further document variations in optical properties around the globe, which can help us identify key variables for monitoring the changing ocean.



Figure 5.2: Optical measurements during the CAATEX 2019 cruise in the Arctic Ocean north of Svalbard.

Bibliography

- Agrawal, Y., A. Whitmire, O. A. Mikkelsen, and H. Pottsmith (2008), Light scattering by random shaped particles and consequences on measuring suspended sediments by laser diffraction, *Journal of Geophysical Research: Oceans*, 113(C4). 2.3.1
- Agrawal, Y. C. (2005), The optical volume scattering function: Temporal and vertical variability in the water column off the New Jersey coast, *Limnology and Oceanography*, 50(6), 1787–1794. 3.1.1
- Agrawal, Y. C., and H. C. Pottsmith (2000), Instruments for particle size and settling velocity observations in sediment transport, *Marine Geology*, 168(1-4), 89–114. 2.3.1, 2.3.1, 3.1.1
- Andrews, S., D. Nover, and S. G. Schladow (2010), Using laser diffraction data to obtain accurate particle size distributions: The role of particle composition, *Limnology and Oceanography: Methods*, 8(10), 507–526. 2.3.1
- Andrews, S., D. Nover, J. Reuter, and S. Schladow (2011a), Limitations of laser diffraction for measuring fine particles in oligotrophic systems: Pitfalls and potential solutions, *Water Resources Research*, 47(5). 3.3
- Andrews, S., D. Nover, K. Reardon, J. Reuter, and S. Schladow (2011b), The influence of ambient light intensity on in situ laser diffractometers, *Water Resources Research*, 47(6). 3.3
- Antoine, D., D. A. Siegel, T. Kostadinov, S. Maritorena, N. B. Nelson, B. Gentili, V. Vellucci, and N. Guillocheau (2011), Variability in optical particle backscattering in contrasting bio-optical oceanic regimes, *Limnology and Oceanography*, 56(3), 955–973. 2.3.1
- Antoine, D., M. Babin, J.-F. Berthon, A. Bricaud, B. Gentili, H. Loisel, S. Maritorena, and D. Stramski (2014), Shedding light on the sea: André Morel’s legacy to optical oceanography, *Annual Review of Marine Science*, 6, 1–21. 2.1
- Apel, J. R. (1987), *Principles of ocean physics*, Academic Press. 2.1, 2.2
- Babin, M., A. Morel, V. Fournier-Sicre, F. Fell, and D. Stramski (2003), Light scattering properties of marine particles in coastal and open ocean waters as related to the particle mass concentration, *Limnology and Oceanography*, 48(2), 843–859. 3
- Baker, D. J. (1981), Ocean instruments and experiment design, in *Evolution of physical oceanography*, edited by B. Warren and C. Wunsch, chap. 14, pp. 396–433, Cambridge, Massachusetts (USA) MIT Press. 2.1

- Bar-On, Y. M., R. Phillips, and R. Milo (2018), The biomass distribution on Earth, *Proceedings of the National Academy of Sciences*, 115(25), 6506–6511. 1
- Basterretxea, G., J. S. Font-Munoz, and I. Tuval (2020), Phytoplankton orientation in a turbulent ocean: A microscale perspective, *Frontiers in Marine Science*, 7, 185. 2.2
- Behrenfeld, M. J. (2014), Climate-mediated dance of the plankton, *Nature Climate Change*, 4(10), 880–887. 2.2
- Behrenfeld, M. J., and P. G. Falkowski (1997), Photosynthetic rates derived from satellite-based chlorophyll concentration, *Limnology and Oceanography*, 42(1), 1–20. 2.2
- Behrenfeld, M. J., R. T. O'Malley, E. S. Boss, T. K. Westberry, J. R. Graff, K. H. Halsey, A. J. Milligan, D. A. Siegel, and M. B. Brown (2016), Reevaluating ocean warming impacts on global phytoplankton, *Nature Climate Change*, 6(3), 323–330. 2.2
- Blondeau-Patissier, D., J. F. Gower, A. G. Dekker, S. R. Phinn, and V. E. Brando (2014), A review of ocean color remote sensing methods and statistical techniques for the detection, mapping and analysis of phytoplankton blooms in coastal and open oceans, *Progress in Oceanography*, 123, 123–144. 1, 2.1, 2.3.2, 2.4
- Boles, E., C. Provost, V. Garçon, C. Bertosio, M. Athanase, Z. Koenig, and N. Senéchaël (2020), Under-ice phytoplankton blooms in the Central Arctic Ocean: Insights from the first biogeochemical IAOOS platform drift in 2017, *Journal of Geophysical Research: Oceans*, 125(3), e2019JC015,608. 2.4
- Boss, E., and W. S. Pegau (2001), Relationship of light scattering at an angle in the backward direction to the backscattering coefficient, *Applied Optics*, 40(30), 5503–5507. 2.3.1, 2.3.1
- Boss, E., M. S. Twardowski, and S. Herring (2001), Shape of the particulate beam attenuation spectrum and its inversion to obtain the shape of the particulate size distribution, *Applied Optics*, 40(27), 4885–4893. 2.3.1
- Boss, E., L. Taylor, S. Gilbert, K. Gundersen, N. Hawley, C. Janzen, T. Johengen, H. Purcell, C. Robertson, D. W. Schar, et al. (2009a), Comparison of inherent optical properties as a surrogate for particulate matter concentration in coastal waters, *Limnology and Oceanography: Methods*, 7(11), 803–810. 2.3.1, 3
- Boss, E., W. H. Slade, M. Behrenfeld, and G. Dall'Olmo (2009b), Acceptance angle effects on the beam attenuation in the ocean, *Optics Express*, 17(3), 1535–1550. 3.4, 3.4
- Boss, E., N. Haëntjens, T. K. Westberry, L. Karp-Boss, and W. H. Slade (2018a), Validation of the particle size distribution obtained with the laser in-situ scattering and transmission (LISST) meter in flow-through mode, *Optics Express*, 26(9), 11,125–11,136. 2.3.1, 2.4

- Boss, E., C. R. Sherwood, P. Hill, and T. Milligan (2018b), Advantages and limitations to the use of optical measurements to study sediment properties, *Applied Sciences*, 8(12), 2692. 2.4
- Boss, E. S., R. Collier, W. Pegau, G. Larson, and K. Fennel (2007), Measurements of spectral optical properties and their relation to biogeochemical variables and processes in Crater Lake, Crater Lake National park, OR, in *Long-term Limnological Research and Monitoring at Crater Lake, Oregon*, pp. 149–159, Springer. 2.3.2
- Bricaud, A., A. Morel, M. Babin, K. Allali, and H. Claustre (1998), Variations of light absorption by suspended particles with chlorophyll a concentration in oceanic (Case 1) waters: Analysis and implications for bio-optical models, *Journal of Geophysical Research: Oceans*, 103(C13), 31,033–31,044. 2.3.2, 3
- Buras, R., and B. Mayer (2011), Efficient unbiased variance reduction techniques for Monte Carlo simulations of radiative transfer in cloudy atmospheres: The solution, *Journal of Quantitative Spectroscopy and Radiative Transfer*, 112(3), 434–447. 3.2
- Chai, F., K. S. Johnson, H. Claustre, X. Xing, Y. Wang, E. Boss, S. Riser, K. Fennel, O. Schofield, and A. Sutton (2020), Monitoring ocean biogeochemistry with autonomous platforms, *Nature Reviews Earth & Environment*, 1(6), 315–326. 2.4
- Chami, M., E. Shybanov, T. Churilova, G. Khomenko, M.-G. Lee, O. Martynov, G. Berseneva, and G. Korotaev (2005), Optical properties of the particles in the Crimea coastal waters (Black Sea), *Journal of Geophysical Research: Oceans*, 110(C11). 2.3.1
- Chami, M., E. Marken, J. Stamnes, G. Khomenko, and G. Korotaev (2006a), Variability of the relationship between the particulate backscattering coefficient and the volume scattering function measured at fixed angles, *Journal of Geophysical Research: Oceans*, 111(C5). 2.3.1
- Chami, M., D. McKee, E. Leymarie, and G. Khomenko (2006b), Influence of the angular shape of the volume-scattering function and multiple scattering on remote sensing reflectance, *Applied Optics*, 45(36), 9210–9220. 3.3
- Chase, A., E. Boss, R. Zaneveld, A. Bricaud, H. Claustre, J. Ras, G. Dall’Olmo, and T. K. Westberry (2013), Decomposition of in situ particulate absorption spectra, *Methods in Oceanography*, 7, 110–124. 2.3.2
- Chinnici, I., and G. Consolmagno (Eds.) (2021), *Angelo Secchi and Nineteenth Century Science: The Multidisciplinary Contributions of a Pioneer and Innovator*, Springer International Publishing. 2.1
- Clarke, G. L., G. C. Ewing, and C. J. Lorenzen (1970), Spectra of backscattered light from the sea obtained from aircraft as a measure of chlorophyll concentration, *Science*, 167(3921), 1119–1121. 2.1
- Claustre, H., K. S. Johnson, and Y. Takeshita (2020), Observing the global ocean with biogeochemical-Argo, *Annual Review of Marine Science*, 12, 23–48. 1, 2.2, 2.4, 3

- Clavano, W. R., E. Boss, and L. Karp-Boss (2007), Inherent optical properties of non-spherical marine-like particles – from theory to observation, *Oceanography and Marine Biology: An Annual Review*, 45, 1–38. 2.3.1, 2.3.1
- Cloern, J. E., S. Foster, and A. Kleckner (2014), Phytoplankton primary production in the world's estuarine-coastal ecosystems, *Biogeosciences*, 11(9), 2477–2501. 2.2
- Costanza, R. (1999), The ecological, economic, and social importance of the oceans, *Ecological Economics*, 31(2), 199–213. 1
- Crain, C. M., K. Kroeker, and B. S. Halpern (2008), Interactive and cumulative effects of multiple human stressors in marine systems, *Ecology Letters*, 11(12), 1304–1315. 2.2
- Crowther, T. W., H. B. Glick, K. R. Covey, C. Bettigole, D. S. Maynard, S. M. Thomas, J. R. Smith, G. Hintler, M. C. Duguid, G. Amatulli, et al. (2015), Mapping tree density at a global scale, *Nature*, 525(7568), 201–205. 1
- Dall'Olmo, G., T. Westberry, M. Behrenfeld, E. Boss, and W. Slade (2009), Significant contribution of large particles to optical backscattering in the open ocean, *Biogeosciences*, 6(6), 947–967. 2.3.2
- Davies, E. J., W. A. M. Nimmo-Smith, Y. C. Agrawal, and A. J. Souza (2012), LISST-100 response to large particles, *Marine Geology*, 307, 117–122. 2.3.1
- Davies, E. J., S. L. Basedow, and D. McKee (2021), The hidden influence of large particles on ocean colour, *Scientific Reports*, 11(1), 1–9. 3.3
- Dierssen, H. M. (2010), Perspectives on empirical approaches for ocean color remote sensing of chlorophyll in a changing climate, *Proceedings of the National Academy of Sciences*, 107(40), 17,073–17,078. 3
- Doney, S. C., V. J. Fabry, R. A. Feely, and J. A. Kleypas (2009), Ocean acidification: The other CO₂ problem, *Annual Review of Marine Science*, 1, 169–192. 2.2
- Doney, S. C., M. Ruckelshaus, J. Emmett Duffy, J. P. Barry, F. Chan, C. A. English, H. M. Galindo, J. M. Grebmeier, A. B. Hollowed, N. Knowlton, J. Polovina, N. N. Rabalais, W. J. Sydeman, and L. D. Talley (2012), Climate change impacts on marine ecosystems, *Annual Review of Marine Science*, 4, 11–37. 2.2
- Doxaran, D., E. Leymarie, B. Nechad, A. Dogliotti, K. Ruddick, P. Gernez, and E. Knaeps (2016), Improved correction methods for field measurements of particulate light backscattering in turbid waters, *Optics Express*, 24(4), 3615–3637. 2.3.3
- Eckhardt, R., S. Ulam, and J. Von Neumann (1987), Stan Ulam, John Von Neumann and the Monte Carlo method, *Los Alamos Science*, 15, 131. 3.2
- El Serafy, G. Y., B. A. Schaeffer, M.-B. Neely, A. Spinosa, D. Odermatt, K. C. Weathers, T. Baracchini, D. Bouffard, L. Carvalho, R. N. Conmy, et al. (2021), Integrating inland and coastal water quality data for actionable knowledge, *Remote Sensing*, 13(15), 2899. 3.2

- Felix, D., I. Albayrak, and R. M. Boes (2018), In-situ investigation on real-time suspended sediment measurement techniques: Turbidimetry, acoustic attenuation, laser diffraction (LISST) and vibrating tube densimetry, *International journal of sediment research*, 33(1), 3–17. 2.3.1
- Field, C. B., M. J. Behrenfeld, J. T. Randerson, and P. Falkowski (1998), Primary production of the biosphere: Integrating terrestrial and oceanic components, *Science*, 281(5374), 237–240. 2.3.2
- Fournier, G. R., and J. L. Forand (1994), Analytic phase function for ocean water, in *Ocean Optics XII*, vol. 2258, pp. 194–201, International Society for Optics and Photonics. 2.3.1
- Frette, Ø., S. Rune Erga, B. Hamre, J. Aure, and J. J. Stamnes (2004), Seasonal variability in inherent optical properties in a western Norwegian fjord, *Sarsia North Atlantic Marine Science*, 89(4), 276–291. 3
- Frigstad, H., Ø. Kaste, A. Deininger, K. Kvalsund, G. Christensen, R. G. Bellerby, K. Sørensen, M. Norli, and A. L. King (2020), Influence of riverine input on Norwegian coastal systems, *Frontiers in Marine Science*, 7, 332. 2.2
- Gershun, A. (1939), The light field, *Journal of Mathematics and Physics*, 18(1-4), 51–151. 2.3.3
- Gordon, H. R., and G. C. Boynton (1998), Radiance–irradiance inversion algorithm for estimating the absorption and backscattering coefficients of natural waters: vertically stratified water bodies, *Applied Optics*, 37(18), 3886–3896. 2.3.3
- Guo, H.-D., L. Zhang, and L.-W. Zhu (2015), Earth observation big data for climate change research, *Advances in Climate Change Research*, 6(2), 108–117. 1
- Hovis, W., D. Clark, F. Anderson, R. Austin, W. Wilson, E. Baker, D. Ball, H. Gordon, J. Mueller, S. El-Sayed, et al. (1980), Nimbus-7 Coastal Zone Color Scanner: System description and initial imagery, *Science*, 210(4465), 60–63. 2.1
- Hu, L., X. Zhang, Y. Xiong, and M.-X. He (2019), Calibration of the LISST-VSF to derive the volume scattering functions in clear waters, *Optics Express*, 27(16), A1188–A1206. 3.1.2, 3.1.2, 3.1.2, 3.1.2, 3.3, 3.3
- Huntford, R. (1997), *Nansen: The Explorer as Hero*, Abacus. 2.1
- Huot, Y., A. Morel, M. Twardowski, D. Stramski, and R. Reynolds (2008), Particle optical backscattering along a chlorophyll gradient in the upper layer of the eastern South Pacific Ocean, *Biogeosciences*, 5(2), 495–507. 2.3.1
- IPCC (2021), Climate Change 2021: The Physical Science Basis. Contribution of Working Group I to the Sixth Assessment Report of the Intergovernmental Panel on Climate Change, Masson-Delmotte, V., P. Zhai, A. Pirani, S. L. Connors, C. Péan, S. Berger, N. Caud, Y. Chen, L. Goldfarb, M. I. Gomis, M. Huang, K. Leitzell, E. Lonnoy, J. B. R. Matthews, T. K. Maycock, T. Waterfield, O. Yelekçi, R. Yu and B. Zhou (eds.). Cambridge University Press. *In Press*. 2.2

- Jerlov, N. G. (1968), *Optical Oceanography*, Elsevier. 2.1
- Jin, Z., and K. Stamnes (1994), Radiative transfer in nonuniformly refracting layered media: Atmosphere–ocean system, *Applied Optics*, 33(3), 431–442. 2.3.3
- Johnson, G. C., S. Hosoda, S. R. Jayne, P. R. Oke, S. C. Riser, D. Roemmich, T. Suga, V. Thierry, S. E. Wijffels, and J. Xu (2021), Argo—Two Decades: Global Oceanography, Revolutionized, *Annual Review of Marine Science*, 14. 1
- Johnson, K. S., F. P. Chavez, and G. E. Friederich (1999), Continental-shelf sediment as a primary source of iron for coastal phytoplankton, *Nature*, 398(6729), 697–700. 2.2
- Jonasz, M., and G. Fournier (2011), *Light Scattering by Particles in Water: Theoretical and Experimental Foundations*, Elsevier. 3.3
- Karageorgis, A., D. Georgopoulos, W. Gardner, O. Mikkelsen, and D. Velaoras (2015), How schlieren affects beam transmissometers and LISST-Deep: An example from the stratified Danube River delta, NW Black Sea, *Mediterranean Marine Science*, 16(2), 366–372. 3.3
- Karp-Boss, L., L. Azevedo, and E. Boss (2007), LISST-100 measurements of phytoplankton size distribution: Evaluation of the effects of cell shape, *Limnology and Oceanography: Methods*, 5(11), 396–406. 2.3.1
- Keeling, R. F., A. Körtzinger, and N. Gruber (2010), Ocean deoxygenation in a warming world, *Annual Review of Marine Science*, 2, 199–229. 2.2
- Kirk, J. (1992), Monte Carlo modeling of the performance of a reflective tube absorption meter, *Applied Optics*, 31(30), 6463–6468. 2.3.3, 3.4
- Koestner, D., D. Stramski, and R. A. Reynolds (2018), Measurements of the volume scattering function and the degree of linear polarization of light scattered by contrasting natural assemblages of marine particles, *Applied Sciences*, 8(12), 2690. 3.1.2, 3.3
- Koestner, D., D. Stramski, and R. A. Reynolds (2020), Polarized light scattering measurements as a means to characterize particle size and composition of natural assemblages of marine particles, *Applied Optics*, 59(27), 8314–8334. 2.3.1, 3.1.2, 3.1.2, 3.1.2
- Kostakis, I., M. Twardowski, C. Roesler, R. Röttgers, D. Stramski, D. McKee, A. Tonizzo, and S. Drapeau (2021), Hyperspectral optical absorption closure experiment in complex coastal waters, *Limnology and Oceanography: Methods*. 2.3.2, 2.3.3, 3.4
- Kulk, G., T. Platt, J. Dingle, T. Jackson, B. F. Jönsson, H. A. Bouman, M. Babin, R. J. Brewin, M. Doblin, M. Estrada, et al. (2020), Primary production, an index of climate change in the ocean: Satellite-based estimates over two decades, *Remote Sensing*, 12(5), 826. 2.4, 3

- Lee, M. E., and M. R. Lewis (2003), A new method for the measurement of the optical volume scattering function in the upper ocean, *Journal of Atmospheric and Oceanic Technology*, 20(4), 563–571. 2.3.1
- Lee, Z., A. Weidemann, J. Kindle, R. Arnone, K. L. Carder, and C. Davis (2007), Euphotic zone depth: Its derivation and implication to ocean-color remote sensing, *Journal of Geophysical Research: Oceans*, 112(C3). 2.2
- Lefering, I., R. Röttgers, C. Utschig, M. S. Twardowski, and D. McKee (2018), Measurement uncertainties in PSICAM and reflective tube absorption meters, *Optics Express*, 26(19), 24,384–24,402. 3.4
- Leymarie, E., D. Doxaran, and M. Babin (2010), Uncertainties associated to measurements of inherent optical properties in natural waters, *Applied Optics*, 49(28), 5415–5436. 3.4
- Li, G., L. Cheng, J. Zhu, K. E. Trenberth, M. E. Mann, and J. P. Abraham (2020), Increasing ocean stratification over the past half-century, *Nature Climate Change*, 10(12), 1116–1123. 2.2
- Liu, D., P. Xu, Y. Zhou, W. Chen, B. Han, X. Zhu, Y. He, Z. Mao, C. Le, P. Chen, et al. (2019), Lidar remote sensing of seawater optical properties: Experiment and Monte Carlo simulation, *IEEE Transactions on Geoscience and Remote Sensing*, 57(11), 9489–9498. 2.3.3
- Liu, Y., R. Röttgers, M. Ramírez-Pérez, T. Dinter, F. Steinmetz, E.-M. Nöthig, S. Hellmann, S. Wiegmann, and A. Bracher (2018), Underway spectrophotometry in the Fram Strait (European Arctic Ocean): A highly resolved chlorophyll-a data source for complementing satellite ocean color, *Optics Express*, 26(14), A678–A696. 2.3.2
- Martínez, M. L., A. Intralawan, G. Vázquez, O. Pérez-Maqueo, P. Sutton, and R. Landgrave (2007), The coasts of our world: Ecological, economic and social importance, *Ecological Economics*, 63(2-3), 254–272. 2.2
- McKee, D., and A. Cunningham (2005), Evidence for wavelength dependence of the scattering phase function and its implication for modeling radiance transfer in shelf seas, *Applied Optics*, 44(1), 126–135. 3.4
- McKee, D., M. Chami, I. Brown, V. S. Calzado, D. Doxaran, and A. Cunningham (2009), Role of measurement uncertainties in observed variability in the spectral backscattering ratio: a case study in mineral-rich coastal waters, *Applied Optics*, 48(24), 4663–4675. 2.3.1
- McKee, D., J. Piskozub, R. Röttgers, and R. A. Reynolds (2013), Evaluation and improvement of an iterative scattering correction scheme for in situ absorption and attenuation measurements, *Journal of Atmospheric and Oceanic Technology*, 30(7), 1527–1541. 3.4, 3.4, 3.4
- Mie, G. (1908), Beiträge zur optik trüber medien, speziell kolloidaler metallösungen, *Annalen der physik*, 330(3), 377–445. 2.3.1

- Mikkelsen, O. A., T. G. Milligan, P. S. Hill, R. J. Chant, C. F. Jago, S. E. Jones, V. Krivtsov, and G. Mitchelson-Jacob (2008), The influence of schlieren on in situ optical measurements used for particle characterization, *Limnology and Oceanography: Methods*, 6(3), 133–143. 3.3
- Miles, T., W. Slade, and S. Glenn (2021), Sediment resuspension and transport from a glider integrated Laser In Situ Scattering and Transmissometry (LISST) particle analyzer, *Journal of Atmospheric and Oceanic Technology*. 3.3
- Mishchenko, M. I. (2009), Gustav Mie and the fundamental concept of electromagnetic scattering by particles: A perspective, *Journal of Quantitative Spectroscopy and Radiative Transfer*, 110(14-16), 1210–1222. 2.3.1, 3.2
- Mishchenko, M. I., L. D. Travis, and D. W. Mackowski (1996), T-matrix computations of light scattering by nonspherical particles: A review, *Journal of Quantitative Spectroscopy and Radiative Transfer*, 55(5), 535–575. 2.3.1
- Mobley, C. D. (1994), *Light and Water: Radiative Transfer in Natural Waters*, Academic Press. 1, 2.3
- Mobley, C. D., L. K. Sundman, and E. Boss (2002), Phase function effects on oceanic light fields, *Applied Optics*, 41(6), 1035–1050. 2.3.1
- Mobley, C. D., D. Stramski, W. Paul Bissett, and E. Boss (2004), Optical modeling of ocean waters: Is the case 1-case 2 classification still useful?, *Oceanography*, 17(SPL. ISS. 2), 60. 2.3.2
- Moore, C., A. Barnard, P. Fietzek, M. R. Lewis, H. M. Sosik, S. White, and O. Zielinski (2009), Optical tools for ocean monitoring and research, *Ocean Science*, 5(4), 661–684. 2.1
- Moore, C. C., J. R. V. Zaneveld, and J. C. Kitchen (1992), Preliminary results from an in-situ spectral absorption meter, in *Ocean Optics XI*, vol. 1750, pp. 330–337, International Society for Optics and Photonics. 3.4
- Moore, J. K., W. Fu, F. Primeau, G. L. Britten, K. Lindsay, M. Long, S. C. Doney, N. Mahowald, F. Hoffman, and J. T. Randerson (2018), Sustained climate warming drives declining marine biological productivity, *Science*, 359(6380), 1139–1143. 2.2
- Morel, A., B. Gentili, H. Claustre, M. Babin, A. Bricaud, J. Ras, and F. Tieche (2007), Optical properties of the clearest natural waters, *Limnology and Oceanography*, 52(1), 217–229. 2.2
- Moses, W. J., S. G. Ackleson, J. W. Hair, C. A. Hostetler, and W. D. Miller (2016), Spatial scales of optical variability in the coastal ocean: Implications for remote sensing and in situ sampling, *Journal of Geophysical Research: Oceans*, 121(6), 4194–4208. 3
- Munk, W. (2013), The perfect storm, *Proceedings of the American Philosophical Society*, 157(4), 369–392. 2.1

- Nerem, R. S., B. D. Beckley, J. T. Fasullo, B. D. Hamlington, D. Masters, and G. T. Mitchum (2018), Climate-change-driven accelerated sea-level rise detected in the altimeter era, *Proceedings of the National Academy of Sciences*, 115(9), 2022–2025. 2.2
- Neukermans, G., H. Loisel, X. Mériaux, R. Astoreca, and D. McKee (2012), In situ variability of mass-specific beam attenuation and backscattering of marine particles with respect to particle size, density, and composition, *Limnology and Oceanography*, 57(1), 124–144. 2.3.1
- Nima, C., Ø. Frette, B. Hamre, J. J. Stamnes, Y.-C. Chen, K. Sørensen, M. Norli, D. Lu, Q. Xing, D. Muyimbwa, et al. (2019), CDOM absorption properties of natural water bodies along extreme environmental gradients, *Water*, 11(10), 1988. 2.3.2
- Oishi, T. (1990), Significant relationship between the backward scattering coefficient of sea water and the scatterance at 120°, *Applied Optics*, 29(31), 4658–4665. 2.3.1
- Onarheim, I. H., T. Eldevik, L. H. Smedsrud, and J. C. Stroeve (2018), Seasonal and regional manifestation of Arctic sea ice loss, *Journal of Climate*, 31(12), 4917–4932. 2.2
- Opdal, A. F., C. Lindemann, and D. L. Aksnes (2019), Centennial decline in North Sea water clarity causes strong delay in phytoplankton bloom timing, *Global Change Biology*, 25(11), 3946–3953. 2.1, 2.2
- Organelli, E., G. Dall’Olmo, R. J. Brewin, G. A. Tarran, E. Boss, and A. Bricaud (2018), The open-ocean missing backscattering is in the structural complexity of particles, *Nature Communications*, 9(1), 1–11. 2.3.1
- Organelli, E., G. Dall’Olmo, R. J. Brewin, F. Nencioli, and G. A. Tarran (2020), Drivers of spectral optical scattering by particles in the upper 500 m of the Atlantic Ocean, *Optics Express*, 28(23), 34,147–34,166. 2.3.1
- Petit, T., B. Hamre, H. Sandven, R. Röttgers, P. Kowalczyk, M. Zablocka, and M. Granskog (2021), Inherent optical properties and optical characteristics of dissolved organic and particulate matter in the Storfjorden (Svalbard) in early summer, *Ocean Science. Preprint*. 2.6
- Petzold, T. J. (1972), Volume scattering functions for selected ocean waters, *Tech. rep.*, Scripps Institution of Oceanography. 2.3.1
- Piskozub, J., D. Stramski, E. Terrill, and W. K. Melville (2004), Influence of forward and multiple light scatter on the measurement of beam attenuation in highly scattering marine environments, *Applied Optics*, 43(24), 4723–4731. 2.3.3, 3.3
- Pitarch, J. (2020), A review of Secchi’s contribution to marine optics and the foundation of Secchi disk science, *Oceanography*, 33(3), 26–37. 2.1, 2.1
- Polyakov, I. V., A. V. Pnyushkov, M. B. Alkire, I. M. Ashik, T. M. Baumann, E. C. Carmack, I. Goszczko, J. Guthrie, V. V. Ivanov, T. Kanzow, et al. (2017), Greater role for Atlantic inflows on sea-ice loss in the Eurasian Basin of the Arctic Ocean, *Science*, 356(6335), 285–291. 2.2

- Poole, L. R., D. D. Venable, and J. W. Campbell (1981), Semianalytic Monte Carlo radiative transfer model for oceanographic lidar systems, *Applied Optics*, 20(20), 3653–3656. 2.3.3
- Ramírez-Pérez, M., M. Twardowski, C. Trees, J. Piera, and D. McKee (2018), Inversion of in situ light absorption and attenuation measurements to estimate constituent concentrations in optically complex shelf seas, *Journal of Geophysical Research: Oceans*, 123(1), 720–737. 2.3.2
- Reynolds, R. A., D. Stramski, and G. Neukermans (2016), Optical backscattering by particles in Arctic seawater and relationships to particle mass concentration, size distribution, and bulk composition, *Limnology and Oceanography*, 61(5), 1869–1890. 2.3.1
- Roemmich, D., M. H. Alford, H. Claustre, K. Johnson, B. King, J. Moum, P. Oke, W. B. Owens, S. Pouliquen, S. Purkey, et al. (2019), On the future of Argo: A global, full-depth, multi-disciplinary array, *Frontiers in Marine Science*, 6, 439. 2.3.1
- Roesler, C., J. Uitz, H. Claustre, E. Boss, X. Xing, E. Organelli, N. Briggs, A. Bricaud, C. Schmechtig, A. Poteau, et al. (2017), Recommendations for obtaining unbiased chlorophyll estimates from in situ chlorophyll fluorometers: A global analysis of WET Labs ECO sensors, *Limnology and Oceanography: Methods*, 15(6), 572–585. 3
- Röttgers, R., D. McKee, and S. B. Woźniak (2013), Evaluation of scatter corrections for ac-9 absorption measurements in coastal waters, *Methods in Oceanography*, 7, 21–39. 2.3.2, 3.4, 3.4
- Ryabinin, V., J. Barbière, P. Haugan, G. Kullenberg, N. Smith, C. McLean, A. Troisi, A. Fischer, S. Aricò, T. Aarup, et al. (2019), The UN decade of ocean science for sustainable development, *Frontiers in Marine Science*, 6, 470. 1, 1
- Sequoia Scientific Inc. (2020), LISST-200X User’s manual, www.sequoiasci.com/wp-content/uploads/2016/02/LISST-200X-Users-Manual-v2_1.pdf, (Version 2.1). 3.3
- Siegel, D. A., K. O. Buesseler, M. J. Behrenfeld, C. R. Benitez-Nelson, E. Boss, M. A. Brzezinski, A. Burd, C. A. Carlson, E. A. D’Asaro, S. C. Doney, et al. (2016), Prediction of the export and fate of global ocean net primary production: The exports science plan, *Frontiers in Marine Science*, 3, 22. 2.2
- Slade, W. H., and E. Boss (2015), Spectral attenuation and backscattering as indicators of average particle size, *Applied Optics*, 54(24), 7264–7277. 2.3.1
- Slade, W. H., and E. S. Boss (2006), Calibrated near-forward volume scattering function obtained from the LISST particle sizer, *Optics Express*, 14(8), 3602–3615. 2.3.1, 3.1.1, 4
- Slade, W. H., E. Boss, G. Dall’Olmo, M. R. Langner, J. Loftin, M. J. Behrenfeld, C. Roesler, and T. K. Westberry (2010), Underway and moored methods for improving accuracy in measurement of spectral particulate absorption and attenuation, *Journal of Atmospheric and Oceanic Technology*, 27(10), 1733–1746. 2.3.2, 2.4

- Slade, W. H., Y. C. Agrawal, and O. A. Mikkelsen (2013), Comparison of measured and theoretical scattering and polarization properties of narrow size range irregular sediment particles, in *2013 OCEANS-San Diego*, pp. 1–6, IEEE. 1, 2.3.1, 2.3.1
- Soja-Woźniak, M., M. Baird, T. Schroeder, Y. Qin, L. Clementson, B. Baker, D. Boadle, V. Brando, and A. D. Steven (2019), Particulate backscattering ratio as an indicator of changing particle composition in coastal waters: Observations from Great Barrier Reef waters, *Journal of Geophysical Research: Oceans*, 124(8), 5485–5502. 2.3.1
- Stamnes, K., and J. J. Stamnes (2016), *Radiative Transfer in Coupled Environmental Systems: An Introduction to Forward and Inverse Modeling*, John Wiley & Sons. 2.3.3
- Stockley, N. D., R. Röttgers, D. McKee, I. Lefering, J. M. Sullivan, and M. S. Twardowski (2017), Assessing uncertainties in scattering correction algorithms for reflective tube absorption measurements made with a WET Labs ac-9, *Optics Express*, 25(24), A1139–A1153. 2.3.2, 3.4, 3.4, 3.4
- Stramski, D., E. Boss, D. Bogucki, and K. J. Voss (2004), The role of seawater constituents in light backscattering in the ocean, *Progress in Oceanography*, 61(1), 27–56. 2.3.1
- Styles, R. (2006), Laboratory evaluation of the LISST in a stratified fluid, *Marine Geology*, 227(1-2), 151–162. 3.3
- Sullivan, J. M., and M. S. Twardowski (2009), Angular shape of the oceanic particulate volume scattering function in the backward direction, *Applied Optics*, 48(35), 6811–6819. 2.3.1, 2.3.1
- Sullivan, J. M., M. S. Twardowski, J. R. V. Zaneveld, C. M. Moore, A. H. Barnard, P. L. Donaghay, and B. Rhoades (2006), Hyperspectral temperature and salt dependencies of absorption by water and heavy water in the 400–750 nm spectral range, *Applied Optics*, 45(21), 5294–5309. 2.3.2
- Sun, D., X. Su, S. Wang, Z. Qiu, Z. Ling, Z. Mao, and Y. He (2019), Variability of particulate backscattering ratio and its relations to particle intrinsic features in the Bohai Sea, Yellow Sea, and East China Sea, *Optics Express*, 27(3), 3074–3090. 2.3.1
- Takami, H., A. Inoue, F. Fuji, and K. Horikoshi (1997), Microbial flora in the deepest sea mud of the Mariana Trench, *FEMS Microbiology Letters*, 152(2), 279–285. 2.2
- Tassan, S., and G. M. Ferrari (2003), Variability of light absorption by aquatic particles in the near-infrared spectral region, *Applied Optics*, 42(24), 4802–4810. 3.4
- Tonizzo, A., M. Twardowski, S. McLean, K. Voss, M. Lewis, and C. Trees (2017), Closure and uncertainty assessment for ocean color reflectance using measured volume scattering functions and reflective tube absorption coefficients with novel correction for scattering, *Applied Optics*, 56(1), 130–146. 3.4

- Twardowski, M., X. Zhang, S. Vagle, J. Sullivan, S. Freeman, H. Czerski, Y. You, L. Bi, and G. Kattawar (2012), The optical volume scattering function in a surf zone inverted to derive sediment and bubble particle subpopulations, *Journal of Geophysical Research: Oceans*, 117(C7). 2.3.1
- Twardowski, M. S., J. M. Sullivan, P. L. Donaghay, and J. R. V. Zaneveld (1999), Microscale quantification of the absorption by dissolved and particulate material in coastal waters with an ac-9, *Journal of Atmospheric and Oceanic Technology*, 16(6), 691–707. 2.3.1, 2.3.2, 3
- Twardowski, M. S., E. Boss, J. B. Macdonald, W. S. Pegau, A. H. Barnard, and J. R. V. Zaneveld (2001), A model for estimating bulk refractive index from the optical backscattering ratio and the implications for understanding particle composition in case i and case ii waters, *Journal of Geophysical Research: Oceans*, 106(C7), 14,129–14,142. 2.3.1, 2.3.1
- Twardowski, M. S., M. R. Lewis, A. H. Barnard, and J. R. V. Zaneveld (2007), In-water instrumentation and platforms for ocean color remote sensing applications, in *Remote Sensing of Coastal Aquatic Environments*, pp. 69–100, Springer. 2.4
- Ulloa, O., S. Sathyendranath, and T. Platt (1994), Effect of the particle-size distribution on the backscattering ratio in seawater, *Applied Optics*, 33(30), 7070–7077. 2.3.1, 2.3.1
- van de Hulst, H. C. (1981), *Light Scattering by Small Particles*, Courier Corporation. 2.3.1, 3.3
- Watanabe, F., T. Rodrigues, A. Do Carmo, E. Alcântara, M. Shimabukuro, N. Imai, N. Bernardo, and L. H. Rotta (2018), Assessment of scattering error correction techniques for ac-s meter in a tropical eutrophic reservoir, *Remote Sensing*, 10(5), 740. 2
- Webster, J. G., and H. Eren (2018), *Measurement, Instrumentation, and Sensors Handbook: Two-Volume Set*, CRC press. 3
- Werdell, P. J., L. I. McKinna, E. Boss, S. G. Ackleson, S. E. Craig, W. W. Gregg, Z. Lee, S. Maritorena, C. S. Roesler, C. S. Rousseaux, et al. (2018), An overview of approaches and challenges for retrieving marine inherent optical properties from ocean color remote sensing, *Progress in Oceanography*, 160, 186–212. 2.1, 2.3.1, 2.3.2, 2.3.2, 2.3.3, 2.4
- Werdell, P. J., M. J. Behrenfeld, P. S. Bontempi, E. Boss, B. Cairns, G. T. Davis, B. A. Franz, U. B. Gliese, E. T. Gorman, O. Hasekamp, et al. (2019), The Plankton, Aerosol, Cloud, ocean Ecosystem mission: Status, science, advances, *Bulletin of the American Meteorological Society*, 100(9), 1775–1794. 2.3.1
- Wernand, M. R. (2010), On the history of the Secchi disc, *Journal of the European Optical Society-Rapid Publications*, 5. 2.1
- Whitmire, A. L., E. Boss, T. J. Cowles, and W. S. Pegau (2007), Spectral variability of the particulate backscattering ratio, *Optics Express*, 15(11), 7019–7031. 2.3.1

- Whitmire, A. L., R. M. Letelier, V. Villagrán, and O. Ulloa (2009), Autonomous observations of in vivo fluorescence and particle backscattering in an oceanic oxygen minimum zone, *Optics Express*, 17(24), 21,992–22,004. 3
- Whitmire, A. L., W. S. Pegau, L. Karp-Boss, E. Boss, and T. J. Cowles (2010), Spectral backscattering properties of marine phytoplankton cultures, *Optics Express*, 18(14), 15,073–15,093. 2.3.1
- Wijffels, S., D. Roemmich, D. Monselesan, J. Church, and J. Gilson (2016), Ocean temperatures chronicle the ongoing warming of Earth, *Nature Climate Change*, 6(2), 116–118. 2.2
- Wong, J., S. C. Liew, and E. Wong (2020), Simple method to extend the range of ECO-BB for waters with high backscattering coefficient, *Applied Optics*, 59(31), 9690–9697. 2.3.1
- Zaneveld, J. R. V. (2013), Fifty years of inherent optical properties, *Methods in Oceanography*, 7, 3–20. 2.1
- Zaneveld, J. R. V., J. C. Kitchen, and C. C. Moore (1994), Scattering error correction of reflection-tube absorption meters, in *Ocean Optics XII*, vol. 2258, pp. 44–55, International Society for Optics and Photonics. 3.4
- Zhai, P.-W., G. W. Kattawar, and P. Yang (2008), Impulse response solution to the three-dimensional vector radiative transfer equation in atmosphere-ocean systems. I. Monte Carlo method, *Applied Optics*, 47(8), 1037–1047. 2.3.3
- Zhang, X., M. Twardowski, and M. Lewis (2011), Retrieving composition and sizes of oceanic particle subpopulations from the volume scattering function, *Applied Optics*, 50(9), 1240–1259. 2.3.1
- Zhang, X., D. J. Gray, Y. Huot, Y. You, and L. Bi (2012), Comparison of optically derived particle size distributions: Scattering over the full angular range versus diffraction at near forward angles, *Applied Optics*, 51(21), 5085–5099. 2.3.1
- Zhang, X., Y. Huot, D. Gray, A. Weidemann, and W. Rhea (2013), Biogeochemical origins of particles obtained from the inversion of the volume scattering function and spectral absorption in coastal waters, *Biogeosciences*, 10(9), 6029–6043. 2.3.1
- Zhang, X., R. H. Stavn, A. U. Falster, D. Gray, and R. W. Gould Jr (2014), New insight into particulate mineral and organic matter in coastal ocean waters through optical inversion, *Estuarine, coastal and shelf science*, 149, 1–12. 2.3.1
- Zhang, X., L. Hu, Y. Xiong, Y. Huot, and D. Gray (2020), Experimental estimates of optical backscattering associated with submicron particles in clear oceanic waters, *Geophysical Research Letters*, 47(4), e2020GL087,100. 3.3
- Zhang, X., L. Hu, D. Gray, and Y. Xiong (2021), Shape of particle backscattering in the North Pacific Ocean: The χ factor, *Applied Optics*, 60(5), 1260–1266. 2.3.1, 2.3.1

Chapter 6

Scientific results

Paper I

In situ measurements of the volume scattering function with LISST-VSF and LISST-200X in extreme environments: Evaluation of instrument calibration and validity

Håkon Sandven, Arne S. Kristoffersen, Yi-Chun Chen, and Børge Hamre (2020), *Optics Express*, **28(25)**, 37373-37396, doi:10.1364/OE.411177



In situ measurements of the volume scattering function with LISST-VSF and LISST-200X in extreme environments: evaluation of instrument calibration and validity

HÅKON SANDVEN, ARNE S. KRISTOFFERSEN, YI-CHUN CHEN, AND BØRGE HAMRE*

Department of Physics and Technology, University of Bergen, Allegaten 55, 5007 Bergen, Norway

*borge.hamre@uib.no

Abstract: The LISST-VSF and LISST-200X are commercial instruments made available in recent years, enabling underwater measurements of the volume scattering function, which has not been routinely measured *in situ* due to lack of instrumentation and difficulty of measurement. Bench-top and *in situ* measurements have enabled absolute calibration of the instruments and evaluation of instrument validity ranges, even at environmental extremes such as the clear waters at the North Pole and turbid glacial meltwaters. Key considerations for instrument validity ranges are ring detector noise levels and multiple scattering. In addition, Schlieren effects can be significant in stratified waters.

Published by The Optical Society under the terms of the [Creative Commons Attribution 4.0 License](https://creativecommons.org/licenses/by/4.0/). Further distribution of this work must maintain attribution to the author(s) and the published article's title, journal citation, and DOI.

1. Introduction

Changes in the ocean ecosystems due to anthropogenic climate change necessitates an increased level of environmental monitoring of the ocean. While ocean color data from remote sensing provide observations with extensive temporal and spatial coverage, it is often difficult to acquire accurate quantitative measurements of ocean constituents such as phytoplankton and colored dissolved organic matter (CDOM) in productive coastal regions [1,2]. Improvements in the ocean color products require enhanced measurements of the inherent optical properties (IOPs). These properties describe the influence of the water medium on light propagation, and are independent of the light field. These are measured *in situ*, typically with an active source and detector. Such optical *in situ* measurements can obtain high-resolution information about the vertical structure of the water column, which are unretrievable from satellite observations. While the spectral absorption and attenuation coefficients have been routinely measured for several years, direct measurements of scattering properties are more sparse. Unlike absorption, scattering also has a directional variability, quantitatively described by the volume scattering function (VSF). Due to lack of measurements, the VSF is often represented by simplified parameterisations, and scattering errors are corrected by empirical formulas. Thus, high-accuracy routine VSF measurements, which can be provided by the instruments LISST-VSF and LISST-200X, would be an important development within ocean optics research. This includes input for radiative transfer models, calculations of suspended particle properties [3,4], and corrections on other IOP measurements [5].

The volume scattering function (VSF or β , used interchangeably) is a fundamental IOP that represents the ability of a medium to scatter light in a certain direction. It is mathematically formulated as

$$\beta(\theta) = \frac{dI(\theta)}{E dV} [\text{m}^{-1} \text{sr}^{-1}], \quad (1)$$

where E is the irradiance of an incident unpolarized beam, dI is the radiant intensity of the scattered light from the volume element dV at an angle θ relative to the incident beam. Here, no azimuthal dependency is assumed, which is the case for media with randomly oriented scatterers. The more routinely measured scattering coefficient b can be calculated from the VSF using

$$b = 2\pi \int_0^\pi \beta(\theta) \sin \theta d\theta. \quad (2)$$

Moreover, the phase function $p(\theta)$, which is the normalized VSF, is defined by $p(\theta) = \beta(\theta)/b$. While the scattering coefficient may vary with several orders of magnitude depending on the ocean constituents in the respective water mass, and wavelength to a lesser degree, the phase function tends to depend less on ocean constituents and wavelength in natural waters. Hence, the phase function has often been subject to simplified models in radiative transfer modelling. Other related quantities are the backscattering coefficient b_b , given by

$$b_b = 2\pi \int_{\pi/2}^\pi \beta(\theta) \sin \theta d\theta, \quad (3)$$

and the asymmetry factor g ,

$$g = \langle \cos \theta \rangle = \frac{2\pi}{b} \int_0^\pi \beta(\theta) \cos \theta \sin \theta d\theta. \quad (4)$$

Due to the $\cos \theta$ -term, the asymmetry factor is more dependent on scattering in the far-forward and far-backward direction than the scattering and backscattering coefficients, which makes it challenging to measure accurately. It is often applied when assessing whether multiple scattering can be neglected or not.

The VSF of a medium containing randomly distributed spheres of uniform size and homogeneous structure was fully solved by Gustav Mie as a solution of Maxwell's equations [6]. For monodispersed spheres, only particle concentration, the size parameter (particle diameter relative to wavelength), and the relative complex refractive index decide the VSF. The solution becomes much more complex for non-spherical particles (see work of Mishchenko, e.g. [7]), and non-homogeneous optical properties. This makes forward modelling of the VSF in natural waters challenging, and the inverse problem even more so. Among others, the Fournier-Forand model [8] and Zhang et al. [9] utilize assumptions about particle size distributions and compositions to approximate the VSF.

While the refractive index influences scattering at all angles, the VSF depends strongly on the particle size distribution in the forward direction. Hence, the particle size distribution can be measured from small-angle scattering measurements using inversion methods. Known as laser diffraction, this technique forms the physical motivation behind a series of LISST-instruments (Laser *In Situ* Scattering and Transmissometry, produced by Sequoia Sci.), which are routinely used for sediment and oceanographic studies. The working principle is illustrated in Fig. 1. A laser beam of known power is transmitted through a sample chamber. The transmitted light is detected by a transmission detector, from which the attenuation coefficient can be calculated. The scattered light passes through a lens and onto a ring detector placed at the lens' focal length. Hence, all light scattered with a certain angle from the beam hits the same radius on the ring, and is detected by the silicon photodetector arcs covering logarithmically-spaced radii and consequently scattering angles. Agrawal [10] demonstrated how the scattering data from the LISST-100 ring detector could be used to compute the shape of the VSF, with the angular resolution covered by the ring detector arcs. Slade and Boss [11] used polystyrene beads to calibrate LISST-100 scattering data, yielding both the correct VSF shape and magnitude for angles 0.08-15°. Later, multiple studies have utilized LISST instruments for VSF measurements [12–15]. In [16–18],

the Schlieren effect on forward scattering and attenuation have been investigated. However, the LISST-200X, which is the most recent successor of LISST-100 and measures the VSF for angles 0.04-13° at 670 nm, has not previously been calibrated or used for VSF measurements to our knowledge.

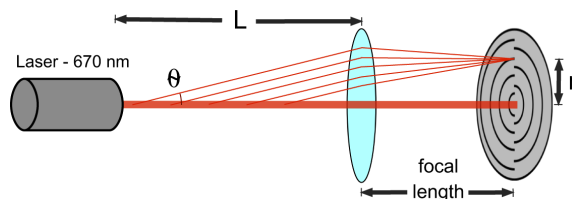


Fig. 1. The working principle of the ring detector used for LISST-200X. The detector plane is placed in the focal plane of a collimating lens, so that light scattered with angle θ will hit the detector plane at radius r . The LISST-VSF ring detector is similar, but with a 515 nm laser wavelength and a longer pathlength L .

The LISST-VSF is a recently released instrument measuring the VSF from 0.09° to 150°. Compared to the scattering and backscatter coefficients, as well as small-angle scattering, the large-angle VSF have been sparingly measured *in situ*. The primary reason is the technical difficulty of the measurements; due to the ratio of forward to backward scattered radiance there is a high demand on the dynamical range of the instrument. Tyler [19] and Petzold [20] were among the first attempts to measure the VSF, and the latter has emerged as the most widely cited set of VSF measurements. While the Petzold measurements are limited in geographical and environmental scope, they are of remarkable quality over a large angular range and are highly beneficial as benchmark figures. Modern studies have focused more on laboratory studies, but also includes some *in situ* measurements (see [21] for an overview). For the LISST-VSF, the dynamical range is covered by using the aforementioned ring detector up to 14.38°, and using a rotating eyeball detector at larger angles. The laser power is decreased when the eyeball position is between 15° and 40° to accommodate for the large differences in the scattering signal. In addition to the VSF, the eyeball detector also yields data allowing computation of Mueller matrix components M_{12} and M_{22} .

There is still a limited number of published studies with *in situ* or bench-top results from the LISST-VSF. Slade et al. [22] contains the first published results with the LISST-VSF, with bench-top measurements of polystyrene and size-fractionated Arizona Test Dust. Here, the degree of polarization was measured in addition to the VSF. The instrument has been shown to agree well with two other prototype VSF instruments, I-VSF and POLVSM [23]. However, due to unfortunate instrument damage, only the ring detector measurements were usable in this study. In the article by Koestner et al. [24], measurements with polystyrene beads of diameters in the sub-micrometer range were used to show that a correction function, $\beta_p^{\text{corr}}(\theta) = \text{CF}(\theta) \times \beta_p^{\text{meas}}(\theta)$, can be used to validate and correct LISST measurements with scattering predicted from Mie theory. Values of the correction function varied in the range 1.7-2.2 in this study. Moreover, laboratory measurements were done on natural seawater samples from different marine environments around the Southern California coast. In addition, the degree of linear polarization was also thoroughly investigated in a similar fashion, showing the further potential of LISST-VSF measurements. This work was very recently expanded upon in [25], where relationships between the measured Mueller matrix components and marine particle properties were investigated. The LISST-VSF has also been used in some optical communication studies (e.g. [26,27]), and in Sahoo et al. [28], where measurements were done *in situ* at discrete depths in the Bay of Bengal.

While earlier studies have used the default relative calibration, Hu et al. [29] offered a significant improvement with the implementation of an absolute calibration of the eyeball detector (see section below for details). This decouples the two detector measurements and enables VSF measurements in very clear waters, which was utilized in a study where the VSF fraction of particles smaller than 0.2 and 0.7 μm in clear ocean waters was measured, in bench-top mode by filtering water during a research cruise in the North Pacific Ocean [30].

In this work, we similarly present results from both submerged polystyrene and polymethacrylate beads and natural waters using the LISST-200X and LISST-VSF. Our approach to absolute calibration utilize larger beads and has a larger concentration range than most earlier studies, which to a greater extent indicates the validity ranges of the instruments. Polarization measurements with the LISST-VSF, the Mueller matrix components M_{12} and M_{22} , have not been included in the study for brevity. The focus of the natural water measurements has been *in situ* data collection using profiling deployment. Fieldwork has been conducted in highly diverse environments, such as the Arctic Ocean and coastal waters of the Svalbard archipelago during the INTAROS-2018 and CAATEX-2019 cruises, and in various coastal waters in southwestern Norway. We evaluate the need for temperature and salinity corrections, compare the validity ranges of the two instruments, and assess the effect of Schlieren on measurements in stratified waters. Finally, we look into extrapolation of forward scattering to estimate the scattering coefficient, which could be another useful application for the LISST-200X in turbid waters.

2. Methodology

2.1. Laboratory calibration measurements

Spherical beads with microscopic, low-variance diameters, made by polystyrene or polymethacrylate, made it possible to perform absolute calibration or validation of scattering measurements. Knowing the bead size distribution, relative refractive index and concentration, Mie theory can be used to calculate the exact VSF of the plastic beads submerged in pure water. Consequently, measurements from the LISST instruments may be compared with accurate theoretical values. For the relative complex refractive index of polystyrene beads, we used values found in [31]. For polymethacrylate (PMMA) beads, values from [32] were used. Theoretical scattering was calculated using Gaussian particle size distributions with the specified size variations. Each VSF was converted to instrument-specific angular resolutions by finding the mean value within each angular bin, which corresponds to the assumption made by the instrument data processing. For transmission values within the instrument range, the VSF measurements have been corrected for volume concentration errors by re-scaling using the ratio of measured and theoretical attenuation, similar to the method used in [11] and [24],

$$\beta_{\text{corr}}(\theta) = \frac{c_{\text{Mie}}}{c_{\text{meas}}} \beta_{\text{meas}}(\theta). \quad (5)$$

The motivation for doing bench-top measurements using beads are different for each of the studied sensors. The LISST-VSF ring detectors have already been factory-calibrated for VSF measurements, so validation is the primary goal. The LISST-200X has not been directly calibrated for VSF measurements, meaning that absolute calibration is necessary. For the LISST-VSF eyeball detector, the current default data processing uses a relative calibration to calculate the VSF, where the VSF measured from two outer-most ring detectors (angles 12.32° and 14.38°) are extrapolated to the first angle of the eyeball detector (15°). The ratio of the extrapolated value and the uncalibrated eyeball detector value $P_{11}^{\text{uncal}}(15)$ is subsequently used as a scaling factor for calculating the VSF from $P_{11}^{\text{uncal}}(\theta)$. This method is highly sensitive to uncertainties in the ring scattering data.

In addition, bead measurements spanning over a large concentration range allow an assessment of the validity of the VSF measurements; when does the linear relationship between particle

concentration and VSF, or attenuation, break down? The topic of instrument validity ranges with respect to particle size and concentration is further discussed in section 3.1.1.

2.1.1. Overview of data processing

The VSF is computed from scattering data output of the LISST instruments, digital counts, using factory-provided data processing procedures outlined here. The ring detector data processing has been treated in detail in [3,10]. The raw signal, denoted *scat*, is digital counts, from which ambient light has been rejected. This is corrected for instrumental artifacts using

$$\text{cscat} = \text{scat}/\tau - \text{zscat}. \quad (6)$$

Here, *zscat* are background scattering measurements made in pure water to account for intrinsic pure water scattering and optical losses in the instrument. By contrast to *zscat* and *scat*, the corrected scattering signal *cscat* is no longer an integer due to the division on τ . The transmission ratio is $\tau = T/T_0$, where *T* is the measured transmission (measured laser power $I_{\text{out}}/I_{\text{incident}}$) and T_0 is the measured transmission from the background measurement. LISST-200X *cscat* values are also divided by a concentration calibration factor (for particle size distribution calculations), yielding many orders of magnitude smaller values than LISST-VSF *cscat* values. This has no impact on VSF measurements. For the LISST-VSF eyeball detector, the transmission must be calculated from the attenuation *c*, $\tau = \exp(-cL)$, as the pathlength *L* of the detected light beam varies with the eyeball angle.

The ring *cscat* data is subsequently converted to the VSF using the expression

$$\beta_{i,p}(\theta) = \frac{P_{i,p}}{P_0} \cdot \frac{C_i}{2\pi\phi(\cos\theta_{i+1} - \cos\theta_i)L}, \quad (7)$$

where $P_{i,p}$ is the *cscat* scattering data on ring *i* counted from the centre, P_0 is the incident light, θ_i and θ_{i+1} is the inner and outer radius of each ring detector, and $\phi = 1/6$ denotes that each detector only covers 1/6 of a circle. Furthermore, C_i represents constants for geometrical corrections such as vignetting. In addition, the sensitivity of the detectors needs to have correct values. The eyeball scattering data follow another processing procedure; four components of scattering data have been measured using combinations of source and detector polarizations. Each of these components are first corrected for ambient light by rapidly turning the laser on and off and subtracting the measured ambient light. Then the components are corrected for differences in transmission due to use of a half-wave plate, before the components are corrected for attenuation-loss and laser drift, and the background measurements (matched with the PMT-gain) are subtracted. At around 45°, there is a change in laser power. This is corrected for using a factory-provided calibration factor, and interpolating the data between 44° and 51°. Moreover, a geometric correction is applied for a small misalignment between laser and eyeball viewing plane, as well as a relative gain correction for differences between the laser polarizations (we used the automatic α -value). Finally, the components are used to compute the VSF and additional polarization components. The VSF is computed by first taking the average of the four corrected components, yielding $P_{11}^{\text{uncal}}(\theta)$, which is then scaled using the absolute or relative calibration. We refer to [24,25,29] for further details on the eyeball detector.

2.1.2. Experiment procedure

Each laboratory experiment started with filling the factory-provided sample chambers of the instruments with ultrapure water (Milli-Q). In order to minimize uncertainties in the bead concentrations, care was taken to add an accurate amount of water: 18 mL for the LISST-200X and 1620 mL for the LISST-VSF sample chamber. After adding ultrapure water, at least one hour was allowed for bubbles and possible temperature differences to dissipate, before blank

measurements were made. For the LISST-VSF, the sample chamber mixers always had to be used when measuring, in order to get non-fluctuating transmission values. Solutions of polystyrene or PMMA beads were then added to the sample chamber using pipettes (Eppendorf Research Plus), so that the bead concentration could be known with a high degree of certainty. For each experiment, a cumulative amount of the bead solution was added, yielding a measurement series of increasing bead concentration. For each bead concentration, approximately 100 single measurements were done with both instruments.

2.1.3. LISST-VSF eyeball detector calibration

Polystyrene beads (0.190 μm (Sigma-Aldrich); 0.508 and 25.1 μm (Thermo Fischer Scientific)) in different concentrations were used for the absolute calibration of the LISST-VSF eyeball detector. Following [29], the absolute calibration was implemented with the equation

$$\beta^{\text{eyeball}}(\theta) = \kappa(\theta, V_0) \left(\frac{V_0}{V} \right)^\gamma P_{11}^{\text{uncal}}(\theta, V). \quad (8)$$

Here, V is the PMT voltage of the respective measurement and V_0 is a reference voltage (selected to be 645 mV in both this and the aforementioned study). The term $(V_0/V)^\gamma$ is a conversion factor, yielding a linear relationship between $\beta^{\text{eyeball}}(\theta)$ and $P_{11}^{\text{uncal}}(\theta, V)$ irrespective of PMT voltage. The coefficient γ depends on dynode material and geometry; the value used in the Hu et al. [29] study, $\gamma = 8.6$, was also in excellent agreement with our data. Finally, $\kappa(\theta, V_0)$ is the calibration coefficient, which can be calculated from bead measurements and theoretical VSF values using linear regression of Eq. (8).

2.1.4. Ring detector calibration

The LISST-VSF ring detector has been evaluated using polystyrene beads (0.508, 2.504 and 25.1 μm (Thermo Fischer Scientific)) and PMMA beads (4.92 μm (Sigma-Aldrich)) in different concentrations. We used different angular domains for each type of bead, due to factors described in section 3.1.1. As mentioned above, Koestner et al. [24] introduces a correction function CF, based on bead measurements, which is applied to correct already processed VSF measurements β^{meas} . A linear relationship is assumed between the measured and true VSF, so that $\beta^{\text{corr}} = \text{CF} \times \beta^{\text{meas}}$. CF was calculated by finding the median of $\beta^{\text{true}}/\beta^{\text{meas}}$ for each angle, where β^{true} is the theoretical VSF (this is subsequently referred to as method 1). We use a standard least-squares fitting of the measured data to the theoretical values to compute the correction function (method 2),

$$\beta^{\text{true}} = A\beta^{\text{meas}}, \quad (9)$$

and compare with the method stated in [24]. Finally, we also compare with the linear model

$$\beta^{\text{true}} = a\beta^{\text{meas}} + b, \quad (10)$$

to check for possible "zero scattering" offsets in the measured data (method 3).

The LISST-200X was calibrated in a similar way. As the laser power per digital count is not known for the incident laser detector, the default output has the wrong magnitude. Different concentrations of polystyrene beads (2.504 and 25.1 μm (Thermo Fischer Scientific)) and PMMA beads (99.0 μm (Sigma-Aldrich)) were used. The 99 μm beads were challenging to keep suspended; persistent mixing using a pipette made it possible to measure in the small LISST-200X sample chamber, but not with the LISST-VSF.

2.2. Fieldwork

2.2.1. In situ measurements

During the field deployments, the LISST instrument measurements were conducted by continuous profiling down to a depth of 50 m, which is the factory-specified maximum operational depth

of the LISST-VSF. After initial tests, continuous profiling was found to be the prudent choice, as stationary measurements gave highly fluctuating transmission values. This is consistent with bench-top measurements; even when the water is ultrapure, static water is detrimental for transmission measurements. We speculate that this is due to microturbulence along the beam caused by the laser, but mirror-like reflections by large slow-moving particles could also have a contribution. This is not seen for the LISST-200X, but continuous profiling is also used here for consistency. Continuous profiling also puts some constraints on the measurements. The winch system operated with an ascent and descent speed of approximately 0.5 m/s. For the LISST-200X, which has a sample rate of 1 Hz, each sample will then cover 0.5 m. With LISST-VSF, each sample takes 4 seconds. Thus, one sample will cover 2 meters. Moreover, the LISST-VSF acquires data by first doing an eyeball and ring detector measurement with perpendicular polarized incident light, then another with parallel polarized incident light. This means that the Mueller matrix components can only be reliably measured using continuous profiling in a uniform or slowly changing water column. However, the VSF is calculated from a simple average of the different light measurements. To assure high data quality of the LISST-VSF, multiple casts were always made, typically from three in regular waters to seven in very clear waters. The subsequent data processing include depth-binning the measurements and calculating the median VSF. Physical oceanographic quantities have been obtained using the Castaway-CTD or Rockland Scientific VMP-250 vertical profiler.

2.2.2. Locations

In situ measurements were conducted during three field campaigns, as well as four different days at the Espegrend Marine Biology Lab in Raunefjorden outside Bergen, Norway (in April 2018, June 2018, June 2019 and November 2019), see Fig. 2 for an overview. During the INTAROS-2018 cruise with the Norwegian coastguard vessel KV Svalbard in the Arctic Ocean north of Svalbard, a total of 9 measurement stations were done. Five stations were conducted around in the region around ice edge as well as in ice leads and under ice floes. The last four stations were made in coastal waters of the Svalbard archipelago, for instance in Rjippfjorden, a fjord on northeastern Svalbard with a large glacier calving into the fjord. More measurements were performed in the central Arctic during the CAATEX-2019 cruise in August-September 2019, also with KV Svalbard. Station 1 of this cruise was conducted at the North Pole, and the proceeding stations were made in the ice-covered ocean south towards Svalbard. Finally, further measurements on glacial meltwater in Norwegian coastal waters were conducted in Gaupnefjorden in June 2019, a fjord arm of Sognefjorden in Western Norway. In total, 25 measurement stations are included in this study, with a significant span in optical characteristics as well as geographical extent.

2.2.3. *In situ* temperature and salinity corrections

In clear waters, the scattering of the water itself may have a significant contribution to the total measured scattering at large angles [30]. Using a blank measurement will remove the scattering at the temperature and salinity of the pure water used. However, the temperature and salinity will almost never be the same *in situ* as the blank, making a temperature and salinity correction necessary. In a previous study, this is addressed by not using a blank for field measurements, but simply subtracting the pure water scattering directly [29]. This assumes no optical losses by the instrument, which may be negligible for new instruments but not after extensive use and time, e.g. increased transmission loss in the optical windows. Thus, we suggest another approach. The measured VSF (β_m) may be assumed to be the sum of particulate scattering β_p , pure water scattering β_w and optical losses β_L ,

$$\beta_m = \beta_p + \beta_w(T, S) + \beta_L. \quad (11)$$

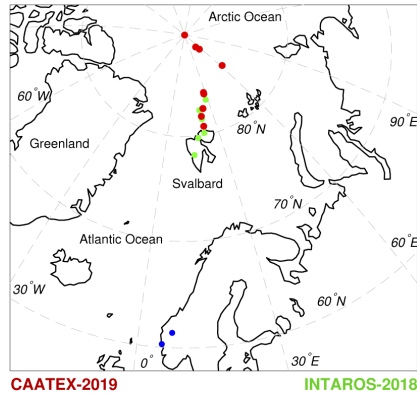


Fig. 2. Map showing the locations of the fieldwork conducted in this study. During the INTAROS-2018 cruise (in green) nine stations were conducted. Nine stations were also done during the CAATEX-2019 cruise (in red). Locations of additional fieldwork in Norwegian fjords are shown in blue.

We have not investigated polarization dependencies of the optical loss, but as the scattered light enters the optical window perpendicular (or near-perpendicular) to the window surface, we do not expect major polarized components. For blank measurements, particulate scattering is assumed to be zero, yielding the expression for the measured blank VSF,

$$\beta_{BG} = \beta_w(T_{BG}, 0) + \beta_L. \quad (12)$$

Since the optical loss term is the same in both instances, one can solve for the particulate scattering,

$$\beta_p = \beta_m - \beta_{BG} - \beta_w(T, S) + \beta_w(T_{BG}, 0). \quad (13)$$

Here, the term $\beta_m - \beta_{BG}$ is the output of the default data processing. The pure water scattering is calculated as described in [33] and [34]. The temperature and salinity from field work are interpolated from CTD measurements.

3. Results and discussion

3.1. Laboratory measurements

3.1.1. Validity ranges for LISST measurements

The validity range of the LISST instruments is limited by the range of the detectors, as well as the assumption that all scattered light is only scattered once (single-scattering condition). The instrumental validity ranges are also evident from the bead calibration measurements. To get stable and consistent measurements for calibration use, the VSF must vary slowly due to possible smearing effects, the oscillations characteristic for beads must be absent or smoothed out. Small beads (for instance $0.190 \mu\text{m}$ diameter) fit this requirement well, but the LISST instruments are optimized for natural waters, which have implications for the lower signal limit of the ring detectors. In Fig. 3(a), it can be seen that when $\text{cscat-values} < 10^{-4}$, LISST-200X VSF measurements only have a weak relationship with theoretical VSF values compared to above this threshold. For reference, cscat values from field measurements are typically in the range 10^{-5} to 10^{-2} . For LISST-VSF, the same is seen for $\text{cscat-values} < 10^2$ in Fig. 3(b) (LISST-VSF

cscat values are typically between 10^2 and 10^5 in field measurements). This pattern is seen for all ring detectors for similar cscat values. Given that the scattering data are related to the VSF through Eq. (7), the minimum VSF values will vary with angle. Field scattering data within these orders of magnitude should be treated with care. Within the low particle concentration limit, the transmission reaches the upper detection limit (which is given as 0.98 for LISST-VSF and 0.995 for LISST-200X). The transmission errors have a relatively low impact on scattering data in clear waters, as seen from Eq. (6).

Within the high particle concentration limit, the transmission lower limit has a large impact. Following Eq. (6), the scattering data are highly sensitive for errors in the transmission measurements when the transmission is low. However, multiple scattering is a more likely limiting factor for VSF measurements in turbid waters. Re-scattered light enters the detectors in addition to the single-scattered light, leading to an overestimation of the VSF. The single-scattering condition is commonly given as $\tau^* \ll 1$, where $\tau^* = cL(1-g)$ is the scaled optical depth (L is the pathlength, c is attenuation), not to be confused with the transmission ratio τ . The appearance of the asymmetry parameter g shows that for waters with smaller angular differences in the VSF, the single-scattering condition will be violated at lower concentrations than in waters with a dominant forward scattering component. When planning the measurements, we used $\tau^* \leq 0.1$ as a default condition.

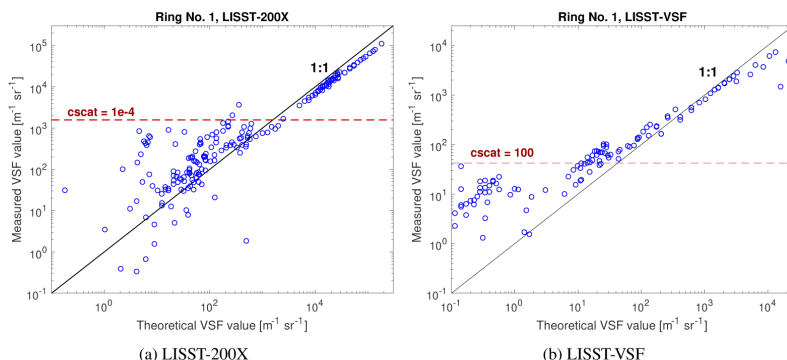


Fig. 3. The VSF of polystyrene or PMMA beads, measured with the innermost ring detector on both instruments and compared with the theoretical values computed using Mie theory. Under a certain threshold in the scattering data (cscat), there is a loss of linearity between measured and predicted values. Due to the area of the rings, this problem is most prevalent for the innermost rings, and dissipates at larger angles, where the size of the detector is larger.

The expected range of possible bead concentrations due to some of the aforementioned factors are visualized in Fig. 4. Here, Mie calculations have been applied to polystyrene beads of diameters 0.1-200 μm , and for the wavelengths of both LISST instruments. There is a scattering maximum for particle diameters approximately twice the wavelength, leading to a minimum of the detectable volume concentration. For smaller particles in the Rayleigh limit, the range of valid volume concentration becomes smaller. Large particles can have much higher volume concentrations without violating the single-scattering condition, and lower concentrations to get strong signals for the ring detector. However, large beads are limited by oscillations for larger angles. Measurements at these angles were excluded in the calibrations. Thus, for calibrating

LISST instruments at all angles, it is necessary to include measurements with both smaller and larger beads.

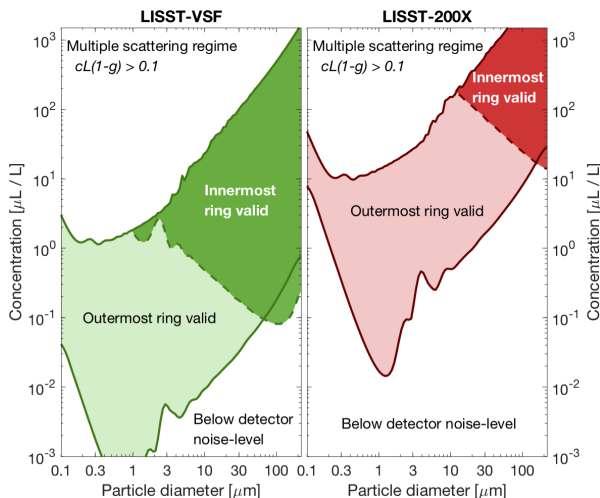


Fig. 4. Expected concentration range for valid measurements calculated for mono-dispersed polystyrene beads, varying in size and diameter. Red area shows the valid area for LISST-200X (wavelength 670 nm) and green area for LISST-VSF (wavelength 515 nm). The strongly colored areas indicate the concentration range needed to get valid measurements for the innermost rings, while the weakly colored areas indicate concentrations for valid signal from the outermost rings. The areas are overlapping, except in a small region with low concentrations of large beads. Here, scattering is so forward-peaked that there is a valid signal for the inner ring but not the outer ring. It should be noted that these results do not extend to particle size distributions.

In this study, we have used six bead diameters covering different angular domains. When calibrating the LISST-VSF, 0.190 μm beads were used for angles above 15° , and 0.508 μm beads above 5.5° . Furthermore, 2.504 μm beads were used for angles below 4.7° and 3.92 μm beads below 2.1° (both with limited signal under $\sim 0.3^\circ$). Finally, 25.1 μm beads were used in the angular domains $0.09^\circ - 0.75^\circ$ and $4.7^\circ - 14.4^\circ$. For the LISST-200X, 2.504 μm beads were used for angles below 10° (with limited signal under 0.1°), and 25.1 μm beads were used in the angular domains $0.07^\circ - 1^\circ$ and $3.5^\circ - 13^\circ$. In addition, 99 μm beads were of particular importance to get data for the innermost rings, covering the angular domains $0.04^\circ - 0.2^\circ$ and $2.5^\circ - 13^\circ$.

3.1.2. Bead attenuation measurements

The results of the attenuation measurements are shown in Fig. 5(a) and 5(b). The measurements show overall high agreement with the theoretical values when transmission values are higher than 98 %. For lower attenuation values, the measurements become imprecise. Some measurements with the LISST-200X have high variability also for higher attenuation. The 99 μm beads used were difficult to sufficiently mix for avoiding settling. Other deviations may be explained by uncertainties in the volume concentration. Comparing the two instruments, the results support the notion that LISST-VSF is suited for attenuation measurements in all but extremely clear natural waters ($c > 0.13 \text{ m}^{-1}$), while the LISST-200X is more limited ($c > 0.8 \text{ m}^{-1}$). The upper

limit of neither instrument has been reached, the LISST-VSF results show good accuracy up to $\sim 30 \text{ m}^{-1}$, above the specified limit.

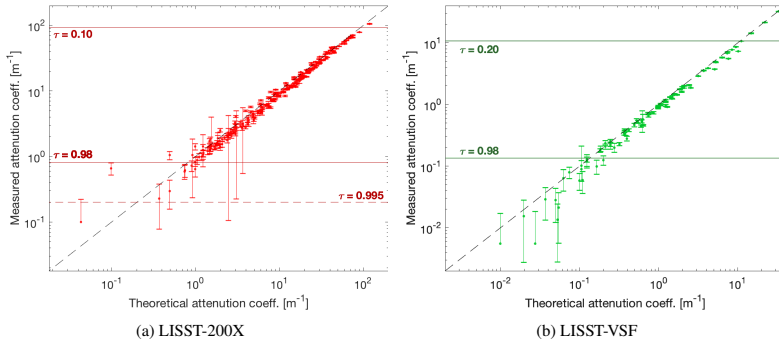


Fig. 5. Attenuation measurements with the LISST-200X and LISST-VSF using plastic beads; comparison between theoretical values from Mie theory and measured values. Error bars indicate the standard deviations in each measurement, consisting typically of around 100 samples. The factory-specified limits for valid transmittance measurements $\tau = \exp(-cL)$ are also plotted.

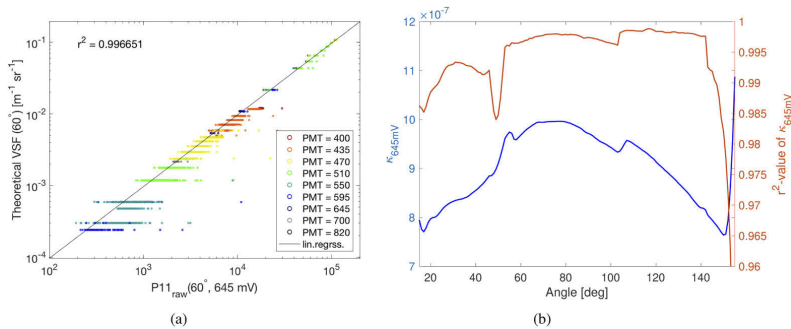


Fig. 6. The absolute correction for the eyeball detector is found by linear regression of $P_{11}^{\text{uncal}}(\theta, 645 \text{ mV})$ -values and theoretical VSF-values for each measured angle. In (a), uncalibrated LISST-VSF eyeball detector data $P_{11}^{\text{uncal}}(\theta, 645 \text{ mV})$ (converted to PMT = 645 mV, see Eq. (8)) are compared with corresponding theoretical VSF values for $\theta = 60^\circ$. Different colors differentiate the PMT values. The linear regression yielding the κ -value is also plotted. In (b), the absolute calibration factor κ is plotted over the entire angular domain of the LISST-VSF eyeball detector output (blue line). The coefficient of determination (r^2 -value) is also shown for each angle.

3.1.3. LISST-VSF eyeball detector calibration

The PMT correction of the LISST-VSF was made with 0.190, 0.508 and 25.1 μm polystyrene beads over a large concentration range. Similar to the Hu et al. study [29], a strong linear relationship between the $P_{11}^{\text{uncal}}(\theta, 645\text{mV})$ and $\beta^{\text{eyeball}}(\theta)$ can be seen in Fig. 6(a) and 6(b). However, the κ -value is three orders of magnitude smaller for our instrument (SN = 1667), likely because the aforementioned study normalized the P_{11}^{uncal} by dividing on incident laser power (which could mitigate effects of laser drift). For low 25.1 μm bead concentrations, which give the lowest VSF values in Fig. 6(a), there is significant variation in the data, possibly due to a relatively low PMT gain compared to the signal. Lack of rescaling (see Eq. (5)), due to attenuation values outside instrument range, may cause additional uncertainties. It should also be noted that comparing goodness-of-fit across the entire angular domain with statistical quantities (r^2 or mean square error) should be treated with care, due to large variations in the dynamical range of the measurements, but manual inspection of the data confirms good agreement.

3.1.4. LISST-VSF ring detector validation

Measurements of plastic beads up to 25.1 μm were used to calculate correction functions for the LISST-VSF ring detector. The results are shown in Fig. 7. Near-unity correction functions and r^2 -values for all methods would indicate a perfect fit between theory and measurements. Figure 7(a) and 7(b) reveal that the ring detector measurements generally agree well with the expected theoretical values for all three methods used. The linearity of the data is illustrated in Fig. 9(a). The correction function found using the median of the ratio (method 1) deviates from the linear regression functions (method 2 and 3) at some angles. The reason seems to be that it is more influenced by where in the scattering range the majority of the measurements have been made. There are no significant differences between the perpendicular (Fig. 7) and parallel (not shown) polarized incident light, as expected for forward scattering. Measurements from the ring detector at 0.90° were highly erratic and non-physical, also in blank measurements. Results from this ring have thus been consistently treated as invalid and replaced by interpolated values using the two neighbor rings, even though this may introduce a small bias.

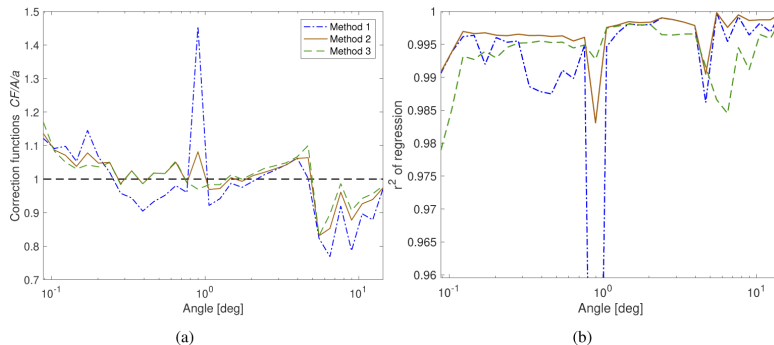


Fig. 7. Correction functions for the LISST-VSF ring detector, for the perpendicular incident beam (first rotation, in the vertical plane of the instrument), is shown in (a). Each method is described in section 2.1.4. The coefficient of determination (r^2 -value) for each method is shown in (b).

Significantly higher forward scattering than expected from Mie theory were measured for sub-micron beads. The forward scattering varied between measurement series and was observed

to increase with time. We speculate that this is due to flocculation of small beads, as it has been shown that particle flocculations may appear as larger particles in LISST particle size distribution measurements [35], which is consistent with higher forward scattering. Other studies have used an ultrasonic device to break up the flocs [11,23], which would likely eliminate this error source. Moreover, smaller beads scatters so little in the forward direction that the ring detector scattering data are under the instrument detection level. Data affected by these error sources were discarded. Multiple scattering influences the measurements, which is seen as a non-linear relationship between bead concentration and VSF. This is plotted for 25.1 μm beads in Fig. 10(a). The single-scattering condition has been used as a guideline ($\tau * < 0.1$), but results shown in Fig. 10 indicate that it may not be an adequate condition for calibration purposes, especially for larger beads such as 25 μm at large angles. Thus, some empirical considerations had to be made for the calibration concentration range. Slade and Boss [11] points out the imaginary refractive index of the bead material as a major error source for VSF measurements of larger beads, but based on Fig. 10 we believe multiple scattering plays a more significant role than expected.

Variations between different particle samples and their dilutions seem to be the largest source of uncertainty. The impact has been mitigated by doing multiple independent measurement series with varying particle diameter and applying the attenuation re-scaling. Nevertheless, it is reasonable to conclude that the deviations may be attributed to the experimental uncertainties, and that the LISST-VSF ring detector is adequately calibrated from the factory.

3.1.5. LISST-200X ring detector calibration

While the VSF is a default output of the factory data processing for the LISST-VSF, the LISST-200X data processing does not yield the VSF by default. However, Sequoia Sci. provided a data processing script enabling non-calibrated VSF measurements as output. Here, the correction functions were used directly for absolute calibration of the measurements. Results shown in Fig. 8 reveal similarities with the LISST-VSF ring detector, including most of the error sources. Figure 9(b) shows an example of robust fit of the data at 0.66° . The correction factors vary between 1.6×10^{11} and 3.6×10^{11} . Method 1 deviates slightly from the two linear regression-methods (method 2 and 3), but follows same the general trend. In Fig. 10(b), one may also for LISST-200X observe a non-linear relationship between attenuation and measured scattering at large angles for 25 μm beads. In addition, there were some saturation errors in the ring detector data. These measurements had to be manually removed. Following the same considerations as for the LISST-VSF, a constant value, $A = 2.8 \times 10^{11}$, was chosen for all rings.

3.2. Field measurements

3.2.1. Assessment of PMT calibration

In situ field measurements with particulate scattering covering several orders of magnitude enable robust comparisons between the absolute and relative PMT calibration as well as between the two LISST instruments. A natural point of comparison for the relative and absolute calibration is the VSF at 15° , the start of the eyeball measurement, plotted in Fig. 11. The two methods agree well for mid-range scattering, while discrepancies are apparent in very clear and turbid waters. For clear waters, systematic discrepancies may be seen for PMT-values 435-550. These measurements are from the INTAROS-2018 cruise, where the automatic PMT gain adjustment seemed to insufficiently adjust to very clear waters, yielding noisy eyeball data. After the cruise, the PMT-gain algorithm was updated by the producer, yielding significantly better results for later fieldwork. The absolute calibration was performed after this update. While the PMT gain may be set manually, the automatic gain is typically necessary due to water column variations. Moreover, for the CAATEX-2019 cruise, unreliable values in the outermost ring yielded artificially low eyeball values for the relative calibration, perfectly illustrating the uncertainty of this method. The relative calibration is also visibly affected by random errors in the forward scattering in

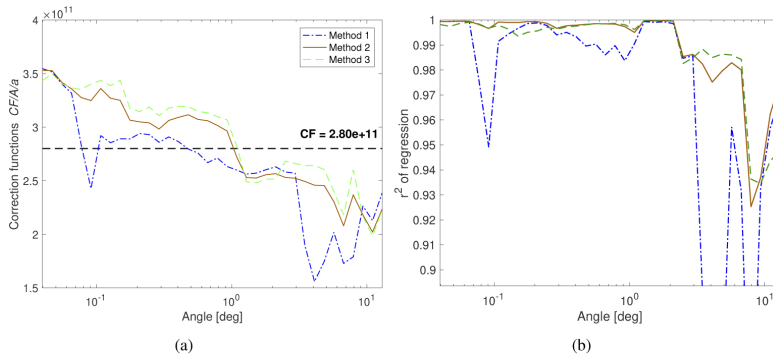


Fig. 8. Correction functions for LISST-200X ring detector is shown in (a). Each method is described in section 2.1.4. The coefficient of determination (r^2 -value) for each method is shown in (b).

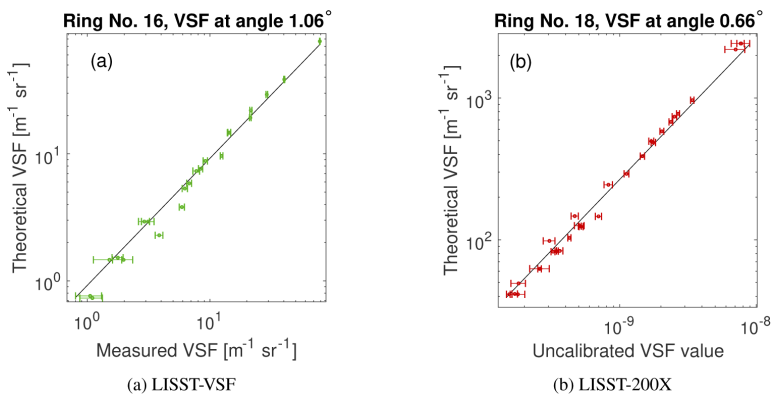


Fig. 9. Measured VSF from ring 16 of the LISST-VSF ring detector (total ring number is 32), is compared with theoretically predicted VSF values in (a). The standard deviation of the measurements are plotted as error bars. A robust linear fit (method 2) is also plotted as a black line. In (b), uncalibrated VSF values from the LISST-200X are plotted with corresponding theoretical VSF values, along with the robust fit (method 2, showing ring number 18 out of 36).

addition to the systematic errors in clear waters. In turbid waters, a discontinuity is visible in the VSF between the ring and eyeball detector, at 15° when the absolute calibration is used (see Fig. 14). This is due to multiple scattering effects, as the two detectors have different pathlengths at 15° . The eyeball detector may also experience saturation in particularly turbid media.

The scattering coefficient, backscattering coefficient and backscattering fraction for the two calibrations are compared in Fig. 12(a) and 12(b). All are integrated from bin-median VSF, with extrapolation in the backward direction by using a well-established backscattering model [9]. For *b*, the differences are minimal, due to the dominating contribution of forward scattering to

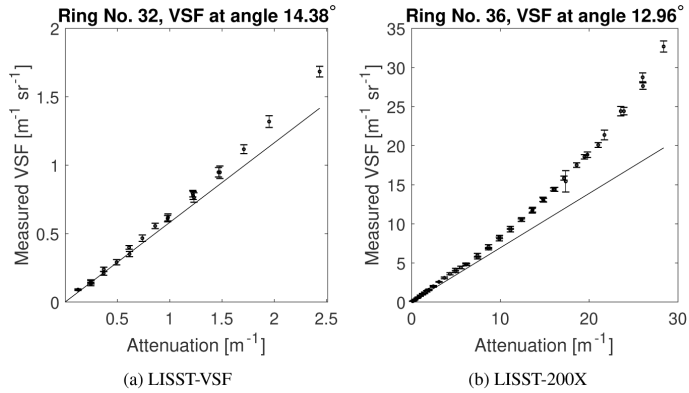


Fig. 10. VSF measurements with $25.1 \mu\text{m}$ beads are plotted as a function of the attenuation, for the outermost ring of LISST-VSF (a) and LISST-200X (b). Theoretically predicted scattering is plotted as a black line. Maximum scaled optical depth for the LISST-VSF results is $cL(1-g) \sim 0.02$, for LISST-200X the maximum value is $cL(1-g) \sim 0.05$. Non-linear behaviour can be seen for a large range of concentrations. In the innermost rings the non-linear behaviour is absent (not plotted).

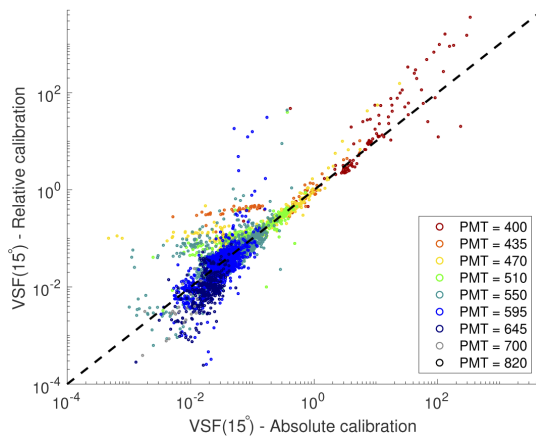


Fig. 11. Comparison of LISST-VSF measurements at 15° , using relative (default calibration) and absolute calibration. Each color represents a different PMT value used in the calibration. As the PMT values may change throughout a profile, each measurement is plotted. While most measurements are close to the 1:1 line, there are differences in turbid and very clear waters.

the scattering coefficient. By contrast, b_b shows more discrepancies, especially the effects of multiple scattering are apparent.

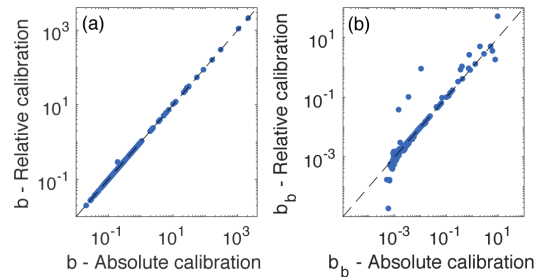


Fig. 12. Comparison of the particulate scattering coefficient b (a), the particulate backscattering coefficient b_b (b), when using the relative and absolute calibration.

3.2.2. Temperature and salinity corrections

In Fig. 13, absolute calibrated LISST-VSF measurements are plotted with the offset due to pure water scattering, computed from temperature and salinity interpolated from CTD measurements. It is clear that a temperature and salinity correction is important for clear waters, but it gives a negligible contribution at small angles or in turbid waters. LISST-200X has a measurement domain which does not reflect a need for a temperature and salinity correction of the VSF. The importance of auxiliary CTD casts is evident in almost all investigated waters, as changes in both optical and physical quantities are often significant in the upper water column. Natural waters with high salinity and low temperatures have the highest pure water scattering, with the salinity making the strongest contribution. Most physical and empirical models that are used in the computation of pure water scattering, have a validity range down to 0 °C. In polar surface waters, the water temperature can be lower than -1.5 °C. Few studies have investigated optical properties at such temperatures. A theoretical model for volume scattering function by pure seawater was recently extended to subzero temperatures by [36]. For *in situ* measurements, one also need to consider possible offsets in light attenuation and the refractive index [37]. In particular, changes in the latter leads to a different transmittance at the interface between water and optical windows. Estimates show that these effects combined can give an absolute error in the attenuation up to $\sim 0.01 \text{ m}^{-1}$ for LISST-VSF, and $\sim 0.05 \text{ m}^{-1}$ for LISST-200X. VSF measurements are less affected, with relative errors on the order of $\sim 10^{-3}$. Controlled validation measurements at subzero temperatures and high salinity are needed for more accurate error estimates, instrument-specific corrections, and validation of the theoretical scattering model.

3.2.3. Volume scattering function measurements

A selection of particulate VSF measurements in different natural waters is shown in Fig. 14. The values are calculated from the median of all valid data within a given depth-interval (with low variability) at each measurement site. The clearest waters measured in the central Arctic had minimum VSF values of $\sim 10^{-5}$, with considerable noise even after averaging 138 samples. Only slightly higher scattering, seen at the North Pole station, gives a much less noisy signal. On the upper turbidity limit is glacial meltwater. Here, the measured VSF around 90° is more than five orders of magnitude larger than in the clearest measurements. However, the aforementioned discontinuity between the detectors can be seen at 15°, revealing multiple scattering effects and

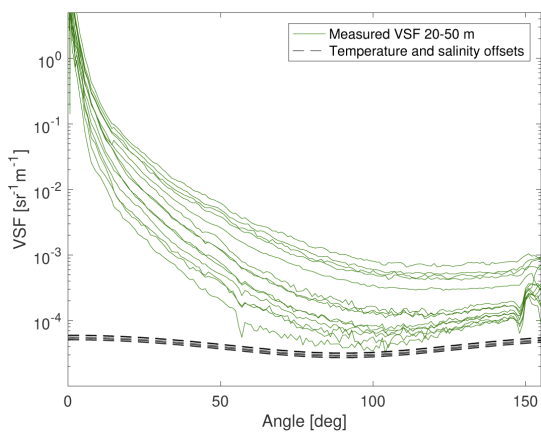


Fig. 13. LISST-VSF measurements from a large selection of field measurements (median between 20 and 50 meters), are plotted in green, before correction of temperature and salinity. The temperature and salinity correction offset for each VSF measurement, computed from theoretical pure water scattering [33], is plotted as black dashed lines. Thus, the lines form a band of typical VSF offsets in natural sea water.

suggesting that the detected VSF magnitude may be incorrect. Variations in the phase function are also evident.

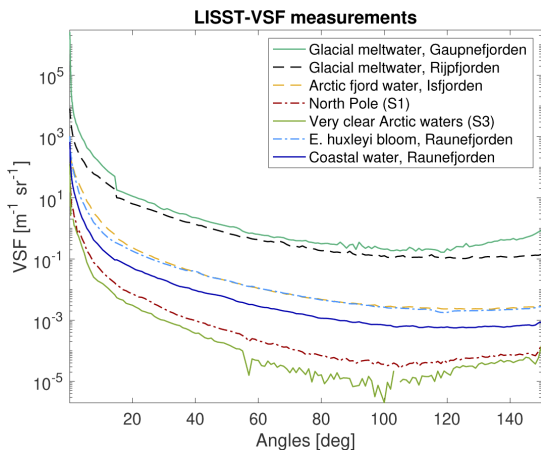


Fig. 14. A selection of *in situ* particulate VSF measurements with the LISST-VSF in highly varying natural waters, from the Norwegian coast to the North Pole. The extremities of the instrument validity range can be observed.

In some of the LISST-VSF measurements, a dip can be seen around 120° in the uppermost 10-20 meters. This is most likely because the field-of-view of the eyeball detector moves from

being directed at the open environment to being directed at the instrument wall at $\sim 120^\circ$, leading to an artifact in the ambient light rejection. For angles above $145\text{--}150^\circ$, elevated VSF values can also be frequently observed (see Fig. 13), both for laboratory and field measurements. The cause is probably instrumental reflections, but backscattering from bubbles could also have an additional contribution.

In Fig. 15, VSF measurements of the LISST-VSF and LISST-200X are compared for three cases. In the lowermost VSF (dashed line), large parts of the LISST-200X falls under the noise level indicated with a solid black line (chosen as $\text{cscat} = 5 \times 10^{-5}$). The LISST-200X frequently measures scattering under the lower detection level in clear waters, resulting in an unreliable and limited VSF. For the middle case (dashed-dotted line), both instruments perform well. Here, the shape of the VSF agree well, and there is a reasonable increase in scattering from 670 to 515 nm. However, for turbid waters (solid line), the LISST-VSF measures VSF values $\sim 25\text{--}500$ times higher than corresponding LISST-200X values. These severely elevated measurements are due to multiple scattering. Moreover, the flattening of the LISST-VSF phase function close to zero has been shown to be due to saturated ring detectors. The LISST-200X is with the 2.5 cm pathlength much less influenced by the mentioned effects.

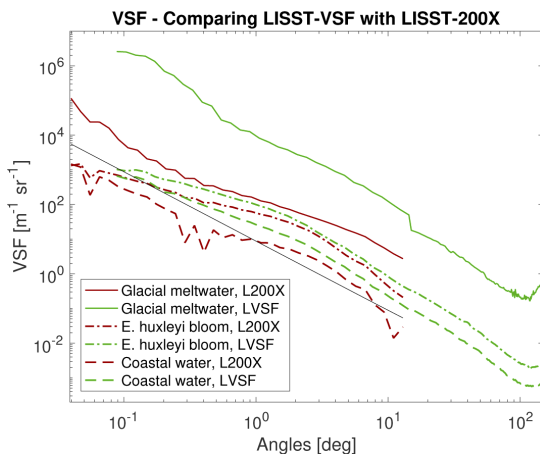


Fig. 15. The VSF measured with the LISST-200X and the LISST-VSF are compared for three different cases. Estimated minimum VSF-values that can be measured by the LISST-200X are indicated as a solid red line. Strong systematic errors due to multiple scattering are apparent for the LISST-VSF in turbid glacial meltwater.

3.2.4. Estimating scattering coefficient from forward scattering

The dominance of forward scattering on the scattering coefficient ($\beta(\theta < 13^\circ)$ contains on average $\sim 80\%$ of b) indicates the possibility that LISST-200X measurements can be used to estimate $b(670\text{nm})$. LISST-VSF measurements can be used for a robust evaluation, by computing b from both the entire VSF measurement and only the VSF of the LISST-200X angular domain ($0.08\text{--}13^\circ$). The former is computed by using the LISST-VSF measurement up to 145° and the backscattering extrapolation (described in Zhang et al. [9]) up to 180° , which can be assumed to be close to the correct b . The latter is computed by curve-fitting the Fournier-Forand VSF to the ring data (up to 13.2°), which is also used for the LISST-200X scattering. An example

is plotted in Fig. 16. The forward scattering extrapolation tends to systematically overestimate backscattering.

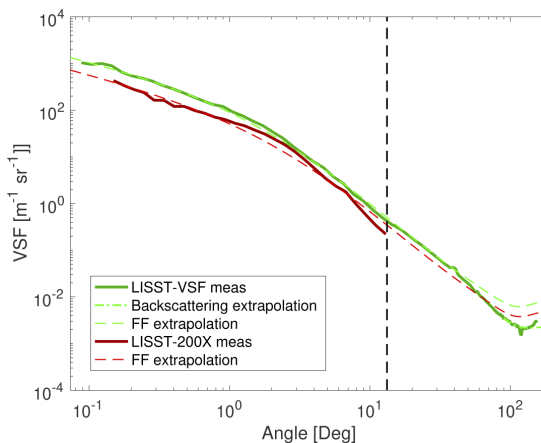


Fig. 16. Plot of LISST-VSF and LISST-200X measurements done at the same location and depth (*Emiliana Huxleyi* bloom, 0.5-10 m), together with extrapolations relevant for estimations of b .

In Fig. 17, the two calculated scattering coefficients are compared for a large selection of VSF measurements. Overall, the extrapolated scattering coefficient b_{FF} agrees well with the assumed correct value b_{corr} . A tendency to overestimate the scattering for $b > 1 \text{ m}^{-1}$ can be seen, but the overestimation of the backscattering has a relatively small impact. Linear regression for $b < 5 \text{ m}^{-1}$ gives the correlation shown in Fig. 17, with a 95% confidence interval (assuming a Gaussian distribution) of $\pm 20\%$ on the estimate. Limiting the regression to $b < 1 \text{ m}^{-1}$ decreases the confidence interval to $\pm 6\%$.

Scattering coefficients estimated from LISST-200X measurements (excluding VSF data under the detection limit) are compared with LISST-VSF scattering coefficients measured in the same waters in Fig. 18. Large variations are evident, but the expected trend of generally higher scattering at 515 than 670 nm can be seen. It is also clear that the LISST-200X b -estimates are much less affected by multiple scattering than the LISST-VSF values. The related deviations seem to take place above $\sim 2 \text{ m}^{-1}$.

3.2.5. Schlieren effect

The Schlieren effect is a scattering phenomenon caused by microturbulence and refractive index variations, a prevalent error source for scattering and transmission measurements in stratified natural waters. As Schlieren causes elevated forward scattering, it is primarily affecting the transmissometer and the innermost rings (similar to large particles, leading to errors in PSD calculations). Concurrent profiles with both LISST instruments and CTD instruments make it possible to investigate this effect. This is shown in Fig. 19, where transmission and scattering on the innermost ring of both LISST instruments are plotted with the buoyancy frequency. The buoyancy frequency is a widely used measure of stratification in oceanography, and has in previous studies been linked to Schlieren effects [16–18]. Figure 19(a) shows a clear decrease in LISST-VSF transmission measurements for increased buoyancy frequencies from 0.05 s^{-1} . For buoyancy frequencies at 0.15 s^{-1} and higher, many transmission measurements are close to

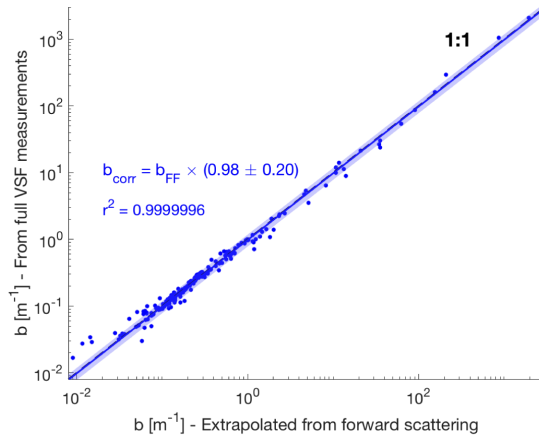


Fig. 17. The scattering coefficient estimated from LISST-VSF forward scattering (0.09° - 13.2°) compared with the scattering coefficient calculated from the full LISST-VSF measurement (0.09° - 145°).

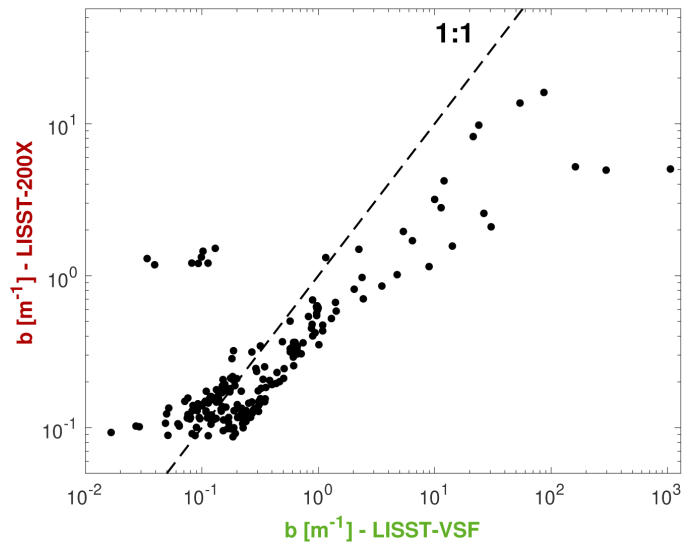


Fig. 18. Comparison of scattering coefficients, measured with LISST-VSF and estimated from LISST-200X forward scattering. Large variations can be seen, and LISST-VSF multiple scattering errors seems to occur from $\sim 2 \text{ m}^{-1}$.

being completely extinguished. However, perhaps the most striking feature is the *absence* of data points with both high transmission and buoyancy frequency; there seems to be an upper (lower) limit on the transmission (attenuation), linearly dependent on the buoyancy frequency. A trend is less clear for LISST-200X (Fig. 19(b)), due to the shorter pathlength, but above a buoyancy frequency of $\sim 0.15 \text{ s}^{-1}$, large fluctuations in the transmission are prevalent. Increases in the measured forward scattering can also be seen for both instruments (Fig. 19(c) and 19(d)). Ring saturation is also apparent in the LISST-VSF plot. However, it should be emphasized that the scattering measurements are coupled to the transmission through Eq. (6). Thus, suppressed transmission is likely a larger error source for VSF measurements in stratified waters than elevated forward scattering. A final consideration regarding these measurements is that the water density gradient (pycnocline) is associated with particle accumulation and flocculation. Hence, also larger particulate scattering can be expected here, and separating the two phenomena is a considerable challenge.

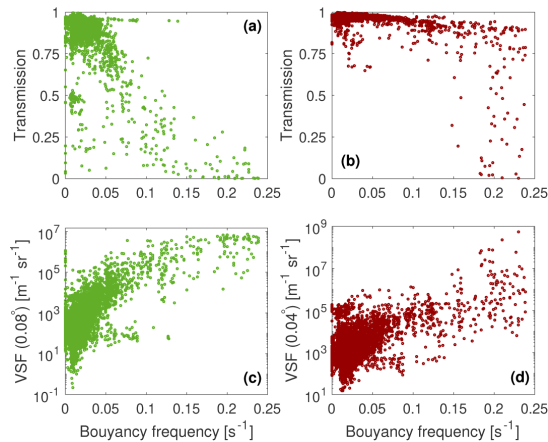


Fig. 19. Optical measurements plotted as a function of the buoyancy frequency, visualizing the Schlieren effect on LISST instruments; the transmission of LISST-VSF (a), the transmission of LISST-200X (b), the scattering on the inner-most LISST-VSF ring (c), and the scattering on the inner-most LISST-200X ring (d).

4. Conclusion

VSF measurements using the LISST-VSF and LISST-200X have been found to be valid over several orders of magnitude, making them valuable for further *in situ* and laboratory research. Bench-top measurements using monodispersed beads enable absolute calibration of the instrument detectors, but several considerations must be made with regards to instrument noise level, VSF oscillations, possible effects of bead flocculation and multiple scattering. We repeat in large parts procedures performed in earlier studies [11,24,29], but extend the eyeball calibration to a larger range. While the factory calibration of the LISST-VSF ring detector was shown to be satisfactory, the absolute calibration of the eyeball detector has greatly improved the robustness of the VSF measurements, avoiding significant propagation of uncertainties from the two outermost ring detectors to the entire eyeball detector domain. Having two independent detectors with different pathlengths also reveals multiple scattering effects in turbid waters. However, using the absolute

calibration requires that the PMT gain adjusts itself adequately to the particulate scattering. The lower thresholds of the LISST ring detectors have been given as angular dependent values ($c_{\text{scat}} \geq 10^{-4}$ for LISST-200X, $c_{\text{scat}} \geq 10^2$ for LISST-VSF), but note that these are order of magnitude numbers. The lower limit of the LISST-VSF eyeball detector depends on the PMT gain, and ambient light conditions under some circumstances.

LISST-VSF and LISST-200X have been extensively used in field campaigns, giving valuable knowledge on how to acquire high-quality data. For LISST-VSF, the water within the sample volume (beam area) must not be static while sampling, either in bench-top mode or during field deployment. The consequence of static water is large fluctuations in transmission and forward scattering. Our speculation is that the laser heats up the water enough to cause microturbulence effects. Hence, continuous descent and ascent is considered best practice during field deployment. For logistical reasons, a profiling speed of approximately 0.5 m/s has primarily been used, but a test with speeds down to 0.1-0.2 m/s have also produced good results. Due to the slow sample rate, we recommend using the lowest practical profiling velocity with the LISST-VSF. Another issue is collecting enough measurements for robust results, which is solved by doing multiple casts and calculating the median VSF, binned with respect to depth. For the LISST-200X, the deployment method is more flexible, but a similar continuous profiling protocol have been used. It has also been shown that temperature and salinity corrections are necessary for LISST-VSF measurements in very clear waters, but are not relevant for LISST-200X measurements.

Comparing the two instruments, their configuration makes them optimized for scattering measurements in different types of natural waters. The LISST-VSF, with its long pathlength, higher laser power and low sample rate, suits clear waters with low scattering, but also coastal waters. In turbid waters with scattering coefficients above approximately 2 m^{-1} , multiple scattering errors become significant, but further investigation is needed for details about the effects. LISST-200X is more suited for such waters, with a short pathlength and higher sample rate (which can detect more small-scale variations). However, the scattering and transmission detection levels makes it less suitable for measurements in clear natural waters. The configuration of the innermost rings makes it possible to detect scattering from less than 0.1° , but also makes the measurements vulnerable to errors due to the Schlieren effect. Schlieren has also been shown to significantly affect transmittance measurements, especially for buoyancy frequencies above 0.15 s^{-1} , which can have a severe effect on scattering measurements at all angles, as they are corrected by being divided on the transmittance (see Eq. (6)). Thus, care must be taken for measurements in stratified waters.

Even though LISST-200X only measures the VSF up to 13° , it has been shown that by curve fitting the Fournier-Forand phase function to the data, a good estimate of the scattering coefficient at 670 nm can be found. Thus, combined with attenuation measurements, the absorption at 670 nm can be calculated from $a = c - b$. Existing *in situ* spectrophotometers often yield measurements with large scattering-related uncertainties at longer wavelengths [38], especially in turbid waters. Due to its 2.5 cm path-length, the LISST-200X is less susceptible to multiple scattering errors, and may thus yield absorption measurements of higher accuracy than existing instrumentation in such waters. The instrument wavelength (670 nm) lies close to the chlorophyll-a pigment absorption peak at 676 nm. Thus, the instrument may be relevant for use with hyper-spectral *in situ* instrumentation for improved retrieval of primary production estimates in optically complex waters.

Acknowledgements

We thank the Norwegian Coast Guard, and especially the crew onboard KV Svalbard, for allocation of ship time and excellent field support during the cruise. We also thank the INTAROS and CAATEX project and NERSC for inclusion in the research cruises and support with the cruises. CTD measurements from six stations on the INTAROS cruise were provided by

Waldemar Walczowski, for which we are grateful. Moreover, Espesrend Marine Biology Lab have been very helpful with the fieldwork in Raunefjorden. Thomas Leeuw at Sequoia Scientific has also been of great help with providing us additional code for the LISST-instruments and answering questions regarding the instruments. Finally, we thank three anonymous reviewers for valuable reviews, which helped us improve upon our manuscript.

Disclosures

The authors declare no conflicts of interest.

References

1. D. Blondeau-Patissier, J. F. Gower, A. G. Dekker, S. R. Phinn, and V. E. Brando, "A review of ocean color remote sensing methods and statistical techniques for the detection, mapping and analysis of phytoplankton blooms in coastal and open oceans," *Prog. Oceanogr.* **123**, 123–144 (2014).
2. P. J. Werdell, L. I. McKinna, E. Boss, S. G. Ackleson, S. E. Craig, W. W. Gregg, Z. Lee, S. Maritorena, C. S. Roesler, C. S. Rousseaux, D. Stramski, J. M. Sullivan, M. S. Twardowski, M. Tzortziou, and X. Zhang, "An overview of approaches and challenges for retrieving marine inherent optical properties from ocean color remote sensing," *Prog. Oceanogr.* **160**, 186–212 (2018).
3. Y. Agrawal and H. Pottsmith, "Instruments for particle size and settling velocity observations in sediment transport," *Mar. Geol.* **168**(1-4), 89–114 (2000).
4. X. Zhang, M. Twardowski, and M. Lewis, "Retrieving composition and sizes of oceanic particle subpopulations from the volume scattering function," *Appl. Opt.* **50**(9), 1240–1259 (2011).
5. N. D. Stockley, R. Röttgers, D. McKee, I. Lefering, J. M. Sullivan, and M. S. Twardowski, "Assessing uncertainties in scattering correction algorithms for reflective tube absorption measurements made with a wet labs ac-9," *Opt. Express* **25**(24), A1139–A1153 (2017).
6. G. Mie, "Beiträge zur optik trüber medien, speziell kolloidaler metallösungen," *Ann. Phys.* **330**(3), 377–445 (1908).
7. M. I. Mishchenko, L. D. Travis, and D. W. Mackowski, "T-matrix computations of light scattering by nonspherical particles: a review," *J. Quant. Spectrosc. Radiat. Transfer* **55**(5), 535–575 (1996).
8. G. R. Fournier and J. L. Forand, "Analytic phase function for ocean water," in *Ocean Optics XII*, vol. 2258 (International Society for Optics and Photonics, 1994), pp. 194–201.
9. X. Zhang, G. R. Fournier, and D. J. Gray, "Interpretation of scattering by oceanic particles around 120 degrees and its implication in ocean color studies," *Opt. Express* **25**(4), A191–A199 (2017).
10. Y. C. Agrawal, "The optical volume scattering function: Temporal and vertical variability in the water column off the new jersey coast," *Limnol. Oceanogr.* **50**(6), 1787–1794 (2005).
11. W. H. Slade and E. S. Boss, "Calibrated near-forward volume scattering function obtained from the lisst particle sizer," *Opt. Express* **14**(8), 3602–3615 (2006).
12. E. Boss, W. H. Slade, M. Behrenfeld, and G. Dall'Omo, "Acceptance angle effects on the beam attenuation in the ocean," *Opt. Express* **17**(3), 1535–1550 (2009).
13. Y. Agrawal and O. A. Mikkelsen, "Empirical forward scattering phase functions from 0.08 to 16 deg. for randomly shaped terrigenous 1–21 μm sediment grains," *Opt. Express* **17**(11), 8805–8814 (2009).
14. L. Mullen, D. Alley, and B. Cochenour, "Investigation of the effect of scattering agent and scattering albedo on modulated light propagation in water," *Appl. Opt.* **50**(10), 1396–1404 (2011).
15. X. Zhang, D. J. Gray, Y. Huot, Y. You, and L. Bi, "Comparison of optically derived particle size distributions: scattering over the full angular range versus diffraction at near forward angles," *Appl. Opt.* **51**(21), 5085–5099 (2012).
16. R. Styles, "Laboratory evaluation of the lisst in a stratified fluid," *Mar. Geol.* **227**(1-2), 151–162 (2006).
17. O. A. Mikkelsen, T. G. Milligan, P. S. Hill, R. J. Chant, C. F. Jago, S. E. Jones, V. Krivtsov, and G. Mitchelson-Jacob, "The influence of schlieren on in situ optical measurements used for particle characterization," *Limnol. Oceanogr.: Methods* **6**(3), 133–143 (2008).
18. A. Karageorgis, D. Georgopoulos, W. Gardner, O. Mikkelsen, and D. Velaoras, "How schlieren affects beam transmissometers and lisst-deep: an example from the stratified danube river delta, nw black sea," *Medit. Mar. Sci.* **16**(2), 366–372 (2015).
19. J. E. Tyler, "Scattering properties of distilled and natural waters 1," *Limnol. Oceanogr.* **6**(4), 451–456 (1961).
20. T. J. Petzold, Volume scattering functions for selected ocean waters, Tech. rep., Scripps Institution of Oceanography La Jolla Ca Visibility Lab (1972).
21. E. Marken, N. Ssebiyonga, J. K. Lotsberg, J. J. Starnes, B. Hamre, Ø. Frette, A. S. Kristoffersen, and S. R. Erga, "Measurement and modeling of volume scattering functions for phytoplankton from norwegian coastal waters," *J. Mar. Res.* **75**(5), 579–603 (2017).
22. W. H. Slade, Y. C. Agrawal, and O. A. Mikkelsen, "Comparison of measured and theoretical scattering and polarization properties of narrow size range irregular sediment particles," in *2013 OCEANS-San Diego*, (IEEE, 2013), pp. 1–6.

23. T. Harmel, M. Hieronymi, W. Slade, R. Röttgers, F. Roullier, and M. Chami, "Laboratory experiments for inter-comparison of three volume scattering meters to measure angular scattering properties of hydrosols," *Opt. Express* **24**(2), A234–A256 (2016).
24. D. Koestner, D. Stramski, and R. A. Reynolds, "Measurements of the volume scattering function and the degree of linear polarization of light scattered by contrasting natural assemblages of marine particles," *Appl. Sci.* **8**(12), 2690 (2018).
25. D. Koestner, D. Stramski, and R. A. Reynolds, "Polarized light scattering measurements as a means to characterize particle size and composition of natural assemblages of marine particles: publisher's note," *Appl. Opt.* **59**(29), 9233 (2020).
26. B. Cochenour, S. P. O'Connor, and L. J. Mullen, "Suppression of forward-scattered light using high-frequency intensity modulation," *Opt. Eng.* **53**(5), 051406 (2013).
27. B. Cochenour, K. Dunn, A. Laux, and L. Mullen, "Experimental measurements of the magnitude and phase response of high-frequency modulated light underwater," *Appl. Opt.* **56**(14), 4019–4024 (2017).
28. R. Sahoo, P. Shanmugam, and S. K. Sahu, "Impact of air–sea interface effects and bubble and particulate scattering on underwater light field distribution: An implication to underwater wireless optical communication system," in *Optical and Wireless Technologies*, (Springer, 2020), pp. 171–178.
29. L. Hu, X. Zhang, Y. Xiong, and M.-X. He, "Calibration of the LISST-VSF to derive the volume scattering functions in clear waters," *Opt. Express* **27**(16), A1188–A1206 (2019).
30. X. Zhang, L. Hu, Y. Xiong, Y. Huot, and D. Gray, "Experimental estimates of optical backscattering associated with submicron particles in clear oceanic waters," *Geophys. Res. Lett.* **47**(4), e2020GL087100 (2020).
31. X. Ma, J. Q. Lu, R. S. Brock, K. M. Jacobs, P. Yang, and X.-H. Hu, "Determination of complex refractive index of polystyrene microspheres from 370 to 1610 nm," *Phys. Med. Biol.* **48**(24), 4165–4172 (2003).
32. S. N. Kasarova, N. G. Sultanova, C. D. Ivanov, and I. D. Nikolov, "Analysis of the dispersion of optical plastic materials," *Opt. Mater.* **29**(11), 1481–1490 (2007).
33. X. Zhang, L. Hu, and M.-X. He, "Scattering by pure seawater: effect of salinity," *Opt. Express* **17**(7), 5698–5710 (2009).
34. X. Zhang, D. Stramski, R. A. Reynolds, and E. R. Blocker, "Light scattering by pure water and seawater: the depolarization ratio and its variation with salinity," *Appl. Opt.* **58**(4), 991–1004 (2019).
35. W. H. Slade, E. Boss, and C. Russo, "Effects of particle aggregation and disaggregation on their inherent optical properties," *Opt. Express* **19**(9), 7945–7959 (2011).
36. L. Hu, X. Zhang, and M. J. Perry, "Light scattering by pure seawater at subzero temperatures," *Deep Sea Res., Part I* **162**, 103306 (2020).
37. R. Röttgers, D. McKee, and C. Utschig, "Temperature and salinity correction coefficients for light absorption by water in the visible to infrared spectral region," *Opt. Express* **22**(21), 25093–25108 (2014).
38. R. Röttgers, D. McKee, and S. B. Woźniak, "Evaluation of scatter corrections for ac-9 absorption measurements in coastal waters," *Methods Oceanogr.* **7**, 21–39 (2013).

Paper II

Analysis of multiple scattering errors in LISST-VSF volume scattering function measurements using Monte Carlo simulations and experimental data

Håvard S. Ugulen, Håkon Sandven, Børge Hamre, Arne S. Kristoffersen, and Camilla Sætre (2021), *Optics Express*, **29(8)**, 12413-12428, doi:10.1364/OE.419116



Analysis of multiple scattering errors in LISST-VSF volume scattering function measurements using Monte Carlo simulations and experimental data

HÅVARD S. UGULEN,* HÅKON SANDVEN, BØRGE HAMRE, ARNE S. KRISTOFFERSEN, AND CAMILLA SÆTRE

Department of Physics and Technology, University of Bergen, Allegaten 55, 5007 Bergen, Norway
*havard.ugulen@uib.no

Abstract: A Monte Carlo algorithm has been developed to investigate the effects of multiple scattering on the volume scattering function measured by the LISST-VSF instrument. The developed algorithm is compared to experimental results obtained from bench-top measurements using 508 nm spherical polystyrene beads and Arizona test dust as scattering agents. The Monte Carlo simulation predicts measured volume scattering functions at all concentrations. We demonstrate that multiple scattered light can be a major contributor to the detected signal, resulting in errors in the measured volume scattering function and its derived inherent optical properties. We find a relative error of 10% in the scattering coefficient for optical depths ~ 0.4 , and it can reach 100% at optical depths ~ 2 .

© 2021 Optical Society of America under the terms of the [OSA Open Access Publishing Agreement](#)

1. Introduction

Multiple scattering may be a significant source of systematic errors when measuring the inherent optical properties (IOPs) of particle-rich natural waters [1,2]. IOPs include the absorption coefficient and the volume scattering function (VSF) with its derived properties, such as the scattering coefficient b , and the backscattering coefficient b_b , all of which may vary spectrally. Turbid particle-rich waters are characteristically found in coastal and estuarine regions, which are of increased interest to the optical oceanography community due to the ecological and economic importance of these regions [3–7]. Increased knowledge of IOPs in such optically complex waters would be beneficial for remote sensing observations, environmental monitoring and underwater optical communication and visibility studies. The assumption of single scattering, where each photon is only scattered once, is an important approximation when measuring the VSF or other IOPs, as this negates the use of extensive radiative transfer calculations. However, this assumption will no longer be valid if the amount of multiple scattering is too high. In a study by Chami et al. [8], it was found through radiative transfer modeling that multiple scattering may contribute to as much as $\sim 94\%$ of the radiance reflectance when the ratio of backscattering to absorption is larger than 0.3.

The VSF $\beta(\theta)$ is defined as the radiant intensity dI scattered per elemental volume dV in the direction θ per unit incident irradiance E ,

$$\beta(\theta) = \frac{dI}{E dV} [\text{m}^{-1} \text{sr}^{-1}]. \quad (1)$$

Here, no azimuthal dependency is assumed. From this expression one can derive the scattering coefficient,

$$b = 2\pi \int_0^\pi \beta(\theta) \sin \theta d\theta. \quad (2)$$

The scattering phase function is given as

$$p(\theta) = \frac{\beta(\theta)}{b}. \quad (3)$$

The VSF has been sparingly measured *in situ*, especially at large scattering angles, due to lack of available instrumentation. The LISST-VSF (Sequoia Scientific) is a recently developed commercial instrument for measuring the VSF *in situ* or in the laboratory for angles 0.1–150° at a 515 nm wavelength [9]. The instrument uses a ring detector for measuring the light scattered from the incident laser beam (similar to other LISST-instruments) up to a scattering angle of 14.4°, while a rotating eyeball detector is used for angles 15–150°. While the geometries of the two detectors are different, both make the assumption that all detected light has been scattered solely from the beam. Light lost due to absorption or secondary scattering along the path of the scattered light is corrected for (see Section 2.2.2), but no additional light is assumed to be scattered into the detectors. It has been shown that applying an absolute calibration of the eyeball detector, using a method first presented by Hu et al. [10], yields a distinct discontinuity between the ring detector VSF and eyeball detector VSF in turbid waters [1]. In addition, the scattering values seem to be unreasonably elevated compared to parallel LISST-200X measurements, for which the sample chamber has a much shorter optical path length of 2.5 cm, compared to the 15 cm in the LISST-VSF. Microscopic polystyrene beads of precise and accurate size and concentration enable direct comparison of Mie theory and LISST-VSF measurements. Thus, polystyrene beads has been used to calibrate the LISST-VSF instrument [10–13]. In earlier laboratory measurements with 190 and 508 nm diameter polystyrene beads, we have seen similar VSF discontinuities at larger bead concentrations, as well as a non-linear relationship between scattering and particle concentration for 25 μm beads [1]. The discrepancies seen in both field and laboratory measurements motivate a deeper inquiry into the multiple scattering effects on the LISST-VSF measurements.

The single scattering approximation greatly simplifies the computation of IOPs from *in situ* measurements. The optical depth $\tau = cL$ has previously been used to state whether the single scattering assumption is a good approximation or not. Here, c is the attenuation coefficient, and L is the distance travelled in the medium. In the case of the LISST-VSF, this distance is $L = 0.15$ m, which is the characteristic path length of the instrument. The closely related scaled optical depth $\tau^* = cL(1 - g) = \tau(1 - g)$, is also used. Here, g is known as the asymmetry factor, calculated as the mean cosine of the scattering angle of the phase function [14]. In a paper by Koestner et al. [12], the general condition for single scattering is first given as $\tau \ll 1$. They also state that $\tau^* \ll 1$ can be used to determine the regime where the single scattering approximation is valid. However, these two conditions are quite different, as the asymmetry factor g is typically between 0.89 and 0.95 for natural waters [14]. In a study by Hu et al. [10], $c = 5 \text{ m}^{-1}$ is stated as the upper limit for single scattering, which translates to $\tau = 0.75$ for the LISST-VSF instrument. By contrast, van de Hulst [15] state a significantly stricter general condition for single-scattering: For an optical depth $\tau < 0.1$ (corresponding approximately to $\tau^* < 0.01$), single scattering can be assumed. For $0.1 < \tau < 0.3$, double-scattering corrections may be necessary, and for $\tau > 0.3$ multiple scattering must be taken into account. In a study by Agrawal and Mengüç [16], unnormalized VSF measurements were made using a nephelometer (with a fixed path length) over a wide range of mono- and polydispersed polystyrene bead concentrations. Here, the single-scattering condition was shown to agree well with the measurements up to an optical depth of 0.1, and by including an analytical double-scattering term, there was good agreement between theoretical results and measurements up to $\tau = 1.0$. Similar measurement series with increasing bead concentrations were performed by Chae and Lee [17], where a non-linear trend could be seen when scattering measurements were compared with optical thickness for $\tau > 0.1$, although the authors concluded that the relationship was reasonably linear.

Monte Carlo (MC) simulations offer an excellent tool for investigating optical instrumentation due to the straight-forward implementation of geometry in the simulations. Analytical solutions to light transport can be difficult, if not impossible, to find without the use of approximations. MC simulations, are on the other hand numerical solutions and can usually be implemented without approximations. MC simulations have previously been used to investigate a variety of optical instruments. McKee et al. [18] applied a MC simulation in order to investigate the scattering collection performance of the AC-9 (WET Labs, now Sea-Bird Scientific) reflecting tube absorption meter. Based on the MC simulation, they developed an iterative scattering error correction procedure, which was later improved upon [19]. In Doxaran et al. [20] and Vadakke-Chanat et al. [21], the uncertainty and effects of absorption was analyzed and quantified for back scattered light in the ECO-BB9 (WET Labs, now Sea-Bird Scientific) sensor. Other examples can be found in [22–24]. In this paper, we present a MC simulation to investigate the effects of multiple scattering in LISST-VSF measurements. The aim of the work is to explain the observed features in the measured VSF, and to quantify errors in the phase function and scattering coefficient originating from multiple scattering.

2. Methods

2.1. LISST-VSF measurements

Two different scattering agents are used in this study: Polystyrene beads and Arizona test dust. The polystyrene beads solution is monodisperse with a particle size distribution centered at 508nm and with a full-width half-maximum of 16 nm. The Arizona test dust solution was made from dry powder with original particle sizes ranging from 0-50 μm . The mixed solution was left to stabilize overnight so that larger particles would settle, leaving only the smaller particles suspended in the solution. Consequently, the particle size distribution for the Arizona test dust measurements is not known but is expected to be dominated by the smaller particles.

All VSF measurements were performed in the laboratory using the LISST-VSF instrument in its benchtop mode. Each measurement series commenced with 1630 mL of milli-Q water being poured into the instrument sample chamber. After waiting one hour for bubbles to dissipate, a blank measurement was made. Subsequently, the scattering agent was added from a master solution to the sample chamber in predetermined amounts using pipettes for precise concentrations. The milli-Q water used in the blank was also used in the following measurements, yielding an effective subtraction of pure water scattering and other possible optical losses. A series of measurements were made with subsequent additions of scattering agent solution, going from low to very high concentrations. The concentrations used in this study are given in Table 1 (Section 3.1). To minimize uncertainties connected to the particle concentrations, the VSF measurements were scaled by the ratio of theoretical (Mie theory) and measured (LISST-VSF) attenuation,

$$\beta_{\text{corr}}(\theta) = \beta_{\text{uncorr}}(\theta) \frac{c_{\text{Mie}}}{c_{\text{LISST}}}, \quad (4)$$

as the LISST-VSF attenuation measurements have been shown to have high accuracy above $\sim 0.1 \text{ m}^{-1}$ and are virtually unaffected by multiple scattering [1,23]. This correction was only applied to the polystyrene beads measurements due to the lack of a theoretical attenuation coefficient for the Arizona test dust samples.

2.2. Monte Carlo simulation

Here, we present a Monte Carlo simulation based on the random sampling of variables. The variables are expressed as probability distributions, so that the value of a certain variable can be sampled by generating a random number $\xi \in [0, 1]$. The geometry of the simulation is presented in Fig. 1. The simulation boundary is defined by a cylinder with a length stretching

from $z = 0$ cm to $z = 15$ cm, and a radius of 2 cm. The light source is positioned at the center of the top end of the cylinder ($z = 15$ cm) and the photons are emitted along the z -axis towards the bottom end of the cylinder. The eyeball detector is positioned at the cylinder wall at $z = 5$ cm, so that the distance from the light source is 10 cm along the z -axis. The ring detectors are positioned at $z = 0$ cm and covers the entire bottom area of the cylinder. The cylinder wall act as a perfect absorber, so that all photons crossing the cylinder boundaries are immediately eliminated. It is desirable to minimize the computation time of the simulation without compromising the precision. Thus, the cylinder radius of 2 cm is chosen, as it is considered statistically highly unlikely for a photon that has crossed this cylinder wall boundary to be scattered back into the sample volume and into a detector.

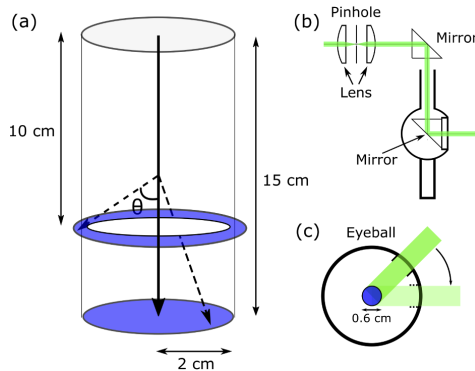


Fig. 1. Illustration of the simulation geometry. (a) The cylindrical sample volume with ring detector in the bottom end of the cylinder and eyeball detector as a ring torus at $z=5$ cm, both colored in blue. Forward scattered light collected by the blue disk (collecting lens) are sorted by their angle of incidence onto the disk. In the instrument, all photons arriving at a particular angle of incidence are directed to a corresponding ring detector. (b) Eyeball detector principle in the LISST-VSF instrument. (c) Eyeball detection principle in the simulation with the detection sphere colored in blue.

The individual photon's trajectory through the sample volume is calculated following the steps outlined in the flow chart presented in Fig. 2. The distance between photon-particle interaction will here be referred to as step size, where the step size distribution can be derived from the attenuation of a beam,

$$I = I_0 e^{-cl}. \quad (5)$$

Here, I_0 is the initial intensity of the beam, c is the attenuation coefficient, l is the distance over which the beam is attenuated, and I is the intensity after traveling the distance l . A random step size can then be sampled from the distribution where the sampled step size s can be calculated as

$$s = \frac{-\ln(\xi)}{c}. \quad (6)$$

The new position of the photon is calculated based on the traveling direction and the sampled step size, and the scattering angle distribution is obtained from the scattering probability density

function (PDF) of the sample in question. The scattering PDF is given as

$$f(\theta) = 2\pi p(\theta) \sin \theta \quad (7)$$

and integration yields

$$\int_0^\pi f(\theta) d\theta = 2\pi \int_0^\pi p(\theta) \sin \theta d\theta = 1, \quad (8)$$

where $p(\theta)$ is the scattering phase function. The scattering angle θ is randomly sampled by generating a new $\xi \in [0, 1]$. The sampled scattering angle θ_{sc} is then found from the relation

$$2\pi \int_0^{\theta_{sc}} p(\theta) \sin \theta d\theta = \xi. \quad (9)$$

A lookup table containing the values of θ_{sc} for different ξ is made prior to the simulation. The azimuthal angle ϕ is sampled from a uniform distribution from 0 to 2π . When performing a simulation for the 508 nm spherical polystyrene beads, a theoretical phase function computed from Mie theory is used as input. For Arizona test dust, the input phase function is obtained from a LISST-VSF measurement at low concentration, so that one can assume that the single scattering approximation is valid.

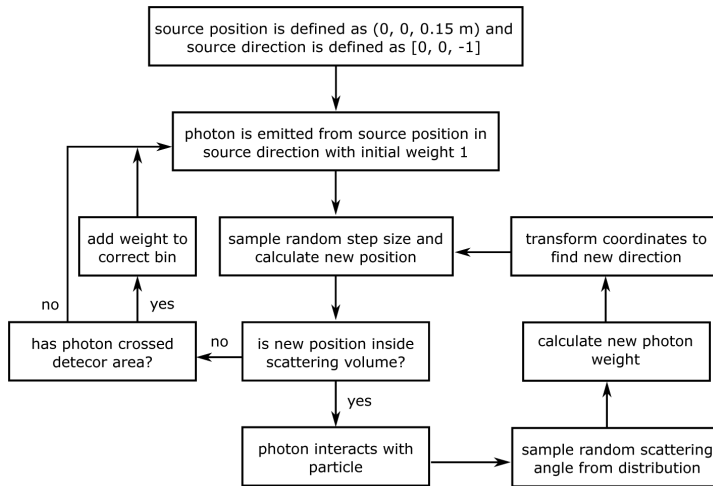


Fig. 2. Flowchart showing the steps in the Monte Carlo algorithm.

In order to account for absorption by the sample volume, we give the photons an initial weight $w = 1$, and at each scattering event, the weight is reduced according to

$$w_{i+1} = w_i \frac{b}{c} \quad (10)$$

where w_{i+1} is the weight after scattering, w_i is the weight before scattering, c is the attenuation coefficient, and b is the scattering coefficient. This avoids having to initiate a new photon every time one is absorbed. As the LISST-VSF measurement is calibrated so that the absorption and scattering from the water itself is zero, there is no need to implement the attenuation from water in the simulation.

2.2.1. Simulation of detectors

Ring detectors In order to detect the scattered intensity in the range $0.09 - 14.4^\circ$, the LISST-VSF uses a set of ring detectors, covering different parts of the range. A lens is positioned above the ring detectors, focusing the light at the different rings depending on the angle of incidence. This detection scheme is simulated by simply defining a flat circle surface, corresponding to the lens, and registering the angle of incidence onto this surface, as illustrated in Fig. 1(a). The registered photons are then binned according to their angle of incidence, matching the bin sizes of the LISST-VSF.

Eyeball detector The eyeball detection scheme is illustrated in Fig. 1(b). The light passes through an opening in the eyeball, leading to a set of reflecting mirrors. The mirrors guide the light to a spatial filter consisting of two lenses and a pinhole, resulting in an acceptance angle of $2\theta_a = 0.9^\circ$. The total power reaching the detector is thus dependent on the opening of the eyeball and the acceptance angle. While the LISST-VSF eyeball rotates in order to measure the angle dependency of the scattered light, the simulation can detect scattered light from all angles θ simultaneously. This is achieved by defining a sphere positioned at the center of the eyeball, where passing through this sphere is the equivalent of passing through the eyeball opening and being within the acceptance angle of the spatial filter. The principle behind this design is illustrated in Fig. 1(c), and while this is a major simplification of the eyeball detection system, the results presented in this paper demonstrate that it works very well. A sphere radius of 3 mm was found to give a good fit to the experimental results. The simulation also allows us to extend this eyeball design around the cylinder, creating a ring torus (see Fig. 1(a)). This is the equivalent of having eyeball detectors covering the entire circumference of the cylinder, as opposed to the LISST-VSF which only has one eyeball detector at a single location. Thus, the simulation can detect scattered photons for all azimuth angles.

2.2.2. Processing simulated data

To obtain a VSF from the MC simulation, the raw data, i.e. number of photons detected at each angle, must be processed. The VSF is calculated based on the method presented in [25]. The number of scattered photons detected by the ring detectors can be calculated for each bin (ring) as

$$N_i = 2\pi e^{-cl} x N_0 \beta_i(\theta) \phi (\cos \theta_{i,l} - \cos \theta_{i,h}), \quad (11)$$

where e^{-cl} is the attenuation factor and l is the total distance traveled from the laser injection point to the detector, assuming single scattering. The factor x is the length of the laser beam contributing to the signal (see Fig. 3), N_0 is the total number of simulated photons, equivalent to the laser power, $\beta_i(\theta)$ is the VSF for bin i , and $\theta_{i,h}$ and $\theta_{i,l}$ is the high and low limit of the bin, respectively. The symbol ϕ does here refer to the fraction of a full circle covered by the ring detectors. For practical reasons, the ring detectors in the LISST-VSF only cover 1/6 of the full circle, meaning that $\phi = 1/6$. In the simulation however, we can use the full circle so that $\phi = 1$. Rearranging Eq. (11), we get the following expression for the VSF

$$\beta_i(\theta) = \frac{N_i}{N_0} \frac{e^{cl}}{2\pi \phi x (\cos \theta_{i,l} - \cos \theta_{i,h})}. \quad (12)$$

Here, the factor e^{cl} accounts for photons lost along the path to the detector. For the ring detector, l does not vary much with detection angle, and is set to $l = L = 0.15$ m. An identical correction for attenuation is done for the LISST-VSF measurements. For angles smaller than $\arctan(r/L)$, where r is the radius of the lens focusing light at the ring detectors, the entire beam contributes to the signal, so that $x = L = 0.15$ m. For angles larger than this, only a fraction of

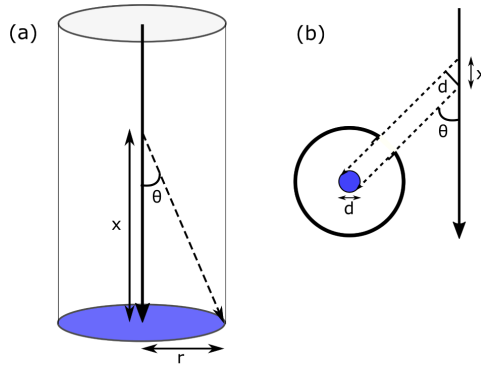


Fig. 3. Geometric illustration of the contributing length x of the laser beam for (a) the ring detector and (b) the eyeball detector.

the beam contributes as the photons scattered from the top end of the beam does not hit the lens (see Fig. 3(a)). In this case, x is calculated as $x = r/\tan \theta_i$, such that Eq. (12) becomes

$$\beta_i(\theta) = \frac{N_i}{N_0} \frac{e^{cl} \tan \theta_i}{2\pi\phi r(\cos \theta_{i,l} - \cos \theta_{i,h})}, \quad (13)$$

where θ_i is the mean angle for bin i .

The same approach is used to calculate the VSF from the signal obtained by the eyeball detector. In this case, only a small fraction of the beam contributes to the signal, where x is calculated as $x = d/\sin \theta_i$ (see Fig. 3(b)). Here, $d = 6$ mm is the diameter of the eyeball detection sphere defined in Section 2.2.1.2. The VSF for the eyeball detector can then be calculated for bin i as,

$$\beta_i(\theta) = \frac{N_i}{N_0} \frac{e^{cl} \sin \theta_i}{2\pi\phi d(\cos \theta_{i,l} - \cos \theta_{i,h})}. \quad (14)$$

Here, the path length l is dependent on the angle of detection, and can be calculated as

$$l = l_{\text{eye}} - R \cot \theta + \frac{R}{\sin \theta}, \quad (15)$$

where $l_{\text{eye}} = 0.10$ m is the distance from the top end of the cylinder to the eyeball detector along the z -axis, and R is the distance from the laser beam to the eyeball detector measured at a right angle. Again, we can set $\phi = 1$ due to the full circle coverage of the eye detector.

In order to ensure a similar signal for all samples, the simulation is set to run until 10^7 photons are detected by the eye detector, i.e. $\sum N_{i,\text{eye}} = 10^7$. The same limit is set for the ring detector, at which the detector stops counting detected photons. The final signal in the ring detector is then calculated as $N_i = N \cdot N_{i,\text{stop}}/N_{\text{stop}}$, where N_i is the adjusted number of photons in bin i , N is the total number of photons simulated, $N_{i,\text{stop}}$ is the number of photons in bin i at which the limit of 10^7 detected photons is reached, and N_{stop} is the total number of simulated photons when the number of detected photons reaches 10^7 .

3. Results and discussion

3.1. Monte Carlo simulations compared with experimental results

The results obtained using the polystyrene beads as the scattering agent are presented in Fig. 4. The simulation input parameters b and c are given in Table 1, along with the corresponding

experimental particle concentrations C and optical depths τ . Measurements by the LISST-VSF are compared with single-scattering theoretical values computed from Mie theory, and simulation results from the Monte Carlo algorithm. At low concentrations, the theoretical, measured, and simulated VSF are in overall good agreement. For increasing particle concentrations, the measured VSF increasingly deviates from the theoretical VSF, both in magnitude and shape. For the highest bead concentration, the amount of measured scattering at large angles is more than an order of magnitude larger than predicted from single scattering, and the oscillating features of the 508 nm bead phase function have vanished. Another prominent feature at higher concentrations is the discontinuity at 15° . This angle is the boundary between where the VSF is measured by the ring detector and where the eye detector is used.

Table 1. Simulation input parameters b and c , and corresponding particle concentrations C (or relative concentrations C_r) and optical depths τ for the 508 nm beads and Arizona test dust samples.

Sample No.	508 nm beads				Arizona test dust			
	C [$\mu\text{L/L}$]	b [m^{-1}]	c [m^{-1}]	τ	C_r	b [m^{-1}]	c [m^{-1}]	τ
1	0.050	0.182	0.183	0.027	1	0.084	0.088	0.013
2	0.10	0.365	0.365	0.055	3	0.253	0.263	0.039
3	0.21	0.766	0.767	0.12	10	0.842	0.876	0.13
4	0.51	1.86	1.86	0.28	30	2.53	2.63	0.39
5	1.0	3.68	3.69	0.55	100	8.41	8.75	1.3
6	2.0	7.43	7.44	1.1	296	24.9	25.9	3.9
7	3.0	11.1	11.1	1.7	-	-	-	-
8	4.0	14.7	14.7	2.2	-	-	-	-
9	6.0	21.9	22.0	3.3	-	-	-	-
10	8.9	32.8	32.9	4.9	-	-	-	-

By contrast, the simulation predicts a VSF with closer resemblance to the LISST-VSF measurements, even at the highest scattering coefficient $b \approx 33 \text{ m}^{-1}$. Some minor deviations can be seen. At small scattering angles ($<7^\circ$) and low concentrations, the LISST-VSF measured enhanced forward scattering relative to theory, whereas the simulated and theoretical curves are almost indistinguishable. The reason is not entirely clear, but is likely attributed to bead flocs, i.e., beads clumped together and effectively acting as larger particles [1,26]. Increased forward scattering for larger particles is consistent with Mie theory. The bead flocs may then deflocculate (break apart) when mixing with water during the experiments, resulting in the spike gradually vanishing. The concentrated polystyrene bead solution was also shaken before each addition of beads to the LISST-VSF sample chamber, so later additions of beads were more thoroughly shaken. Thus, the later additions of beads may have contained less flocculated beads, adding to the reduction of the forward spike. There are other possible explanations for the observed spike in forward scattered intensity. Local heating of the sample volume in the vicinity of the laser beam might cause a temperature gradient to arise, which in turn results in density gradients and deviations in the refractive index [27]. Such deviations can cause scattering of light, and thereby an increase in the measured forward scattering. However, if this were the case, one would also expect to measure increased attenuation, which is not observed in our experiments. Thus, this explanation is considered unlikely. The discontinuity at 15° is also apparent in the simulated VSF, but appears larger in the experimental data for sample Nos. 6-9. After inspection of the experimental raw data, we find that this is due to saturation of the eye detector sensor at the smallest angles ($15 - 25^\circ$). At the highest concentration, the saturation is quenched by increased attenuation of the light (which is compensated for in the data processing), hence the improved agreement between the experiment and simulation for sample No. 10. From 140° and

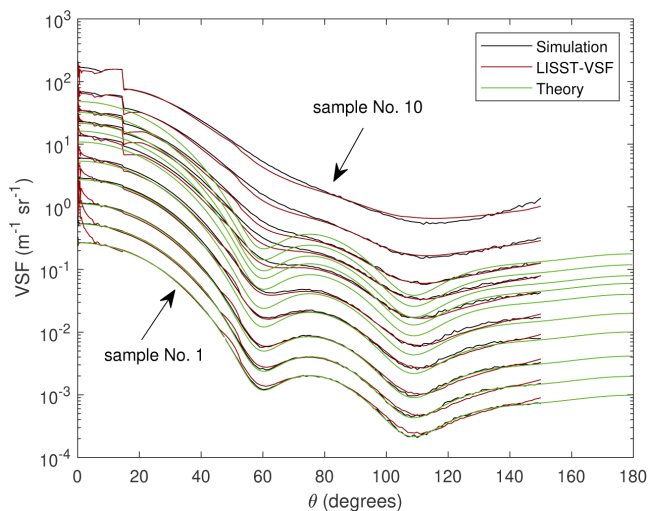


Fig. 4. Volume scattering functions measured by the LISST-VSF (red line) for varying 508 nm bead concentrations (see Table 1), are plotted with theoretically predicted results assuming single scattering (green line), and results from the Monte Carlo simulations of the LISST-VSF measurements (black line). The abrupt jump in the VSF seen at 15° is due to the longer optical path for the ring detector than for the eyeball detector.

onward, the simulated backscattering increases relative to the experimental backscattering, with increasing particle concentration. This is most likely due to the simulated eyeball detection being a simplified version of the instrument eyeball detection. Consequently, the two different eyeball detection schemes might probe the sample volume slightly different, resulting in deviations in the VSF when the turbidity becomes very high.

The Arizona test dust results are presented in Fig. 5. The simulation input parameters b and c are given in Table 1, with the corresponding experimental relative particle concentrations (specific particle concentration is not known) and optical depths τ . Here, the theoretical VSF is acquired from a low concentration sample and scaled according to the relative concentrations C_r presented in Table 1. The results follow the same trend as for the polystyrene beads, showing clear deviations between the predicted values for single scattering and the measurements at high concentrations, and close agreement between simulated and experimental results. A clear difference in the two phase functions, are the oscillatory features seen in the 508 nm beads phase function (see Fig. 4), as opposed to Arizona test dust phase function, where such features are not present. The oscillatory features appear due to constructive and destructive interference of the electromagnetic field scattered by individual particles [12,28]. The angular positions of constructive and destructive interference are dependent on particle size and refractive index, such that the monodisperse 508 nm beads samples will display oscillations in the phase function, while the polydisperse Arizona test dust samples will not.

Results seen in Figs. 4 and 5 validate the developed Monte Carlo simulation of the LISST-VSF, and offer robust explanations of instrument artifacts seen in both laboratory and field measurements. Multiple scattering causes both erroneously large detected scattering and an altered phase function. The discontinuity at 15° arises due to the sudden decrease in path length

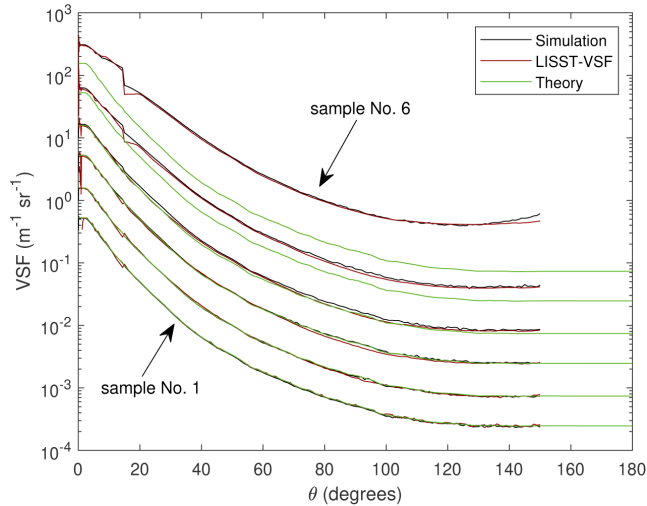


Fig. 5. Volume scattering functions measured by the LISST-VSF (red line) for varying Arizona test dust concentrations (see Table 1), are plotted with theoretically predicted results assuming single scattering (green line), and results from the Monte Carlo simulations of the LISST-VSF measurements (black line).

going from ring detectors to eyeball detector (see Fig. 1). This decrease in path length has a double effect on the measured VSF. Firstly, longer path lengths result in more multiple scattered photons. Secondly, the attenuation factor e^{cl} is larger for the ring detectors (Eq. (12)) than for the eye detector (Eq. (14)) in the forward direction. Thus, the increase in number of detected photons N_j due to multiple scattering contributes more to the absolute error in the VSF measured by the ring detector compared to the one measured by the eyeball detector. However, this does not impact the relative error. Saturation of the eyeball detector may also be a significant factor in waters dominated by scattering processes.

3.2. Error analysis

3.2.1. Convergence test

A convergence test has been performed for the 508 nm beads sample No. 1 (see Table 1 for details about the sample). Convergence is tested for the scattering coefficient b , calculated from Eq. (2), and the results are presented in Fig. 6. For the test, the simulation is set to run until a specific number of photons N_{eye} are detected by the eye detector, starting at 1221 photons and doubling for each simulation up to 10^7 (same as for the results presented in Figs. 4 and 5). The simulation is repeated 10 times for each N_{eye} , providing enough data to calculate a coefficient of variance (CV), also known as relative standard deviation. The CV is calculated as $c_v = \frac{\sigma}{\mu} \times 100\%$, where σ is the standard deviation of the mean μ . The calculated scattering coefficients b from the simulations are presented in Fig. 6(a), and the CV of b is plotted in Fig. 6(b), in addition to a theoretical fit calculated as $c_v = C/\sqrt{N_{\text{eye}}}$, where C is a proportionality constant.

From Fig. 6, one can see that b converges relatively fast. In fact, the CV is below 1% when N_{eye} is larger than 10^4 . While the simulated VSF obtained from a signal of 10^4 detected photons would be very noisy, the scattering coefficient can be accurately predicted as it is obtained from

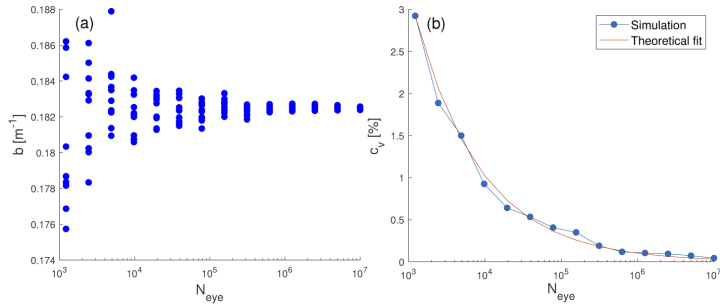


Fig. 6. (a) Scattering coefficient b calculated from simulation for increasing number of detected photons N_{eye} for sample No. 1. (b) Coefficient of variance c_v for increasing number of detected photons N_{eye} and a theoretical fit calculated as $c_v = C/\sqrt{N_{\text{eye}}}$, with $C = 102$.

integrating the VSF over the angles $0.09^\circ - 150^\circ$ (see Eq. (2)). At 10^7 detected photons, the CV is approximately 0.04%, giving a very high precision. A similar convergence test was performed for sample number 5, and no significant difference in CV was found. Thus, it was concluded that the optical depth has little to no influence on the CV for the scattering coefficient.

3.2.2. Multiple scattering error

The validity of the single-scattering approximation may readily be assessed by comparing the Monte Carlo simulation results with the predicted results from assuming single-scattering. For the error analysis, the theoretical scattering coefficients and phase functions are calculated from the VSFs labeled "Theory" in Fig. 4 and 5. The theoretical, experimental, and simulated scattering coefficients, denoted b_t , b_e , and b_s , respectively, are given in Table 2. The scattering coefficients are calculated by integrating from 0.09° to 150° , so that theory, experiment and simulation are considered over the same angular spectrum. Thus, the theoretical scattering coefficient is not the same as the input scattering coefficient given in Table 1.

Table 2. Theoretical b_t , experimental b_e , and simulated b_s scattering coefficients for the 508 nm beads and Arizona test dust samples. The scattering coefficients are calculated by integrating from 0.09° to 150° .

Sample No.	508 nm beads			Arizona test dust		
	b_t [m^{-1}]	b_e [m^{-1}]	b_s [m^{-1}]	b_t [m^{-1}]	b_e [m^{-1}]	b_s [m^{-1}]
1	0.182	0.186	0.182	0.086	0.084	0.084
2	0.363	0.360	0.367	0.258	0.257	0.254
3	0.763	0.750	0.781	0.858	0.837	0.871
4	1.85	1.84	1.97	2.58	2.64	2.83
5	3.67	3.83	4.14	8.57	11.7	12.5
6	7.40	8.56	9.54	25.4	85.2	89.0
7	11.0	14.5	16.25	-	-	-
8	14.6	22.5	24.8	-	-	-
9	21.8	47.2	49.8	-	-	-
10	32.7	119.7	123.7	-	-	-

From Table 2, one can see that a difference in the theoretical single-scattering scattering coefficient b_t and the experimental scattering coefficient b_e can be quite dramatic for high particle concentrations. As the LISST-VSF attenuation measurements have been shown to have a high accuracy and are virtually unaffected by multiple scattering [1,23], one would see a similar dramatic difference in the measured absorption a , calculated as $a = c - b$. In fact, in some cases, when $b > c$, one would get a negative absorption coefficient. The relative errors due to multiple scattering for the scattering coefficient and phase function are plotted in Fig. 7. Three different relative errors are presented. The desired output from a LISST-VSF measurement is the single-scattering phase function and scattering coefficient, and are thus taken as true values when computing the error in the LISST-VSF measurements. This is also the case when comparing simulated results to single scattering. When comparing simulation and experiment, the experimental results are taken as true values, as the goal of the simulation is to reproduce the LISST-VSF measurements. The scattering coefficient relative error e_b is computed from

$$e_b = \frac{|b_{\text{meas}} - b_{\text{true}}|}{b_{\text{true}}} \times 100\%. \quad (16)$$

For the phase function, where the error may vary significantly with angle, the mean relative error e_p is calculated, using

$$e_p = \frac{1}{n} \sum_i^n \frac{|p_{\text{meas}}(\theta_i) - p_{\text{true}}(\theta_i)|}{p_{\text{true}}(\theta_i)} \times 100\%. \quad (17)$$

The measured phase function is measured at log-spaced angles at $<15^\circ$. To avoid bias towards forward scattering effects, the data was interpolated to evenly spaced angles.

The scattering coefficient and phase function errors for the 508 nm beads samples are plotted in Figs. 7(a) and (b), respectively, and the errors for the Arizona test dust samples are plotted in Figs. 7(c) and (d). The error is plotted against the dimensionless parameter τ . As seen in Fig. 7, the simulation predicts a scattering coefficient and phase function close to those derived from the LISST-VSF measurements. For the scattering coefficients, the relative error is always $<13\%$, and $<10\%$ for the phase function. As discussed in section 3.1, a large portion of the error in the simulation relative to the LISST-VSF measurements can be attributed to measurement errors in the experimental results. Comparing simulation and experiment to the single-scattering theoretical values, the errors in the scattering coefficients arise solely due to the added intensity from multiple scattered photons. The phase function, however, is normalized so that the addition of multiple scattered photons does not alone cause the error. Rather, it is the angular distribution of multiple scattered photons that causes the error. Due to the phase functions being highly forward peaked, the photons scattered more than once tend to be distributed to angles close to the original scattering angle. As a consequence, phase functions that varies rapidly with scattering angle is more subjected to multiple scattering errors in the phase function, as the relative increase in signal becomes large when a low signal part of the spectrum neighbors a high signal part. This is especially evident looking at the relative error in the phase functions (Figs. 7(b) and (d)), where the error is significantly larger for the 508 nm beads than for the Arizona test dust. This is due to the low signal dips in the 508 nm beads phase function, approximately at 60° and 110° , gaining a relatively large quantity of multiple scattered photons from the neighboring higher signal parts. Ultimately, as the optical depth approaches infinity, the angular distribution of photons becomes completely random, resulting in a uniform VSF.

Comparing simulation to theory, the error in the scattering coefficient is calculated to be $e_b = 0.4\%$ for the 508 nm at an optical depth of $\tau = 0.027$. The error increases with optical depth reaching $e_b = 29\%$ for $\tau = 1.1$, and finally $e_b = 278\%$ for $\tau = 4.9$. As the CV was calculated to be $c_v = 0.04\%$, the numerical uncertainty in the simulated results can be considered

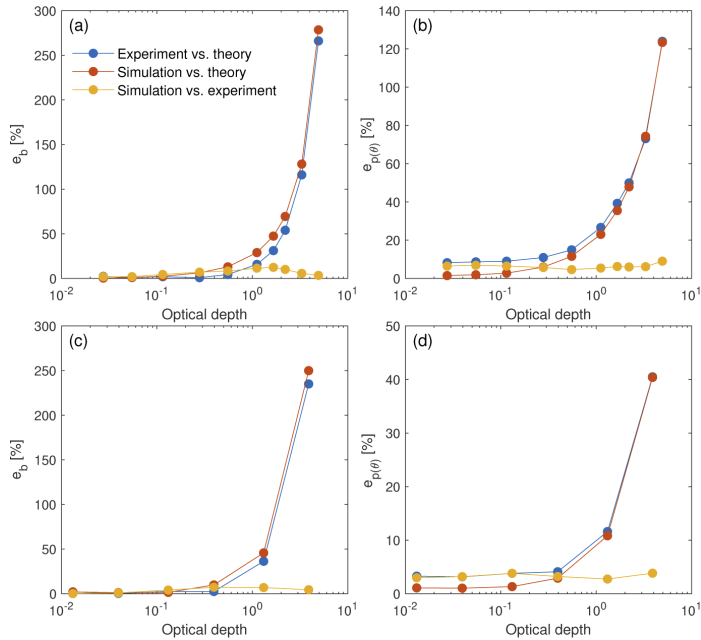


Fig. 7. Relative errors calculated from comparing experiment vs. theory (blue), simulation vs. theory (red) and simulation vs. experiment (yellow). Relative error of (a) the scattering coefficient e_b and (b) the phase function $e_{p(\theta)}$ for the 508 nm beads samples. Relative error of (c) the scattering coefficient e_b and (d) the phase function $e_{p(\theta)}$ for the Arizona test dust samples. The errors are plotted against the dimensionless optical depth τ .

negligible, except for at the smallest optical depths. The error in the phase function is, for the most part, significantly smaller than for the scattering coefficient. The exceptions are for the three smallest optical depths. This is probably due noise being the dominating source of error when the difference between simulated and theoretical VSF becomes very small. The scattering coefficient is not subjected to noise in the same way, as the scattering coefficient is calculated by integrating the VSF over the entire angular range (see Eq. (2)). At the smallest optical depth $\tau = 0.027$, the error is calculated to be $e_p = 2\%$, increasing to $e_p = 123\%$ for the largest optical depth of $\tau = 4.9$. For the Arizona test dust, the error in the scattering coefficient goes from $e_b = 2\%$ to $e_b = 250\%$ when the optical depth goes from $\tau = 0.013$ to $\tau = 3.9$. The error in the phase function goes from $e_p = 1\%$ to $e_p = 40\%$ for the same values of τ . An overview of the optical depths at which the scattering coefficient and phase function reach specific relative errors is presented in Table 3. The values presented are calculated by linear interpolation of the results labeled as "Simulation vs. theory" in Fig. 7.

As seen in the results presented here, a 15 cm path length is sufficient to cause considerable errors in the measured VSF and its derived inherent properties, here represented by the scattering coefficient and phase function. Thus, it becomes interesting to compare the LISST-VSF with other optical equipment and measurements. For instance, the historical Petzold measurements are often used as a reference to *in situ* data [29]. For these measurements, two different instruments

Table 3. Optical depths at which the 508 nm beads and Arizona test dust reach specific levels of relative error in the scattering coefficient b and phase function $p(\theta)$.

Relative error	Scattering coefficient		Phase function	
	508 nm beads	Arizona test dust	508 nm beads	Arizona test dust
1%	0.055	NaN	NaN	NaN
2%	0.10	0.15	0.062	0.24
5%	0.23	0.24	0.23	0.64
10%	0.43	0.40	0.48	1.2
30%	1.1	0.91	1.4	3.0
50%	1.7	1.4	2.3	NaN
100%	2.8	2.0	4.1	NaN

were used, depending on the scattering angle. The instrument used to measure the low angle scattering (approximately $0.06^\circ - 0.4^\circ$) had a path length of 50 cm, while the range $10^\circ - 170^\circ$ was measured at a path length of 18.8 cm. The VSF was measured for a range of different ocean waters, with an attenuation coefficient peaking at 2.190, which translates to an optical depth of 1.1, for the longest path length of 50 cm. From Table 3, one can see that this results in a relative error of approximately 30% in the measured scattering coefficient, assuming the equipment is subjected to multiple scattering similarly to the LISST-VSF.

4. Summary and conclusion

We have demonstrated that the errors originating from multiple scattering in the LISST-VSF measurements can be significant for large optical depths, which largely explains *in situ* LISST-VSF measurement artifacts seen in turbid waters measurements. The developed Monte Carlo algorithm has been validated by employing 508 nm polystyrene beads and Arizona test dust as scattering agents, and has proven to be an accurate tool for analyzing errors in both the measured phase function and scattering coefficient. A convergence test was performed for the MC algorithm, from which we found a coefficient of variance of $c_v \leq 0.04\%$ for the scattering coefficient. Comparing simulation to experiment, the relative error is $<13\%$ for the scattering coefficient and $<10\%$ for the phase function, for the concentrations and scattering agents tested in this study. A large fraction of these errors can be attributed to errors in the LISST-VSF measurements, caused by particle flocculation, or saturation of the eyeball detector.

Comparing the simulated VSF to the single-scattering VSF, the relative error in the scattering coefficient reaches 10% for an optical depth of $\tau \approx 0.4$ for both scattering agents, while an error of 100% is reached for $\tau \approx 2.8$ and $\tau \approx 2.0$ for the 508 nm beads and Arizona test dust, respectively. The error in the phase function was found to be significantly larger for the 508 nm beads than for the Arizona test dust. A 10% error is found for $\tau \approx 0.48$ for the 508 nm beads, reaching 100% for $\tau \approx 4.1$. The Arizona test dust, however, does not reach a 10% error before $\tau \approx 1.2$ and does not go above 50% for the concentrations investigated. The large difference in error between the two phase functions is attributed to the finer details in the 508 nm beads phase function. Thus, we have shown that errors in both the scattering coefficient and phase function are dependent on the phase function, but to what extent is still not fully explored. Furthermore, both sample sets investigated in this paper are heavily dominated by scattering, increasing the ratio of absorption to scattering is expected to influence the error when plotted against optical depth.

Acknowledgments. We would like to thank one of our anonymous reviewers who brought to our attention the possibility of multiple scattering errors in the Petzold measurements.

Disclosures. The authors declare no conflicts of interest.

References

1. H. Sandven, A. S. Kristoffersen, Y.-C. Chen, and B. Hamre, "In situ measurements of the volume scattering function with LISST-VSF and LISST-200X in extreme environments: evaluation of instrument calibration and validity," *Opt. Express* **28**(25), 37373–37396 (2020).
2. Y. C. Agrawal and H. C. Pottsmith, "Instruments for particle size and settling velocity observations in sediment transport," *Mar. Geol.* **168**(1–4), 89–114 (2000).
3. C. B. Mouw, S. Greb, D. Aurin, P. M. DiGiacomo, Z. Lee, M. Twardowski, C. Binding, C. Hu, R. Ma, T. Moore, W. Moses, and S. E. Craig, "Aquatic color radiometry remote sensing of coastal and inland waters: Challenges and recommendations for future satellite missions," *Remote. Sens. Environ.* **160**, 15–30 (2015).
4. M. Chami, E. B. Shybanov, G. A. Khomenko, M. E.-G. Lee, O. V. Martynov, and G. K. Korotaev, "Spectral variation of the volume scattering function measured over the full range of scattering angles in a coastal environment," *Appl. Opt.* **45**(15), 3605–3619 (2006).
5. M. Soja-Woźniak, M. Baird, T. Schroeder, Y. Qin, L. Clementson, B. Baker, D. Boadle, V. Brando, and A. D. L. Steven, "Particulate backscattering ratio as an indicator of changing particle composition in coastal waters: Observations from Great Barrier Reef waters," *J. Geophys. Res.: Oceans* **124**(8), 5485–5502 (2019).
6. V. G. Harharasudhan and P. Shanmugam, "Modelling the particulate backscattering coefficients of turbid and productive coastal waters," *Ocean Sci. J.* **54**(2), 147–164 (2019).
7. C. Nima, Ø. Frette, B. Hamre, S. R. Erga, Y.-C. Chen, L. Zhao, K. Sørensen, M. Norli, K. Stamnes, and J. J. Stamnes, "Absorption properties of high-latitude Norwegian coastal water: The impact of CDOM and particulate matter," *Estuarine, Coastal Shelf Sci.* **178**, 158–167 (2016).
8. M. Chami, D. McKee, E. Leymarie, and G. Khomenko, "Influence of the angular shape of the volume-scattering function and multiple scattering on remote sensing reflectance," *Appl. Opt.* **45**(36), 9210–9220 (2006).
9. W. H. Slade, Y. C. Agrawal, and O. A. Mikkelsen, "Comparison of measured and theoretical scattering and polarization properties of narrow size range irregular sediment particles," in *2013 OCEANS-San Diego*, (IEEE, 2013), pp. 1–6.
10. L. Hu, X. Zhang, Y. Xiong, and M.-X. He, "Calibration of the LISST-VSF to derive the volume scattering functions in clear waters," *Opt. Express* **27**(16), A1188–A1206 (2019).
11. T. Harmel, M. Hieronymi, W. Slade, R. Röttgers, F. Roullier, and M. Chami, "Laboratory experiments for inter-comparison of three volume scattering meters to measure angular scattering properties of hydrosols," *Opt. Express* **24**(2), A234–A256 (2016).
12. D. Koestner, D. Stramski, and R. A. Reynolds, "Measurements of the volume scattering function and the degree of linear polarization of light scattered by contrasting natural assemblages of marine particles," *Appl. Sci.* **8**(12), 2690 (2018).
13. D. Koestner, D. Stramski, and R. A. Reynolds, "Polarized light scattering measurements as a means to characterize particle size and composition of natural assemblages of marine particles," *Appl. Opt.* **59**(27), 8314–8334 (2020).
14. M. Jonasz and G. Fournier, *Light Scattering by Particles in Water: Theoretical and Experimental Foundations* (Elsevier, 2007).
15. H. C. van de Hulst, *Light Scattering by Small Particles* (Courier Corporation, 1981).
16. B. M. Agrawal and M. P. Mengüç, "Forward and inverse analysis of single and multiple scattering of collimated radiation in an axisymmetric system," *Int. J. Heat Mass Transfer* **34**(3), 633–647 (1991).
17. S.-K. Chae and H. S. Lee, "Determination of radiative transport properties of particle suspensions by a single-scattering experiment," *Aerosol Sci. Technol.* **18**(4), 389–402 (1993).
18. D. McKee, J. Piskozub, and I. Brown, "Scattering error corrections for in situ absorption and attenuation measurements," *Opt. Express* **16**(24), 19480–19492 (2008).
19. D. McKee, J. Piskozub, R. Röttgers, and R. A. Reynolds, "Evaluation and improvement of an iterative scattering correction scheme for in situ absorption and attenuation measurements," *J. Atmospheric Ocean. Technol.* **30**(7), 1527–1541 (2013).
20. D. Doxaran, E. Leymarie, B. Nechad, A. Dogliotti, K. Ruddick, P. Gernez, and E. Knaeps, "Improved correction methods for field measurements of particulate light backscattering in turbid waters," *Opt. Express* **24**(4), 3615–3637 (2016).
21. S. Vadakke-Chanap, P. Shanmugam, and B. Sundarabalan, "Monte Carlo simulations of the backscattering measurements for associated uncertainty," *Opt. Express* **26**(16), 21258–21270 (2018).
22. D. Stramski and J. Piskozub, "Estimation of scattering error in spectrophotometric measurements of light absorption by aquatic particles from three-dimensional radiative transfer simulations," *Appl. Opt.* **42**(18), 3634–3646 (2003).
23. J. Piskozub, D. Stramski, E. Terrill, and W. K. Melville, "Influence of forward and multiple light scatter on the measurement of beam attenuation in highly scattering marine environments," *Appl. Opt.* **43**(24), 4723–4731 (2004).
24. J. T. O. Kirk, "Monte Carlo modeling of the performance of a reflective tube absorption meter," *Appl. Opt.* **31**(30), 6463–6468 (1992).
25. Y. C. Agrawal, "The optical volume scattering function: Temporal and vertical variability in the water column off the New Jersey coast," *Limnol. Oceanogr.* **50**(6), 1787–1794 (2005).
26. W. H. Slade, E. Boss, and C. Russo, "Effects of particle aggregation and disaggregation on their inherent optical properties," *Opt. Express* **19**(9), 7945–7959 (2011).

27. O. A. Mikkelsen, T. G. Milligan, P. S. Hill, R. J. Chant, C. F. Jago, S. E. Jones, V. Krivtsov, and G. Mitchelson-Jacob, "The influence of schlieren on in situ optical measurements used for particle characterization," *Limnol. Oceanogr.: Methods* **6**(3), 133–143 (2008).
28. M. J. Berg, C. M. Sorensen, and A. Chakrabarti, "Explanation of the patterns in Mie theory," *J. Quant. Spectrosc. Radiat. Transfer* **111**(5), 782–794 (2010).
29. T. J. Petzold, "Volume scattering functions for selected ocean waters," Tech. rep., Scripps Institution of Oceanography La Jolla Ca Visibility Lab (1972).



Graphic design: Communication Division, UIB / Print: Skjipes Kommunikasjon AS



uib.no

ISBN: 9788230852804 (print)
9788230844380 (PDF)